

January 2014

MICROMANIPULATOR-RESONATOR SYSTEM FOR SELECTIVE WEIGHING OF INDIVIDUAL MICROPARTICLES

Bin-Da Chan
Purdue University

Follow this and additional works at: https://docs.lib.purdue.edu/open_access_dissertations

Recommended Citation

Chan, Bin-Da, "MICROMANIPULATOR-RESONATOR SYSTEM FOR SELECTIVE WEIGHING OF INDIVIDUAL MICROPARTICLES" (2014). *Open Access Dissertations*. 1069.
https://docs.lib.purdue.edu/open_access_dissertations/1069

This document has been made available through Purdue e-Pubs, a service of the Purdue University Libraries. Please contact epubs@purdue.edu for additional information.

PURDUE UNIVERSITY
GRADUATE SCHOOL
Thesis/Dissertation Acceptance

This is to certify that the thesis/dissertation prepared

By Bin-Da Chan

Entitled

MICROMANIPULATOR-RESONATOR SYSTEM FOR SELECTIVE WEIGHING OF INDIVIDUAL
MICROPARTICLES

For the degree of Doctor of Philosophy

Is approved by the final examining committee:

Cagri A. Savran

Babak Ziaie

Galen B. King

Jeffrey F. Rhoads

To the best of my knowledge and as understood by the student in the Thesis/Dissertation Agreement, Publication Delay, and Certification/Disclaimer (Graduate School Form 32), this thesis/dissertation adheres to the provisions of Purdue University's "Policy on Integrity in Research" and the use of copyrighted material.

Cagri A. Savran

Approved by Major Professor(s): _____

Approved by: Ganesh Subbarayan 12/02/2014

Head of the Department Graduate Program

Date

MICROMANIPULATOR-RESONATOR SYSTEM FOR SELECTIVE WEIGHING OF
INDIVIDUAL MICROPARTICLES

A Dissertation

Submitted to the Faculty

of

Purdue University

by

Bin-Da Chan

In Partial Fulfillment of the

Requirements for the Degree

of

Doctor of Philosophy

December 2014

Purdue University

West Lafayette, Indiana

For my advisor, group members, family, and friends.

ACKNOWLEDGEMENTS

I would like to express my profound gratitude to my advisor Prof. Cagri Savran for his guidance and support throughout my graduate student life at Purdue University. He is knowledgeable in various aspects of scientific research and always encourages me to use critical thinking skills to logically analyze problems. In addition, he always provides me with insightful suggestions about my research as well as reviews and corrects my English writing. To me, he is not only a great academic advisor but also a communication and life coach.

I would like to acknowledge my advisory committee members, Prof. Babak Ziaie, Prof. Galen King, and Prof. Jeffrey Rhoads, for serving on my dissertation committee and for sharing their valuable knowledge and advice. Additionally, I would also like to thank Prof. Nancy Emery from the Purdue University Department of Biological Sciences for her efforts in helping me to collect and to conduct the pollen grain weighing project; Prof. Timothy Ratliff and his student Hsing-Hui Wang from the Purdue University Center for Cancer Research for providing the mouse prostate stem cell spheres and sharing their perspectives about my experimental results; Prof. Vikki Weake and her student Jingqun Ma from the Department of Biochemistry for providing the eye-brain complexes of larval *Drosophila*; Dr. Aamer Mahmood from Birck Nanotechnology Center for his valuable

suggestions about microfabrication; Laurie Mueller from the Purdue University Life Science Microscopy Facility for teaching the cell fixation and HMDS-drying procedures, as well as conducting the cell milling process. With their help and commitments, I was able to accomplish many interesting research topics. Moreover, they also demonstrate the value of being a successful scholar and person by working diligently while staying grounded with the very basic but important factors of our life such as family, passion, and unselfishness.

I would also like to thank my group members, Dr. Chun-Li Chang, Dr. Kutay Icoz, Dr. Khalid Arif, Farrukh Mateen, Wanfeng Huang, Rohil Jain, Onur Gur, and Yiyang Liew for their contributions and assistances to my research. It has been a great pleasure and fun to work with these intelligent and interesting people. Our occasional coffee or bubble tea time is always helpful for both retreating from work and brainstorming about research projects.

Lastly, I would also like to thank my family and friends for their support, inspiration, and tolerance when I am depressed. I enjoy every moment talking to and hanging out with them. I would also like to acknowledge the National Science Foundation Award 1343069 for supporting my research work.

TABLE OF CONTENTS

	Page
LIST OF TABLES	viii
LIST OF FIGURES	ix
ABSTRACT	xiv
CHAPTER 1. INTRODUCTION.....	1
1.1 Micromanipulator	2
1.2 Cantilever-based Mass Sensing System.....	4
1.3 Motion Detection of Cantilever Sensors.....	7
1.4 Diffractometric Cantilever Sensors.....	8
1.5 Weighing of Individual Biological Microparticles Using Resonant Sensors	10
1.6 Organizational Overview	13
CHAPTER 2. DESIGN, FABRICATION AND APPLICATIONS OF THE MICROMANIPULATOR	15
2.1 Introduction.....	15
2.2 Design and Operational Concepts.....	16
2.2.1 Actuation Mechanism	17
2.2.2 Microtweezers.....	18
2.2.3 Clamping Methods and Materials.....	19
2.3 Fabrication Process and Results.....	20
2.3.1 Microfabrication Process	20
2.3.2 Microfabrication Results.....	23
2.3.3 Device Characterization.....	25

	Page
2.3.4 Failure Modes	26
2.4 Applications and Discussion.....	27
2.4.1 Manipulation and Stacking of Microparticles.....	27
2.4.2 Microcontact Printing on Selected Areas	30
2.4.3 Extraction of Stem Cell Spheres from Culture Media	31
2.5 Summary	32
 CHAPTER 3. CANTILEVER-BASED NANOMECHANICAL RESONATOR	 34
3.1 Introduction.....	34
3.2 Fabrication of the Dual Cantilever Sensor.....	36
3.3 Piezoelectronic Actuation	38
3.3.1 Experimental Setup.....	39
3.3.2 Frequency Response due to Added Mass	40
3.3.3 Mass Derivation	43
3.4 Device Characterization.....	45
3.4.1 Determination of the Effective Mass and Effective Stiffness of Cantilevers	46
3.4.2 Effects of Loading Position on Resonance Frequency	48
3.4.3 Uncertainty in Mass Measurement	50
3.4.4 Comparison of Experimental and Ultimate Theoretical Mass Uncertainty	55
3.5 Summary	58
 CHAPTER 4. SELECTIVE WEIGHING OF INDIVIDUAL MICROPARTICLES	 60
4.1 Dry Mass Measurement of Biological Microparticles.....	61
4.2 Preparation of Cancer Cell and Blood Cell Samples	63
4.2.1 Cultivation of Cancer Cell Lines	63
4.2.2 Preparation of Blood Cells.....	63
4.2.3 Fixation, Dehydration and Drying of Cell Samples.....	64
4.3 Weighing of Individual Stem Cell Spheres of Different Inflammation States	65
4.4 Arrangement of Single Particles on Resonator Surface.....	69
4.5 Weighing of Individually Selected Cancer Cells.....	71

	Page
4.6 Weighing in Conjunction with the Focused Ion Beam Cell Milling Process	74
4.7 Characterization of Microparticles over a High Dynamic Range.....	77
4.8 Summary	81
CHAPTER 5. SUMMARY AND FUTURE WORK.....	82
5.1 Summary	82
5.2 Future Work	83
LIST OF REFERENCES.....	87
APPENDICES	
Appendix A Assembly of the Micromanipulator.....	100
Appendix B Focused Ion Beam (FIB) Milling of Cells	102
VITA	104

LIST OF TABLES

Table	Page
Table 3-1: Effective stiffness (k_e), effective mass (M) and resonance frequency (F_r) of different shapes of cantilevers. The cantilever types corresponding to different numbers are shown in Figure 3-3. Scale bars: 50 μm	48
Table 3-2: Experimental and theoretical mass uncertainties at the 99.7% confidence level.....	54
Table 4-1: Mass and dimension of measured biological micro-entities. Dimension indicates the diameter of a spherical particle or the long axis of an oval particle such as a pollen grain. Mass and dimension variation denote the value of 99.7% confidence interval.....	80
Table B-1: FIB cell milling process.....	102

LIST OF FIGURES

Figure	Page
Figure 1-1: The open and close state of the mechanically driven microtweezers [25].....	3
Figure 1-2: Schematic of optical lever detection system utilized to measure the motion of a cantilever beam [56].	8
Figure 1-3: (a) SEM image of an interdigitated cantilever, (b) schematic of the Cross-sectional view of diffraction grating [1].	10
Figure 1-4: The SMR chip (left) and the measurement of single cell using two fluids with different densities [69].	11
Figure 1-5: (a) Measurement of cellular mass using the Pedestal Resonant Sensor [71]. (b) Finite element analysis of cantilever (upper) and pedestal resonator (lower). Color bars indicate the normalized mass sensitivity [59]. (c) Top view of the fully assembled pedestal chip embedded with a PDMS-based perfusion chamber [70].	12
Figure 1-6: Weighing of single particles using cantilever-based sensors: (a) an <i>Escherichia coli</i> cell, scale bar = 5 μm [73], (b) a Vaccinia virus particle, scale bar = 1 μm [74].	13
Figure 2-1: The schematic and components of the micromanipulator. (a) The fully assembled micromanipulator, (b) (c) detailed views of the tip of micromanipulator, (d) exploded view of the micromanipulator.	17
Figure 2-2: Stress distribution in the microtweezers when they are completely closed. ..	19

Figure	Page
Figure 2-3: Major steps of the fabrication process flow. (a) Silicon wafer with 1 μm silicon oxide first cleaned with piranha and acetone. (b) Microtweezer patterns defined by photoresist. (c) Wafer immersed in BOE for SiO_2 removal. (d) Sample wafer attached on a carrier wafer using Crystalbond™ 555 adhesive (PELCO). (e) Exposed silicon removed by Deep RIE. (f) Device released by 90 °C PRS-2000 solution.....	22
Figure 2-4: Mask used for the photolithography process.	23
Figure 2-5: (a) The silicon micromanipulator has a pair of sharp tips to manipulate micro-particles with size as small as 5 μm . (b) A 20 μm bead held by the tweezers	24
Figure 2-6: A view of the operational micromanipulator.	25
Figure 2-7: Variation of tip separation with horizontal displacement of (d) saddle.	26
Figure 2-8: Micrograph of a small clump of plant cells held by the micromanipulator. The inset shows a micrograph of the cell cluster.	29
Figure 2-9: (a) SEM image of the three-layer pyramid constructed with 40- μm -diameter beads. (b) Two-layer pyramid of 40- μm polystyrene beads on a cantilever tip.	29
Figure 2-10: (a) Bright field and fluorescence micrographs of microstamped 40- μm beads. The arrows indicate beads stamped by FITC-BSA. (b) Micro-stamping result shows 'P.'	31
Figure 2-11: Micrographs of (a) a cell sphere being pulled out of viscous Matrigel and (b) cell sphere held by a microtweezer in air.	32
Figure 3-1: Micrograph of a dual-cantilever-based resonator. Scale bar: 50 μm	35

Figure	Page
Figure 3-2: Fabrication process flow. Only major steps are presented. (a) <100> silicon wafer cleaned by piranha and acetone. (b) LPCVD silicon nitride deposition (on both sides). (c) Cantilever patterns defined by photoresist. (d) Silicon nitride removed by Plasma Tech, photoresist removed by piranha and acetone. The processes of photoresist patterning and silicon nitride removal were repeated again on the backside to define die patterns. (e) Device released by KOH solution. (f) Gold deposition.	37
Figure 3-3: SEM image of a dual-beam cantilever.	38
Figure 3-4: Micrograph of different cantilever designs. Scale bar: 50 μm	38
Figure 3-5: (a) Experimental setup of the weight measurement system. (b) First three reflected diffraction modes.	40
Figure 3-6: The frequency response of system with different mass loads. Resonance frequencies of both the sensor and the reference arms are obtained in a single measurement (The 46.5 ng and 9.3 ng beads were placed 12.2 μm and 11.6 μm away from the tip of the cantilever, respectively).	42
Figure 3-7: The resonance frequency of Cantilever #1 (as shown in inset) with location of the load with respect to the cantilever tip.	43
Figure 3-8: (a) SEM image of a pollen grain placed on a cantilever (left arm). The reference cantilever (right arm) was loaded with a polystyrene bead of known mass. Scale bars: 30 μm . (b) Frequency response of the system that shows the resonance frequencies of both cantilevers.	45
Figure 3-9: Dependence of resonance frequency, added mass (m) and loading position (x). Curves represent prediction of Equation (3.1) and circles represent finite element simulations.	50
Figure 3-10: Dependence of the standard deviation in the measured frequency on the excitation voltage and loading.	58

Figure	Page
Figure 3-11: The theoretical uncertainty in mass with respect to the mass and location of the attached matter. 'x' denotes the distance of the load away from the tip of the cantilever.....	53
Figure 3-12: The bar chart illustrates experimental and theoretical uncertainties in mass for single beads (n=10). The average masses and experimental uncertainties in mass of ten different beads are also presented.....	54
Figure 4-1: Schematic of the measurement strategy for selectively weighing individual micro-entities.	61
Figure 4-2: (a) SEM image and (b) corresponding frequency spectrum of weighing a PSC sphere. The system used is referred to as Cantilever #1 in Chapter 3 [143].	67
Figure 4-3: (a) SEM image and (b) the resulting frequency spectrum showing the simultaneously weighing of two different stem cell spheres.	68
Figure 4-4: Measured average (a) volume, (b) mass, and (c) density of naïve and inflamed prostate spheres. Error bar: ± 1 SD.....	68
Figure 4-5: SEM images of microparticles measured by the cantilever-based resonator. (a) KB cell was placed on top of a polystyrene bead for weighing. The inset shows the side view of the cell-bead stack. The green part indicates the KB cell, purple is the adhesive grease layer, and orange is the polystyrene bead. (b) Weighing of a red blood cell. A red blood cell was selectively picked up from a scatter of cells (inset) by the micromanipulator.....	70
Figure 4-6: (a) SEM image of measured A549 cells with their corresponding dry masses. The theoretical uncertainty of the measured mass was around 20 pg. (b) The dry mass of bead-bound KB cells and bare KB cells are compared. The dry mass of A549 and MCF-7 cancer cells were also presented. Error bars represent $\pm 99.7\%$ confidence interval of cell-to-cell variation (not the systematic uncertainty in measurements which is far smaller).....	73

Figure	Page
Figure 4-7: (a) SEM image of an array of KB cells arranged individually after being weighed. Red arrow indicates the specific cell to be milled by FIB. (b) Top view and (c) tilted view of the milled cell. (d) The artificially colored SEM image illustrates the cross-section of the milled KB cell. The green and blue parts represent the surface and interior structure of cell, the yellow part is the thin platinum layer that is deposited to protect and define the milling edge, and the pink part depicts the conductive substrate. Scale bars denote 10 μm	75
Figure 4-8: SEM images of the (a) top view and (b) tilted view of the milled K9-TCC cell. The substrate was glass. (c) Tilted view and (d) top view of a milled K9-TCC located on a cantilever. Scale bars: (a) and (b) are 10 μm , (c) and (d) are 20 μm	76
Figure 4-9: SEM image of the weighing of a diatom (right arm). The inset depicts a magnified view of the diatom on the cantilever tip. The cantilever used is Cantilever #2 shown in Chapter 3.	78
Figure 4-10: Summary chart of all measured biological microparticles. Insets show the SEM images of measured targets including (a) a white blood cell, (b) a bead-bound KB cell, (c) a K9TCC-AN cell, (d) a <i>Lasthenia Glabrata</i> pollen grain, (e) a pancreatic islet spheroid from mouse, and (f) an eye-brain complex collected from <i>drosophila</i> larvae. Error bars represent +/- 99.7% confidence interval. Pancreatic islet spheroid and brain-eye complex have sample size = 1 therefore no error bars are shown.	79
Figure A-1: Schematics of the assembly process. (a) an explosion view of the micromanipulator, (b) assembling micrometer head with the tweezers holder, (c) assembling the cone tip, (d) assembling the microtweezers, (e) assembling the clamping cap, (f) a zoom-out view of the micromanipulator.	101
Figure B-1: SEM images of (a) the selected KB cell, (b) KB cell coated with a thin Pt layer, (c) and (d) milled KB cell. (e-g) Flow chart of the FIB cell milling process. ...	103

ABSTRACT

Chan, Bin-Da. Ph.D., Purdue University, December 2014. Micromanipulator-Resonator System for Selective Weighing of Individual Microparticles. Major Professor: Cagri A. Savran, School of Mechanical Engineering.

Over the past decade, MEMS-based cantilever sensors have been widely used in the detection of biomolecules, environmental pollutants, chemicals and pathogens. Cantilever-based sensors rely on attachment of target entities on their surface. The attachment causes either change in surface stress or resonance frequency of the cantilever, which is detected using various schemes that range from optical to piezoelectric. The majority of these sensors rely on probabilistic attachment of multiple target entities to the sensor surface. This introduces uncertainties since the location of the adsorbed target entity can modify the signal generated by the sensor. In addition, it does not allow the measurement of individually selected target entities. The goal of this dissertation is to exploit the cantilever-based sensors' mass sensing capability to develop a "supermarket weight scale" for the micro world: a scheme that can enable the user to pick an individual target entity and weigh only that particular entity by precisely positioning it on a micro-weight scale.

The system is composed of a manually operated micromanipulator and a cantilever-based micro-resonator. The micromanipulator is able to pick, move and place a

micro-particle of interest, and the micro-resonator can determine the mass of the target particle. During a measurement, an individual target particle selected under a microscope is picked up by the micromanipulator and then placed on the tip of one of the two cantilevers beam for weighing. The differential motion between the two cantilevers is measured by means of a diffraction grating that allows picogram level mass resolutions. Although the main goal of the study is not to develop the world's most sensitive mass detector, we demonstrate that the current resolution of the sensor is sufficient to weigh a wide range of microparticles. We present the capability of the system to select and weigh various individual microparticles from a single red blood cell ($\sim 10^{-11}$ g) to the eye-brain complex of an insect ($\sim 10^{-6}$ g), covering a 5-order-of-magnitude mass range. In addition, we are also able to measure the mass and density responses of stem cells to pathological treatments. We also demonstrate that this weighing scheme can work in conjunction with other experimental practices, such as immunomagnetic separation and focused ion beam milling processes, to provide complementary mass information. We believe this versatile and user-friendly system will be useful to a wide range of users, including biologists and bioengineers.

CHAPTER 1. INTRODUCTION

Microelectromechanical systems (MEMS) sensors have been used for a variety of purposes including detection of motion [1], verification of the existence of biomolecular substances [2, 3] and measuring the magnitude and direction of forces [4, 5]. Among a plethora of different types of sensors, cantilever-based micro/nano resonators have been used excessively as AFM (atomic force microscopy) probes [6], radio frequency filters [7], mass sensors [8], and sensors to detect a wide variety of entities including biomolecules, chemicals, viruses and cells [9]. The benefits of using micro- or nanomechanical resonators are their small size that enables high sensitivity and microfabrication of many of them at the same time. The latter enables large scale integration on a silicon wafer, which significantly reduces costs and increases yield rate by reducing device-to-device variations. The compliant nature of cantilever sensors has been engineered for extremely sensitive detection of external forces and adsorption of small particles including biomolecules and cells [10]. Researchers have shown that cantilever-based resonators are capable of weighing micro-/nano-particles with zeptogram resolution [11, 12]. However, current strategies of weight measurement using cantilevers mostly rely upon random binding of the targets on the cantilever surface. The probabilistic attachment of the targets introduces uncertainties because location of the target particle can substantially influence the dynamic response of the system and hence

the resolution of the measurement [13, 14]. As a consequence, current strategies are most successful when interrogating a large number of target entities that bind randomly onto the sensor surface but are not geared towards analyzing single entities.

The goal of this study is to develop a versatile and practical system that allows users to weigh a single micro-particle of their choice, in a manner as intuitive as how it is done in a supermarket. The system we developed is based on a combination of a micromanipulator and a cantilever-based mass sensor, whereby a designated object can be moved to the tip of a cantilever and weighed. This chapter will first describe the state of the art on various micromanipulators, followed by a review of cantilever-based detection. The chapter ends with an organizational overview of this dissertation.

1.1 Micromanipulator

Microtweezers or microgrippers are developed and used in various fields to manipulate microparticles. They can also be implemented in automatic/robotic devices and be used to study the mechanical properties of objects [15]. Several different actuation schemes have been introduced to operate microtweezers. For example, thermal flexure schemes [16-18] have been widely used as actuation mechanisms to open and close the microgrippers' tips. By using structures or materials with asymmetrical thermal expansion coefficients, the prong section of the microgrippers can be bent, which causes the grippers' tips to open or close according to the applied temperature. Shape memory alloy thin sheets were also used as materials for microgrippers [19]. Other actuation methods, such as scratch drive [20], pneumatic [21], piezoelectric [22, 23] were also

proposed for use in micromanipulators. Other researchers have been able to manipulate submicron substances by optical trapping [24, 25].

The sophisticated methods described above require extensive fabrication steps, electrical connections, power sources, and/or other additional components (e.g., heating and magnifying elements) for actuation, which directly affect their versatility, compactness, and overall utility. In order to address several complexities in the aforementioned methods, researchers have proposed mechanical actuation as an alternative [26, 27]. In the system depicted in Figure 1-1, a specially designed micro-box is used to mechanically bend the tweezers arms and therefore actuate the microtweezers' tips.

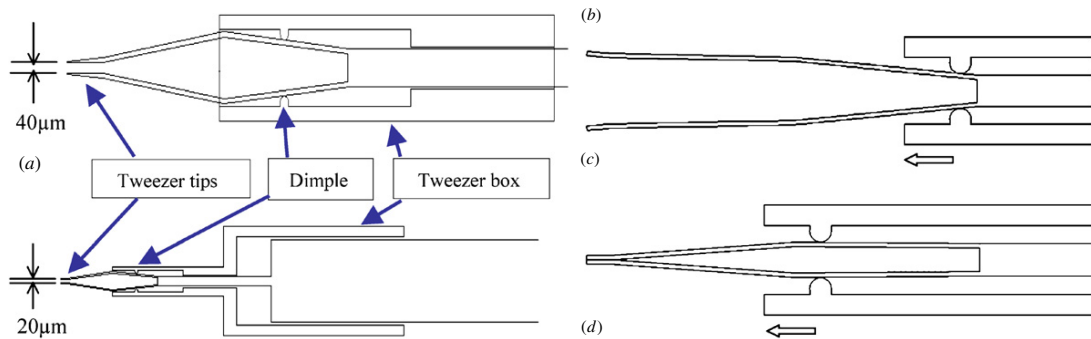


Figure 1-1: The open and close state of the mechanically driven microtweezers [26].

The system shown in Figure 1-1 is based on sliding a plastically deformed metallic pair of tweezers inside a box that forces them to further deform elastically to close the tips. The design is simple, elegant and devoid of electrical actuation but relies on friction and plastic deformation which may be difficult to control and could result in large device-

to-device variations as well as variations in controlling the tip distance and hysteresis. In this dissertation, our goal is a system that is also mechanically actuated but one with controllable fabrication and operation parameters with minimum hysteresis or device-to-device variations.

1.2 Cantilever-based Mass Sensing System

Micro-/ nanocantilevers are widely applied in mass measurement because of their virtues in simple design and low spring constant that render them extremely sensitive to external forces as well as adsorption of additional load [2, 28]. Due to its high sensitivity (as small as zeptogram-scale resolution [12]), in addition to direct mass measurements [29-32], cantilever-based resonant sensors have also been used for measuring humidity [33-35], pH values [36, 37], viscoelasticity [38], carbon deposition on nanowires [39], and temperature [40, 41].

Cantilever-based sensors can be operated both in static, i.e. stress sensing, or dynamic, i.e. resonator modes [2]. In the static mode, a surface stress deflects the cantilever according to

$$\Delta z = \frac{3l^2(1-\nu)}{Et^2} \Delta\delta, \quad (1.1)$$

where l , t , ν , E , $\Delta\delta$ represent the length, thickness, Poisson's ratio, Young's modulus and differential surface stress between the top and the bottom surfaces of the cantilever, respectively. The surface stress accumulation is a slow process, and hence moves the cantilever slowly. This means that the system is prone to low frequency noise and disturbances that exhibit a flicker or $1/f$ -type behavior [42]. Also, as implied by Equation

(1.1), the input that is inferred by the deflection of the cantilever is surface stress and not exactly the added mass (even though there is some correlation between the two).

In the dynamic mode on the other hand, the cantilever is oscillated over a range of frequencies including the resonance frequency that changes with added mass. The angular resonance frequency of the first oscillation mode of an ideal rectangular cantilever in the absence of damping can be expressed as [43, 44]

$$\omega_0 = \sqrt{\frac{k_e}{M}}, \quad (1.2)$$

where k_e is the effective spring constant and M is the effective mass of the cantilever. The spring constant of a rectangular cantilever is

$$k_e = \frac{Ewt^3}{4l^3}. \quad (1.3)$$

Here, E is the Young's modulus of the cantilever, and w , t , l represent the width, thickness and length of the cantilever, respectively. With a mass m loaded on the tip of a cantilever, the resonance frequency of the cantilever is modified as [45]

$$\omega_1 = \sqrt{\frac{k_e}{M+m}}, \quad (1.4)$$

For masses located not far away from the tip of the cantilever, Equation (1.4) is a good approximation.

For cantilevers operated in the dynamic mode, the mass of entities loaded on a cantilever can be derived from the changes in resonance frequency [46]:

$$m = k_e \left(\frac{1}{\omega_1^2} - \frac{1}{\omega_0^2} \right), \quad (1.5)$$

where k_e denotes the spring constant of the cantilever, ω_1 is the resonance frequency after the mass is loaded, ω_0 is the resonance frequency of the empty cantilever.

The smallest detectable mass (δM) of a cantilever with a constant stiffness is ultimately determined by the minimum measurable frequency ($\delta\omega_0$), which can be expressed as [47]:

$$\delta M \approx -2 \frac{M}{\omega_0} \delta\omega_0, \quad (1.6)$$

where M and ω_0 denote the modal mass and angular resonance frequency of the cantilever, respectively. For an externally driven cantilever which is only limited by thermomechanical noise [48], the ultimate minimum measurable frequency is:

$$\delta\omega_0 \approx \left[\frac{K_B T}{E_c} \frac{\omega_0 BW}{Q} \right]^{1/2}. \quad (1.7)$$

Here, K_B is Boltzmann's constant, T is ambient temperature. BW and Q depict the bandwidth and quality factor of the measurement. E_c is the maximum drive energy provided by the external excitation, which can be expressed as $E_c = M\omega_0^2 \langle x_c \rangle^2$. $\langle x_c \rangle$ represents the root mean square (RMS) amplitude of the resonator driven by the external excitation. With Equation (1.7) and Equation (1.8), we can rewrite the minimum detectable mass (δM) of a cantilever as:

$$\delta M \approx 2M \left(\frac{E_{th}}{E_c} \right)^{1/2} \left(\frac{BW}{Q\omega_0} \right)^{1/2}. \quad (1.8)$$

It is important to note that Equation (1.7) and Equation (1.8) assume that thermal noise, i.e. the “ kT ” noise, is the only noise source affecting the system. In practice however, there will be many other factors such as noise in the external actuator, in the illumination source and the electronic components used in the experimental setup, which will contribute to detection uncertainty. Hence the actual mass resolution is likely to be worse than what Equation (1.8) predicts. Therefore it is important to experimentally verify the minimum mass that can be detected using the system in question. The

numerical figures provided by Equation (1.8) should only be used as frame of reference with which the experimentally determined uncertainty can be compared. Equation (1.8) can however be used for general design guidelines. For example, as we will show later, it is generally true that detecting small masses requires large external excitation (E_c), a high quality factor (Q) and a small modal mass.

The goal of this thesis study is not to maximize mass sensitivity but rather to design a simple and intuitive system that has sufficient sensitivity to allow detecting a wide variety of particles that are of relevance. As we discuss later in this thesis, we did employ external excitation to enhance our resolution but refrained from specialized experimental conditions (such as vacuum packaging to enhance Q) that could result in excessively large and or complicated systems that are difficult to build and operate.

1.3 Motion Detection of Cantilever Sensors

The motion of a cantilever-based sensor can be detected using a variety of schemes. Some of these techniques require integration of a motion-detecting interface into the cantilever during its microfabrication such as piezoelectric and piezoresistive schemes [49-51]. These schemes allow operation of the cantilever in a stand-alone fashion, without the need of an external detection scheme. They however require some external circuitry to process the signals produced by the motion-sensing interface. They also significantly increase the complication and hence the cost of device fabrication. Researchers have used optical detecting schemes to avoid such complications. These schemes are external, but are much easier to implement: they require very small or no modification of the cantilever fabrication process. The most common optical motion

interrogation scheme is the optical lever method [52, 53], which is commonly used in the atomic force microscopy. In this scheme, a laser beam is directed to the tip of the cantilever and its reflection, which is altered by the cantilever's motion, is measured using a split photodiode (Figure 1-2). This scheme requires precise alignment and also suffers from the jittering noise of the laser source. In order to mitigate these effects, researchers have integrated diffraction gratings into cantilevers [1, 54, 55]. Integrating a diffraction grating into a cantilever is relatively simple and requires only a simple modification of the cantilever structure that can easily be incorporated during the design of the mask for photolithography.

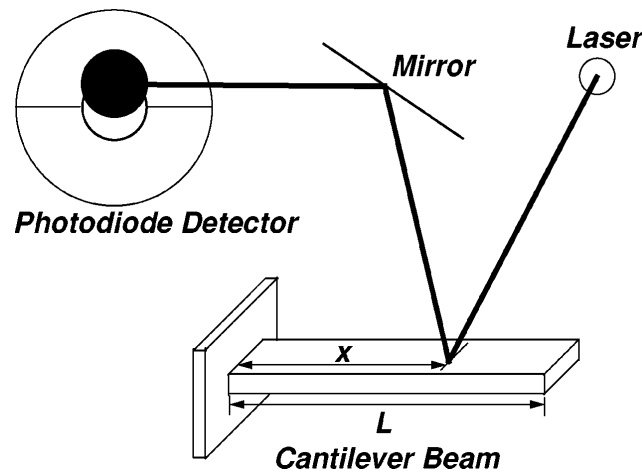


Figure 1-2: Schematic of optical lever detection system utilized to measure the motion of a cantilever beam [56].

1.4 Diffractionmetric Cantilever Sensors

Diffractionmetry has been shown to be effective in improving the resolution of cantilever motion measurements. This method works by integrating a diffraction grating

into the cantilever structure [57]. The diffraction grating appears as a set of interdigitated fingers half of which move in tandem with the cantilever while the other half remain stationary. As shown in Figure 1-3 the interdigitated fingers diffract the incident light into several beams called “diffraction modes”.

The intensity of diffraction modes alternates in accordance with the deflection between two adjacent cantilevers. The intensities of even diffraction modes (0^{th} , 2^{nd} , ...) can be expressed as:

$$I_{\text{even}} \propto \cos^2 \theta, \quad (1.9)$$

and the intensities of the odd modes (1^{st} , 3^{rd} , ...) are:

$$I_{\text{odd}} \propto \sin^2 \theta, \quad (1.10)$$

where θ represents the phase difference between two cantilever beams. As the incident light is perpendicularly illuminating the cantilever plane, θ is expressed as:

$$\theta = \frac{2\pi}{\lambda} \delta. \quad (1.11)$$

The phase θ varies with the wavelength (λ) of the incident optical beam and the spatial displacement (δ) between two adjacent cantilevers. For a fixed wavelength, the intensities of diffraction modes are only sensitive to the displacement between the two cantilevers. Therefore, one can obtain the deflection distance between neighboring cantilevers by observing the intensity of the reflected diffraction modes. The operation of the diffractometry-based cantilever would be the same whether the cantilever is used in the static stress-sensing mode or the dynamic mass-sensing mode.

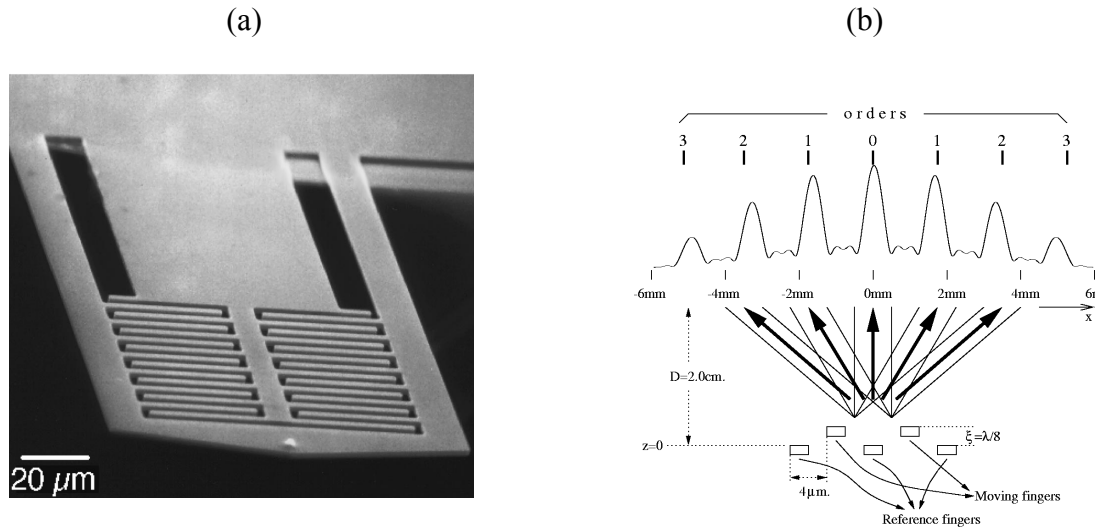


Figure 1-3: (a) SEM image of an interdigitated cantilever, (b) schematic of the Cross-sectional view of diffraction grating [1].

1.5 Weighing of Individual Biological Microparticles Using Resonant Sensors

Mass measurement using resonant sensors is attractive not only due to superior resolution but also due to the ability of detecting mass directly as opposed to inferring it from measurements performed in other domains (e.g. in optical). Therefore applying this scheme to weigh biological entities has also become popular quickly. The mass of biological micro-entities such as cells has been associated with the growth of cells [58, 59] or the effects of pathological and chemical treatments on cells [60, 61]. Researchers have tailored resonant sensors into various forms and architectures to detect cells and other biological entities.

The SMR (suspended microchannel resonator) was developed by the Manalis Lab at MIT to detect biological samples in liquid that flows through the internal channels of

the device that oscillates in vacuum [62-64]. This addresses the problem of low quality factor and large modal mass caused by oscillating a cantilever in liquid. As shown in Figure 1-4, the device is composed of a silicon cantilever with a microfluidic channel embedded in it. As an entity passes through the microfluidic channel, the mass of the particle leads to a change in the resonance frequency of the cantilever [65]. Recently, the SMR method has been used for a variety of applications including monitoring the growth of individual cells [66, 67], estimating water content in single cells [68], and investigating the cellular response to chemicals [69].

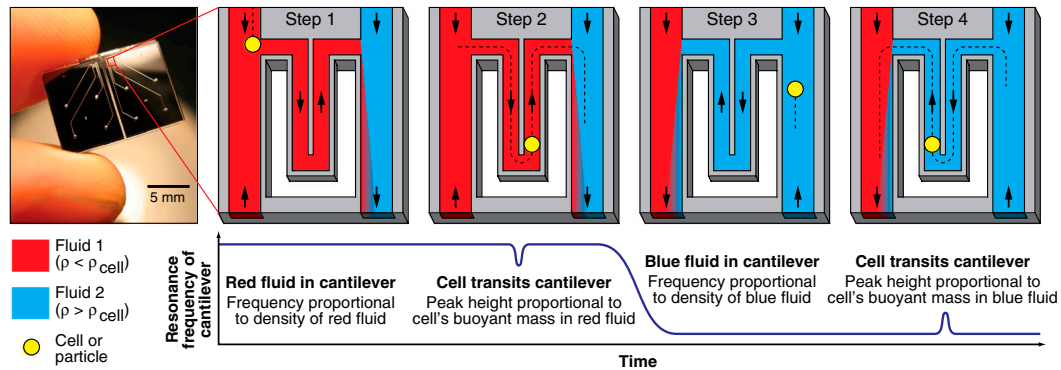


Figure 1-4: The SMR chip (left) and the measurement of single cell using two fluids with different densities [69].

The pedestal resonant sensor is another recently developed technique that can be used to measure the “apparent mass” of single biological microparticles. The sensor has a unique structure of a $60 \times 60 \mu\text{m}^2$ platform supported by four beam-springs to provide uniform mass sensitivity across the device (Figure 1-5a). This design is used to alleviate the problem of uneven mass sensitivity that results when particles land on random

locations on the surfaces of conventional cantilever-based sensors (Figure 1-5b). To deposit target cells on sensor surfaces, a polydimethylsiloxane (PDMS) perfusion chamber was attached on the pedestal sensor array (Figure 1-5c) for cell incubation. This PDMS well, in combination with an on-chip microfluidic system, was used for depositing cells and providing essential nutrients for cell culturing [70]. The device has been successfully applied to monitor the growth of mammalian cells in terms of changes in their stiffness and mass [59, 70].

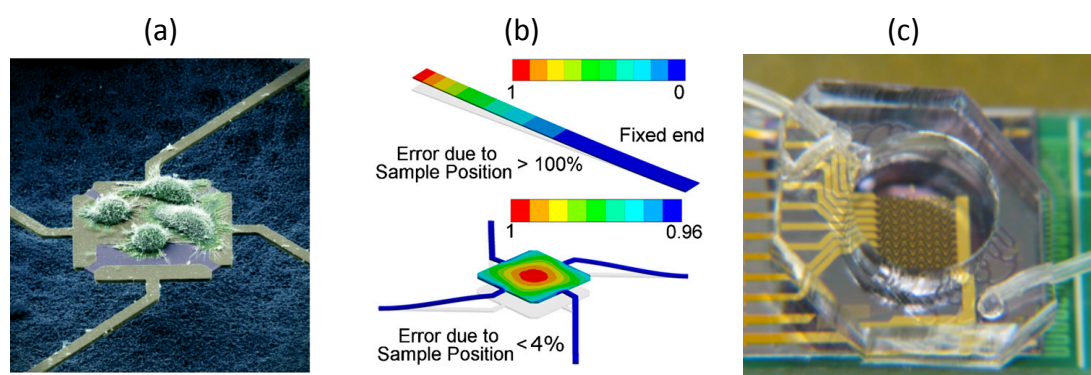


Figure 1-5: (a) Measurement of cellular mass using the Pedestal Resonant Sensor [71]. (b) Finite element analysis of cantilever (upper) and pedestal resonator (lower). Color bars indicate the normalized mass sensitivity [59]. (c) Top view of the fully assembled pedestal chip embedded with a PDMS-based perfusion chamber [70].

Finally, cantilever-based sensors have also been used to measure the mass of individual biological microparticles. Even though the sensors have the capability to resolve the mass of single biological entities, this is often achieved by relying on random binding of single entities on the sensor surface and not by positioning an individual particle selected by the user. Figure 1-6a and Figure 1-6b [2, 72-74].

Here we combine a micromanipulator and a cantilever-based resonator to perform the *on-demand* and selective weighing of single biological microparticles including red blood cells, cancer cells, pollen grains, and pancreatic islet spheroids.

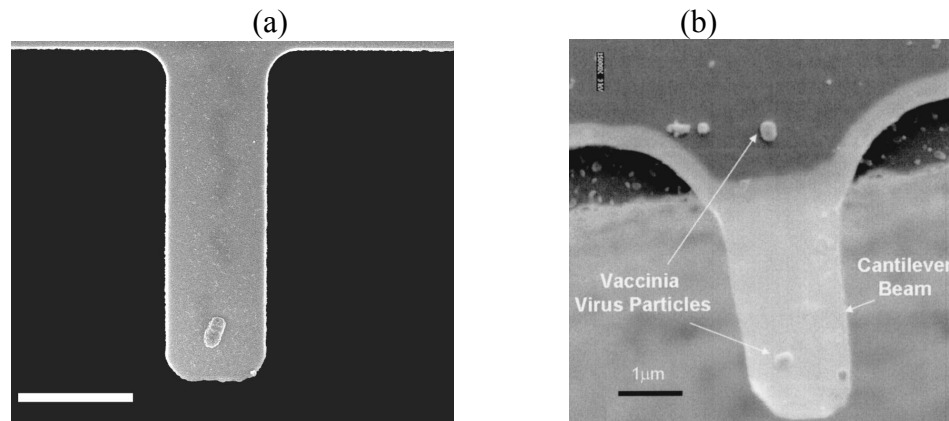


Figure 1-6: Weighing of single particles using cantilever-based sensors: (a) an *Escherichia coli* cell, scale bar = 5 μm [73], (b) a Vaccinia virus particle, scale bar = 1 μm [74].

1.6 Organizational Overview

Chapter 2 focuses on the design, fabrication, and applications of a mechanical driven micromanipulator. The compact, user-friendly and manually actuated micromanipulator is demonstrated as well as its applicability to various fields including construction of 3-D microstructures, placement and arrangement of individual microparticles on specific locations, microcontact printing, and manipulation of live cells.

In Chapter 3, the design and fabrication of the cantilever-based resonator is discussed and an introduction is made to the applications of the system. Uncertainty analyses are also performed to characterize the errors in the measurement.

Chapter 4 presents the combination of the micromanipulator and the cantilever-based resonator to selectively measure the mass of a variety of microparticles. The use of system to determine the dry mass of tumor cells and prostate stem cell spheres is demonstrated. Afterward, the system's utility in interrogating cancer cells in conjunction with other experimental techniques including immunomagnetic separation and focused ion beam milling is presented. Finally, the chapter ends by presenting the weighing of various microparticles covering a 5-order-of-magnitude dynamic range from tens of a picogram (10^{-11} g) to several microgram (10^{-6} g).

In Chapter 5, we summarize the dissertation and present a plan for future work.

CHAPTER 2. DESIGN, FABRICATION AND APPLICATIONS OF THE MICROMANIPULATOR

This chapter presents the design, fabrication and some applications of the micromanipulator (microtweezers) that is able to operate in both liquid and air, and transport micro-objects between the two media. The design and actuation mechanism are first introduced in Section 2.2. In Section 2.3, the fabrication approaches and results are presented. Additionally, the actuation setup and characterization of the device are also shown in this section. Finally, in Section 2.4, several applications of the micromanipulator, such as particle-by-particle microfabrication in 3D, micro-functionalization of individual particles and manipulation of live cells are demonstrated.

2.1 Introduction

Micromanipulators or microgrippers are developed and used in various fields to manipulate or characterize microparticles. As discussed in Chapter 1, many current products have some drawbacks that limit their applicability including high fabrication cost and complex structures and actuation mechanisms. In this chapter, we introduce a versatile, user-friendly and easy-to-fabricate micromanipulator. By combining the elastically deformable and replaceable micromachined tweezers with manual mechanical actuation, the device can readily grab, move, and place microparticles in various media.

2.2 Design and Operational Concepts

The device is composed of a micromachined silicon pair of micro-tweezers, a micrometer head, and an interface connecting the two. The microfabricated pair of tweezers is secured on a cured-polymeric interface (tweezers holder), which allows connection to the spindle of a micrometer head for manual actuation by rotating the thimble (schematically shown in Figure 2-1). The “cone tip” in Figure 2-1, which is connected to the micrometer’s spindle, can move back and forth by rotating the micrometer’s thimble manually. The movement of the cone tip induces the opening/closing of the prong tips of the microtweezers. Details of the actuation mechanism, tweezers design, and clamping methods are introduced below.

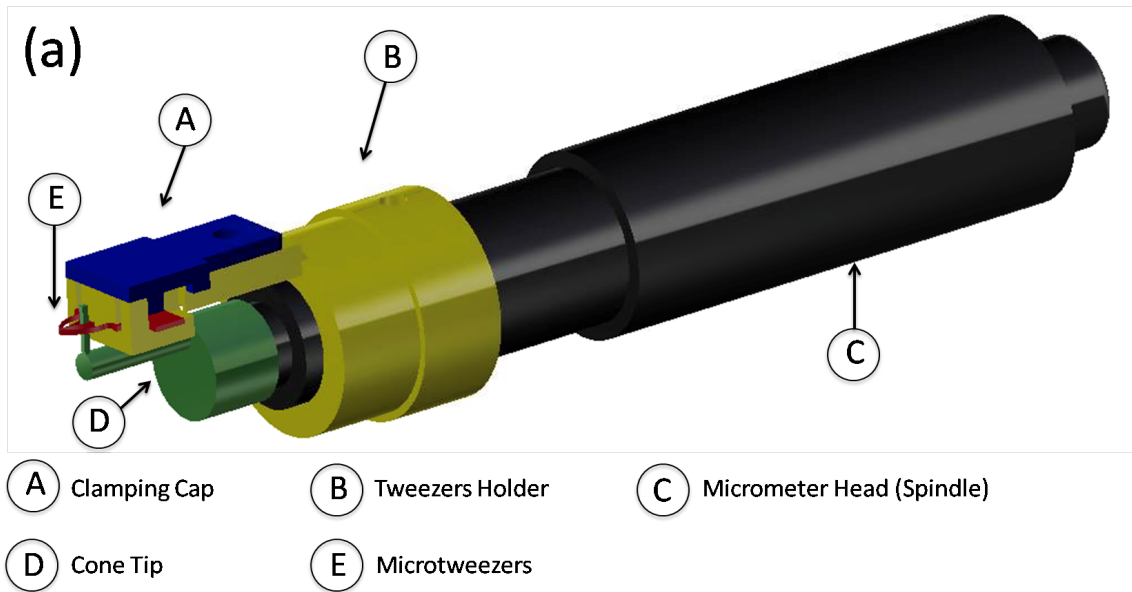


Figure 2-1: The schematic and components of the micromanipulator. (a) The fully assembled micromanipulator, (b) (c) detailed views of the tip of micromanipulator, (d) exploded view of the micromanipulator.

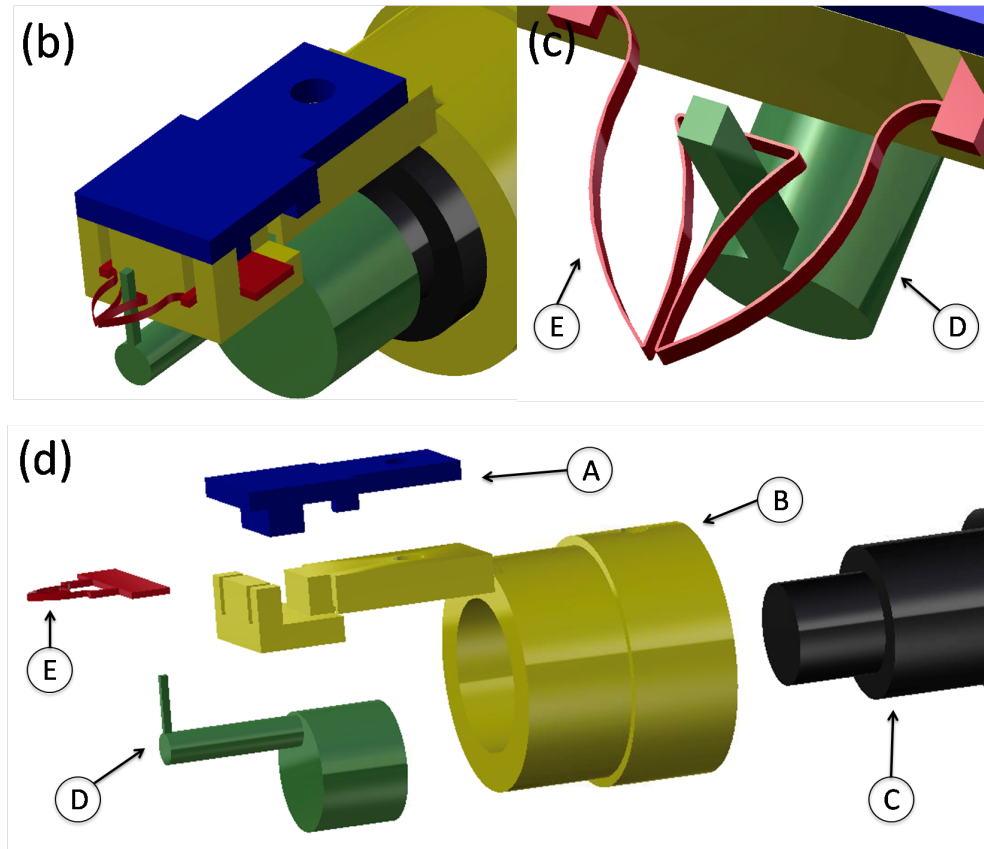


Figure 2-1: Continued.

2.2.1 Actuation Mechanism

The microtweezers are mechanically actuated by manually rotating the spindle to move the cone tip back and forth. The micrometer head that we used has a nonrotating spindle with a resolution of 1 μm and a dynamic range of 25 mm (Global Towns NRM-100). As seen in Figure 2-1c, the cone tip rests against the bridge (or “saddle”) that connects the prongs of the microtweezers. Moving the cone backward exerts a force on the saddle, which deforms the tweezers elastically and closes the tips. Similarly, moving

the cone tip forward opens the tweezers. The entire silicon structure is operated elastically, hence no noticeable hysteresis or permanent deformation occurs.

2.2.2 Microtweezers

The microtweezers are made by micromachining a silicon wafer into a compliant structure. The structure was first designed using the ABAQUS finite-element software package to achieve closure of the tips by a manual input transferred to the structure by means of a micrometer head, without exceeding critical stress values that could cause fracture.

Several parameters were used in the simulation. The Young's modulus and Poisson's ratio were taken as 190 GPa and 0.17 respectively [75]. In the simulation, only two constraints were employed: the two square bases in Figure 2-2 are fixed in all directions (3 translational and 3 rotational), and the cone tip moves only in one direction which is against the surface of the saddle section. 3D stress hexagon elements (C3D8R in ABAQUS) were used to construct the mesh for the finite element analysis.

Figure 2-2 shows the resulting stress distribution of the microtweezers whereby the cone tip moves backward by 110 μm , bringing the prong tips to contact and closing the tweezers completely. The maximum von Mises stress (red color) is about 103 MPa, which occurs at the part where the saddle contacts the cone tip. The maximum stress is well below the tensile strength of silicon (~ 7 GPa), hence the structure is safe during normal operation.

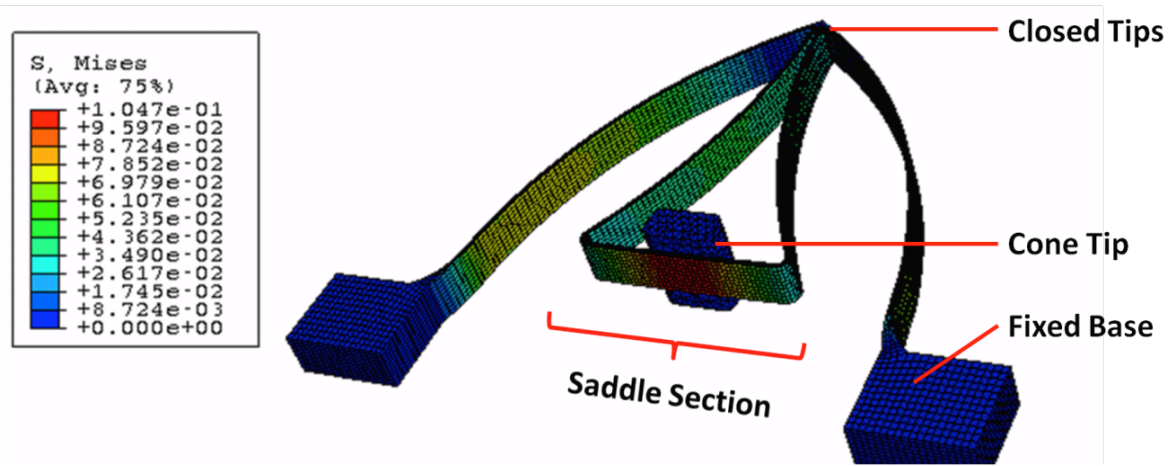


Figure 2-2: Stress distribution in the microtweezers when they are completely closed.

2.2.3 Clamping Methods and Materials

The holding elements (including the clamping cap, tweezers holder and cone tip) are made by the 3D prototyping (FastProtos.com) technique using the material FullCure® 830 curable polymer [76]. In comparison with a previous design in which the tweezers holder was made by graphite [77], the polymeric parts have advantages of simpler fabrication, lower cost, lighter weight, ease of installation, stainless parts, and lack of need for screws for fastening.

To install the microtweezers in the holder, the silicon microtweezers is first slid into the two grooves of the tweezers holder by using another translation stage. Afterward, the apex column of the cone tip is manually adjusted to rest exactly next to the middle point of the saddle section. This alignment step is essential to avoid the cone tip from pressing on an off-centered portion of the saddle section, which can results in an imbalanced closure of prong tips. Finally, the clamping tip is secured to prevent the

microtweezers from moving within the tweezers holder. After the microtweezers are clamped at the holder, and connected to the micrometer, the assembly can be attached to a variety of translation stages to allow translational and rotational movements in every direction. The assembly process is schematically presented in Appendix A.

2.3 Fabrication Process and Results

In order to fabricate the silicon microtweezers, a 4-inch, 500 μm -thick, single-side polished, silicon $\langle 1\ 0\ 0 \rangle$ wafer with a 1 μm -thick silicon oxide (SiO_2) layer was used as the bulk material.

2.3.1 Microfabrication Process

The fabrication process involved two major steps, namely photolithography and deep reactive ion etching (RIE). After the piranha and acetone cleaning steps, the AZ-9260 photoresist was spun on the silicon wafer twice to provide protection during the dry etching procedure. The thickness of photoresist layer was between 12 to 15 μm (verified by an Alpha-Step Profilometer).

After a sequence of photolithography procedures including soft bake (at 110 $^{\circ}\text{C}$), UV-exposure (8 mW/cm^2 power for 31 seconds), development (using AZ-400K developer) and hard bake (120 $^{\circ}\text{C}$), the wafer was immersed in a buffered oxide etchant (BOE) to remove the exposed SiO_2 layer. The patterned photoresist/ SiO_2 layer defined the feature of the microtweezers and also formed a protection layer for the dry etching procedure.

To carry out the deep-RIE process, an STS Advanced Silicon Etch DRIE System (STS-ASE) was used to perform the anisotropic Bosch Process that enables fairly vertical walls. The STS-ASE system alternated between the SF_6 gas to remove the silicon, and the C_4F_8 gas to deposit a protection layer on the sidewalls. After dry etching, the 4-inch wafer was immersed in a 90 °C solvent solution (PRS-2000) to remove the passivation residue (C_4F_8). The process is schematically presented in Figure 2-3.

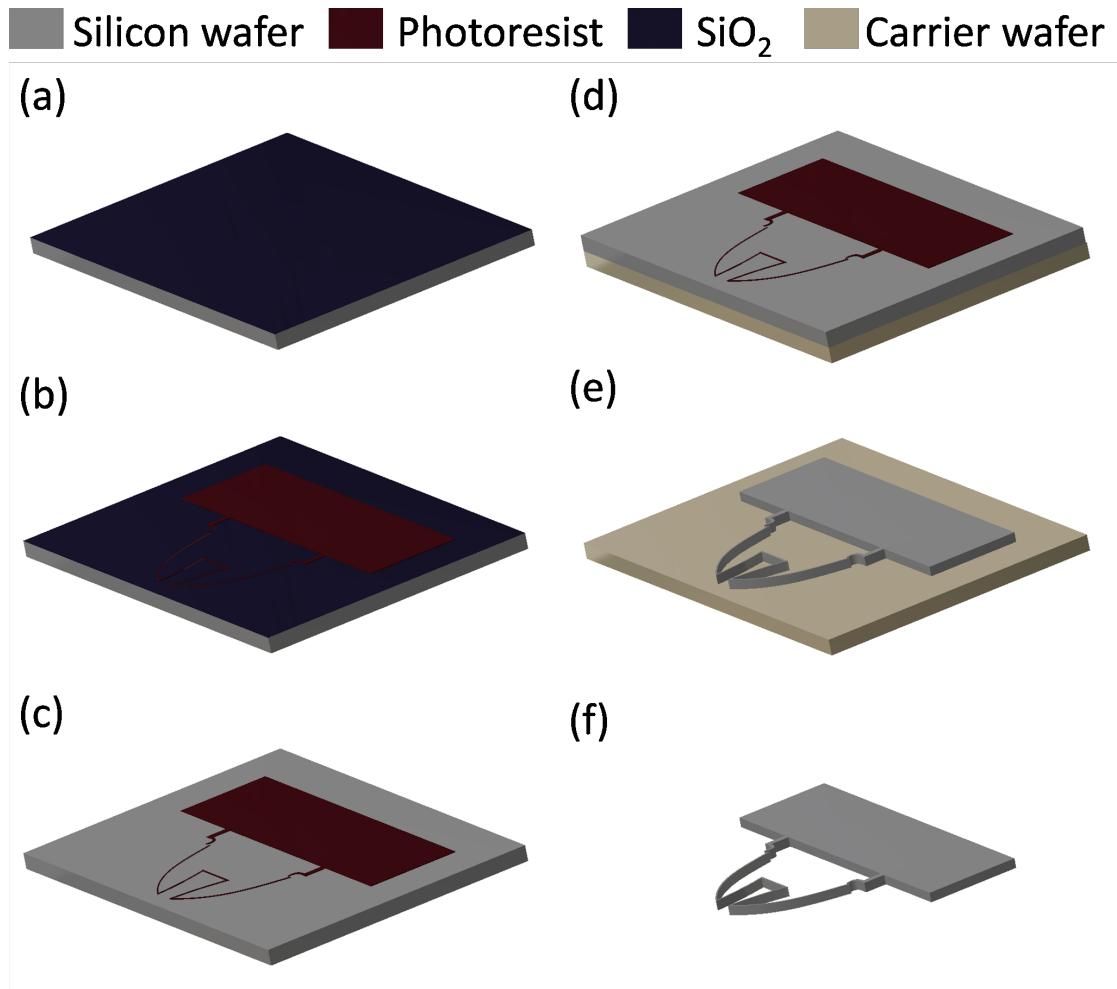


Figure 2-3: Major steps of the fabrication process flow. (a) Silicon wafer with 1 μm silicon oxide was first cleaned with piranha and acetone. (b) Microtweezer patterns defined by photoresist. (c) Wafer immersed in BOE for SiO₂ removal. (d) Sample wafer attached on a carrier wafer using Crystalbond™ 555 adhesive (PELCO). (e) Exposed silicon removed by Deep RIE. (f) Device released by 90 °C PRS-2000 solution.

2.3.2 Microfabrication Results

Figure 2-4 shows the dark-field mask pattern that was used in the fabrication. As seen in this figure, up to ten tweezers can be obtained after processing each wafer (depending on the yield rate which usually is between 50% and 80%). After removing individual tweezers from the wafer by cutting the breakout tabs, a microtweezers is installed on the holding interface. Figure 2-5a illustrates the micrograph of a pair of microtweezers. As seen in this figure, the sharp tips of microtweezers allow manipulation of relatively small particles (down to 5 μm), while their parallel orientation facilitates grabbing larger particles. Figure 2-5b illustrates both 20- μm and 42- μm polystyrene microspheres (Spherotech) held by the microtweezers.

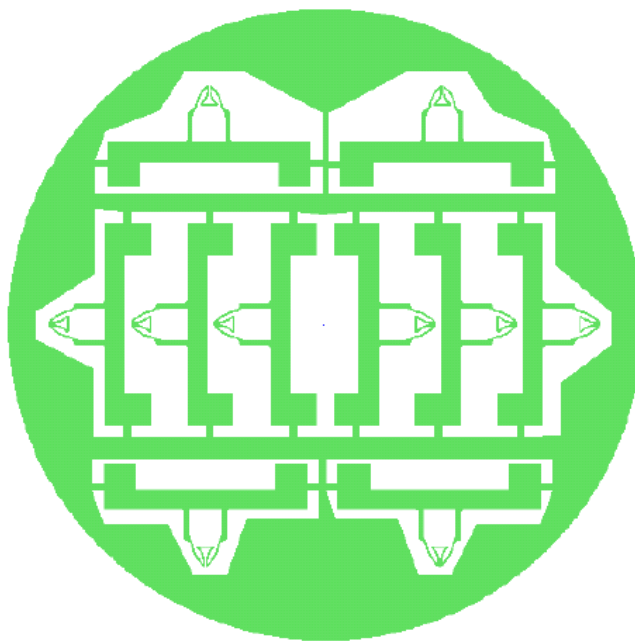


Figure 2-4: Mask used for the photolithography process.

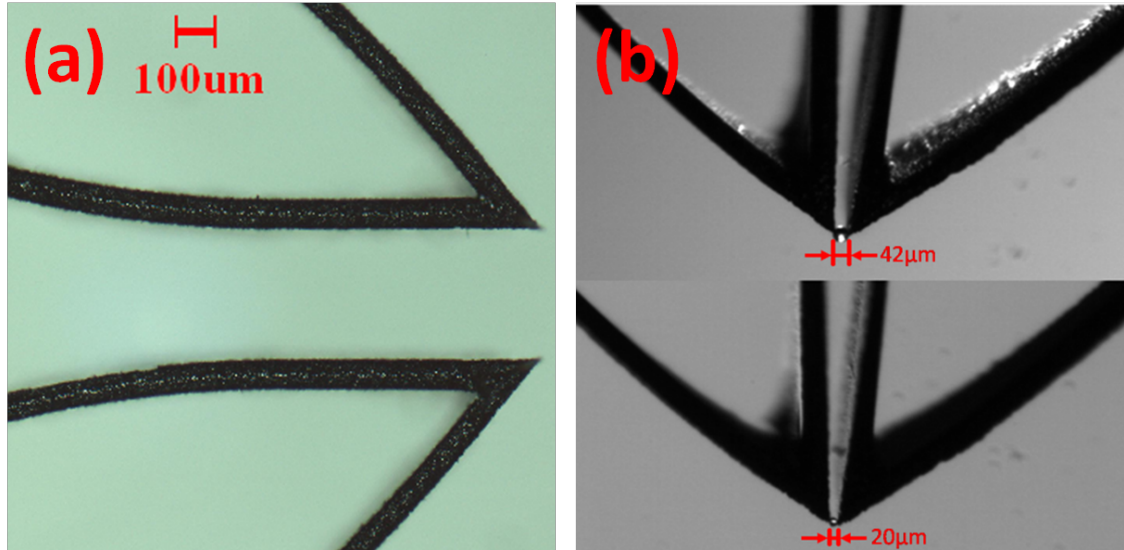


Figure 2-5: (a) The silicon micromanipulator has a pair of sharp tips to manipulate micro-particles with size as small as 5 μm . (b) A 20 μm bead held by the tweezers.

Figure 2-6 shows the fully-assembled micromanipulator that is ready to operate in an inverted position (the orientation can be modified depending on the application). The microtweezers are able to grab a target particle, and move and place it as desired. The elastic deformation of the silicon microtweezers' structure constitutes a restoring force that tends to open the tweezers. However, since the effective stiffness of the manually actuated micrometer head is far greater than that of the silicon structure, a given amount of manual actuation effectively “locks” the distance between the two tips. Therefore, a given distance between the tweezers tips can be maintained virtually indefinitely without providing continuous user input or any other kind of electrical or magnetic actuation. This provides a significant advantage in holding particles in place (or under a given amount of compression) for long amounts of time.

Additionally, since the device can readily be attached to or disconnected from most translation stages, it is possible to grab a particle and move it to a far location (e.g. to another laboratory) while the target entity is held by the tweezers.

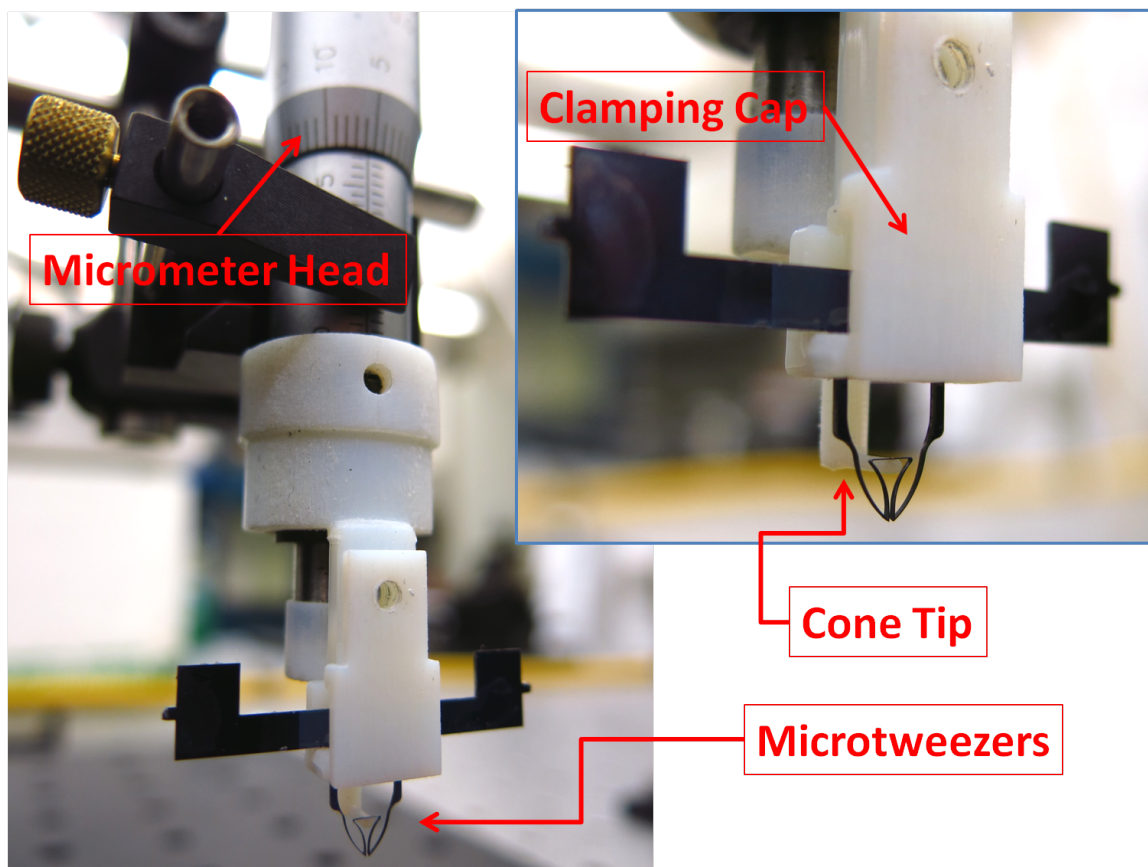


Figure 2-6: A view of the operational micromanipulator.

2.3.3 Device Characterization

We characterized the mechanical behavior of the device by observing the distance between the tips versus the horizontal displacement of the saddle/cone tip. Figure 2-7 shows both the experimental observations and the results of a finite-element simulation.

Displacements were measured by means of calibrated bright field microscopy. Figure 2-7 shows a linear input–output relationship and a good agreement with simulation results. Measurements were made during both closing and opening of the tips with no noticeable difference between the tip separations, indicating that the device exhibits no significant hysteresis. According to the slope of the line in Figure 2-7, and the micrometer’s output (spindle) resolution, the resolution of the prong tip motion is approximately $3\text{ }\mu\text{m}$.

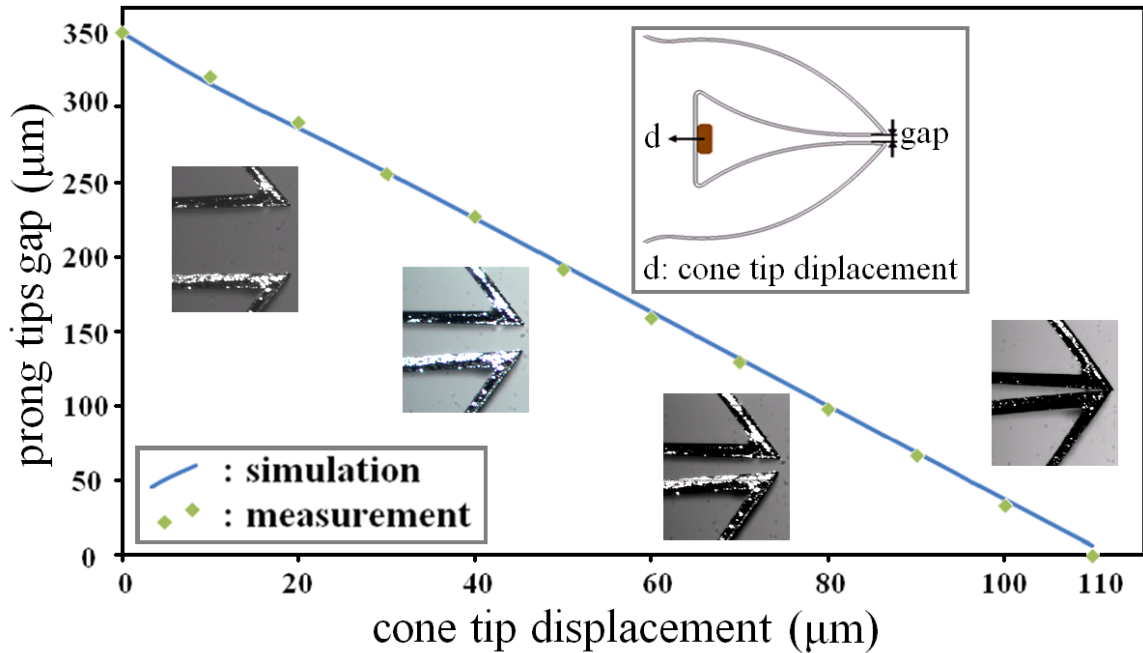


Figure 2-7: Variation of tip separation with horizontal displacement of (d) saddle.

2.3.4 Failure Modes

The primary failure mode of the device is the fracture of the silicon microtweezers upon crashing into a much less compliant surface. We were able to use a pair of tweezers for up to 12 months (more than 1,000 uses) before it was accidentally crashed into a hard

surface. Another possible mode of tweezers failure is the over-tightening of the thimble. However, since the tweezers motion is observed at all times during operation, the occurrence of this is unlikely. Since multiple tweezers are fabricated on a silicon wafer, a broken pair of tweezers can be replaced without difficulty.

2.4 Applications and Discussion

As discussed before, the micromanipulator can operate in both air and liquid and move particles between these two media. The dynamic range and resolution of motion depend on those of the motion stage where the device is attached. We use three Thorlabs PT1 translation stages to move the micromanipulator in 3 translational directions. The translation stages have 25-mm dynamic range and a resolution of 20 μm / thimble graduation, although much smaller movement ($\sim 2 \mu\text{m}$) can be achieved by monitoring the movement continuously under a microscope. We describe below various applications of this versatile and easy-to-use system.

2.4.1 Manipulation and Stacking of Microparticles

As an example, Figure 2-8 illustrates the manipulation of the *Arabidopsis Thaliana* plant cells (provided by Department of Botany and Plant Pathology, Purdue University). Initially the plant cells were randomly distributed in the culture media. In the experiment, a cluster of plant cells (containing 4 to 5 cells) was chosen under the microscope. By using the microtweezers, this cluster of cells was isolated and removed from the natural media without being damaged. To avoid adhesion of cells to the surface of the microtweezers, the cells were released from the device before they were completely dried.

In addition to manipulating living cells, the use of translation stages also enables multiple features such as stacking particles to form 3-D geometries or placing them at distinct positions on other devices or sensors. Figure 2-9a shows a three-layer pyramid structure constructed using fourteen polystyrene beads with diameters around 40 μm . A conductive tape was used to provide adhesion for the first layer of beads as well as to assist in scanning electron microscopy (SEM). The 3×3 bottom layer was constructed by placing beads directly on the conductive tape. To improve the structural integrity of the pyramid and to secure the beads during the SEM imaging, the bottoms of the beads of the second and third layers were dipped partially into grease before placement on the bottom layer of beads.

The micromanipulator was also used to place particles gently on an extremely fragile structure. Figure 2-9b shows a two-layer pyramid built by placing individual beads on the tip of a 500 nm-thick micromachined cantilever while avoiding contacting adjacent structures. Such a capability enables “on-demand” weighing of micro particles or organisms individually isolated from a large group of samples.

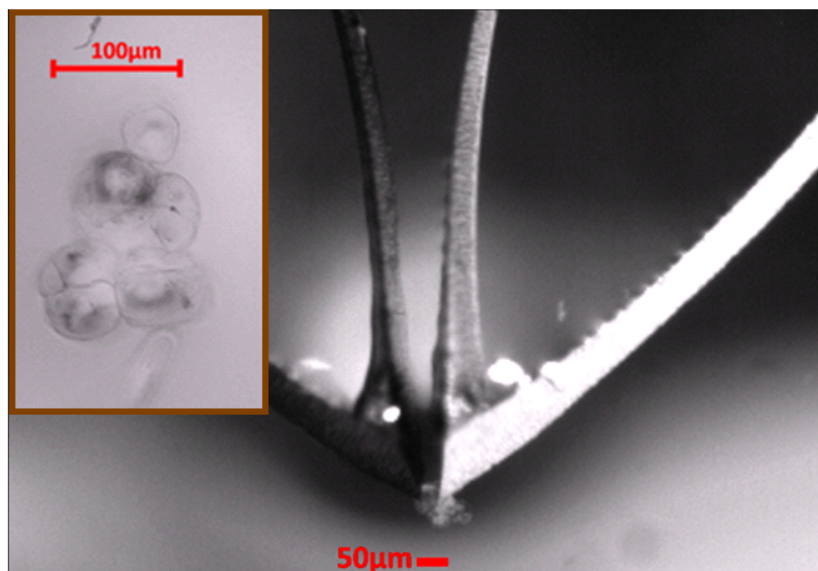


Figure 2-8: Micrograph of a small clump of plant cells held by the micromanipulator. The inset shows a micrograph of the cell cluster.

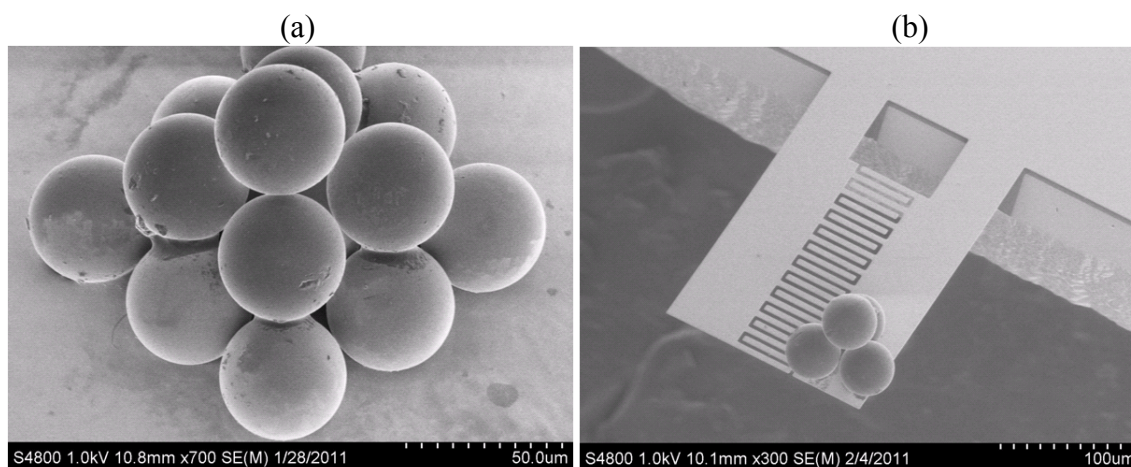


Figure 2-9: (a) SEM image of the three-layer pyramid constructed with 40-μm-diameter beads. (b) Two-layer pyramid of 40-μm polystyrene beads on a cantilever tip.

2.4.2 Microcontact Printing on Selected Areas

Functionalization of micro-areas individually and discretely without contaminating neighboring areas is an important advantage that can eliminate wasting chemicals and allow separate functionalization of an area within a device or multiple areas that are in close proximity. With the current system, a micro-stamp can be used for precise functionalization of discrete spots. In an experiment, a piece of polydimethylsiloxane (PDMS) was used as the stamp material to transfer “ink” to a target surface and fluorescein-isothiocyanate-labeled bovine serum albumin (FITC-BSA, Sigma) as the ink. Figure 2-10a shows nine 40- μm beads arranged in a line formation using the device. The stamp was grabbed and inked using the micromanipulator and brought to contact with selected beads (indicated by arrows in Figure 2-10a). The upper figure in Figure 2-10a is the bright field micrograph, and the lower one shows the corresponding fluorescent micrograph. The result shows fluorescence only from the stamped beads. Figure 2-10b presents another micro-stamping result which features a Purdue ‘P’ logo.

This result demonstrates that the manipulator can apply sufficient pressure on individual beads to transfer the ink without causing the stamp to slip off the tweezer or moving a bead out of position.

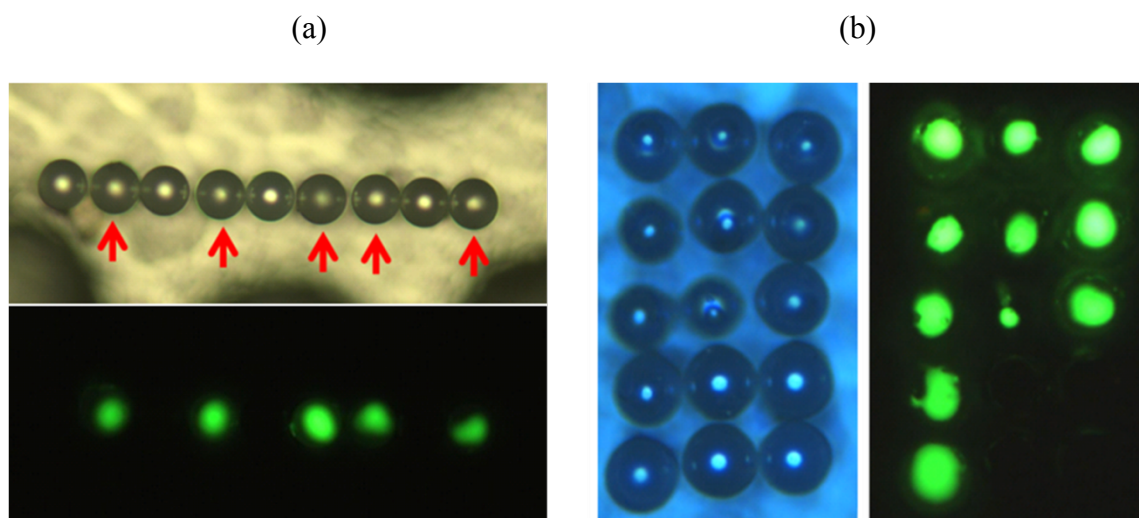


Figure 2-10: (a) Bright field and fluorescence micrographs of microstamped 40- μm beads. The arrows indicate beads stamped by FITC-BSA. (b) Micro-stamping result shows 'P.'

2.4.3 Extraction of Stem Cell Spheres from Culture Media

The ability to discriminate and move individual live cells within or out of aqueous media is important since it allows the device to accomplish tasks of arranging cells in specific patterns, placing them on surfaces of sensors, or isolation of individual cell spheres from culture, as we demonstrate next.

Stem cells grow as multiple spheres in soft agar. Before the cells are interrogated, multiple aspiration and incubation steps are used to separate all of the spheres from the viscous media [78]. This standard procedure not only requires time and reagents but also cannot isolate a single sphere. As a result, many spheres are wasted that could otherwise remain in the media until needed. We were able to isolate a single mouse prostate stem cell sphere directly from the viscous media (Matrigel) that it was suspended in. The tips of the microtweezers were able to reach in the gel and remove a single 100- μm cell

sphere (Figure 2-11). The force provided by the microtweezers was sufficient to compete with the surface tension of the viscous gel but not large enough to damage the cell sphere. Figure 2-11b shows that the cell sphere remained intact after being pulled out of the Matrigel.

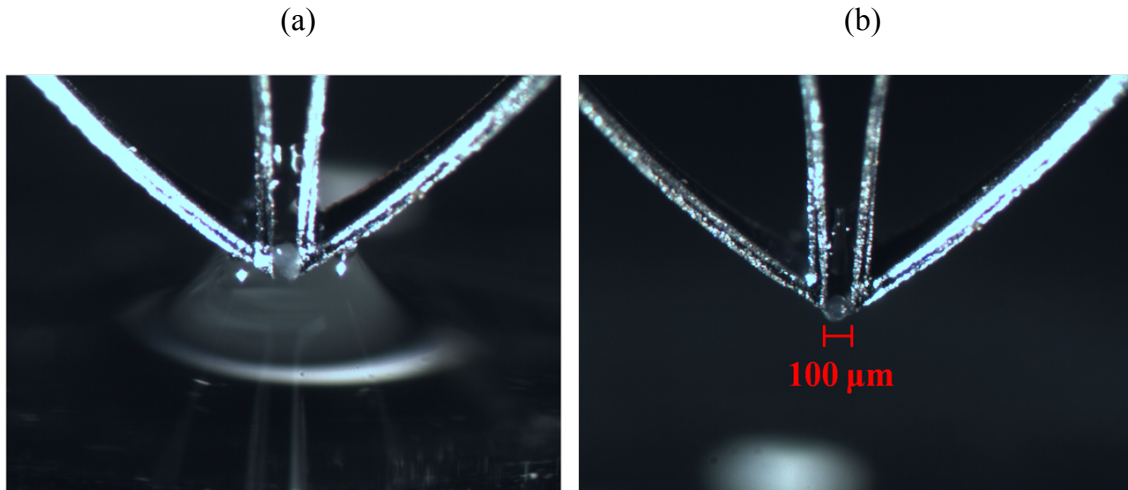


Figure 2-11: Micrographs of (a) a cell sphere being pulled out of viscous Matrigel and (b) cell sphere held by a microtweezer in air.

2.5 Summary

We have developed and demonstrated a compact, portable, and multipurpose micromanipulator that is actuated manually by rotating the thimble of a micrometer head connected to a microtweezer structure via a 3D-printed interface. The operation principle of microtweezers is based on the elastic deformation of silicon, which practically eliminates hysteresis effects and greatly simplifies the overall device design. The device can operate in both air and liquid and transport entities between the two media. Due to its compact and highly portable nature, the device is also capable of transporting entities

from one setting to another. Three applications have been demonstrated in this chapter: With its relatively sharp tips and large dynamic range, the device was able to arrange microspheres in 3-D (including designated spots of sensor surfaces) and perform on-demand microcontact printing. The device was also able to isolate and remove a single stem cell sphere from viscous media without damaging either the sphere or the tweezer.

CHAPTER 3. CANTILEVER-BASED NANOMECHANICAL RESONATOR

In this chapter we present the design, fabrication, operational principles and applications of the cantilever-based nanomechanical resonator. The operational principles of the device are first introduced in Section 3.1. The fabrication process and results are presented in Section 3.2. In Sections 3.3, the experimental setup and results using piezoelectric-actuation are introduced. The frequency response of the resonator is also characterized in terms of loading location and repeatability. In Section 3.4, system verification and uncertainty analyses are performed. Finally, the chapter is summarized in Section 3.5.

3.1 Introduction

Cantilever-based micro/nano sensors have been used extensively over the past decade to detect a wide variety of entities including biomolecules, chemicals, viruses and cells [2, 79-82]. As discussed in Chapter 1, these sensors have been used both in static, i.e. stress sensing, or dynamic, i.e. resonating mode. The latter mode, in which our cantilever-based resonator is operated, reveals directly the mass of the target entity by measuring changes in the resonance frequency of the cantilever. In this study, as shown in Figure 3-1, we utilize a dual-beam cantilever integrated with a diffraction grating for

motion measurement. The device has two identical adjacent cantilevers. Often times one of the cantilevers serves as a reference to test the operation of the system before an experiment using a load with a known mass. The reference cantilever can also serve to account for small disturbances that may affect both cantilevers. In addition, the dual-beam design of the sensor can also be used to directly determine the mass of two different particles in one measurement by loading both cantilevers instead of leaving the reference arm empty.

The relative motion between the two cantilevers is detected directly by illuminating the diffraction grating (or interdigitated fingers in Figure 3-1) between the two cantilevers by a laser beam. The resonance frequency of each cantilever is obtained in a single measurement by observing the intensity of the 0th order reflected diffraction mode that changes in accordance with the deflection between the neighboring cantilevers. Details about the diffractometry-cantilever sensing scheme were described in Chapter 1.

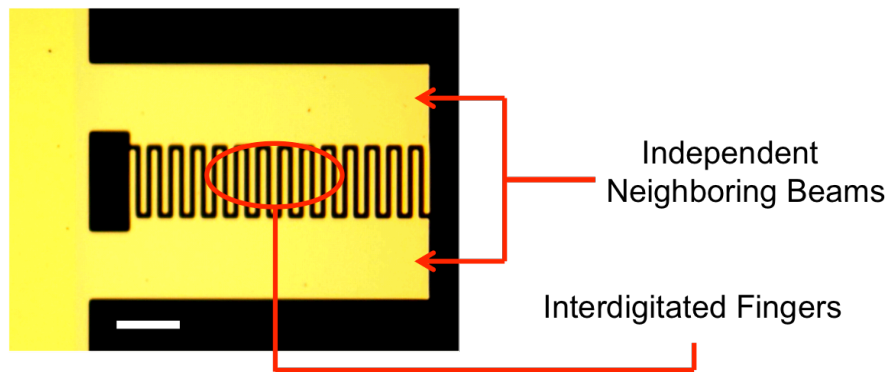


Figure 3-1: Micrograph of a dual-cantilever-based resonator. Scale bar: 50 μm .

3.2 Fabrication of the Dual Cantilever Sensor

The processes used in the microfabrication of the sensing structure include 1) silicon nitride deposition, 2) photolithography, 3) wet etching, and 4) gold deposition.

The 4-inch, 500 μm -thick, single-side polished, $\langle 1\ 0\ 0 \rangle$ silicon wafers were first immersed in piranha and then acetone for cleaning. Next, the silicon wafers were deposited with a 480 nm low-stress silicon-rich silicon nitride layer by LPCVD (low-pressure chemical vapor deposition). After deposition of the nitride layer, a photolithography process was performed to define the cantilever patterns. In this process, AZ-1518 photoresist and Karl-Suss MA6 mask aligner with an exposing power of 8 mW/cm^2 were used to define the cantilever pattern. Next, the wafer was immersed in the AZ-Developer solution to peel off the exposed photoresist. After hard backing in a 120 °C oven for 15 minutes, Plasma Tech was used to remove nitride layer that was not protected by the photoresist; with an etching time of 11 minutes.

The photolithography and the nitride removal processes were then repeated on the backside of the wafer to define the die. After removing the layer on the backside, the wafer was placed into a piranha solution (H_2SO_4 : H_2O = 1:1) and acetone to remove the photoresist. Finally, the wafer was immersed in a 45 % KOH (potassium hydroxide) solution at 80 °C over a period of 7 hours to etch the underlying silicon and release the cantilever structures. A 20 nm gold layer was deposited on the surface of the cantilever to improve the reflectivity. In the process of gold-deposition, an Airco E-beam Evaporator was used to deposit a 1.2 nm Cr adhesion layer and a 20 nm Au layer.

The above mentioned processes are schematically presented in Figure 3-2. Figure 3-3 illustrates a scanning electron micrograph (SEM) image of a cantilever. In addition to

rectangular cantilevers, we also fabricated cantilevers with various shapes that we believed could facilitate weighing micro entities with different geometries. Cantilevers with different shapes are numbered and illustrated in Figure 3-4.

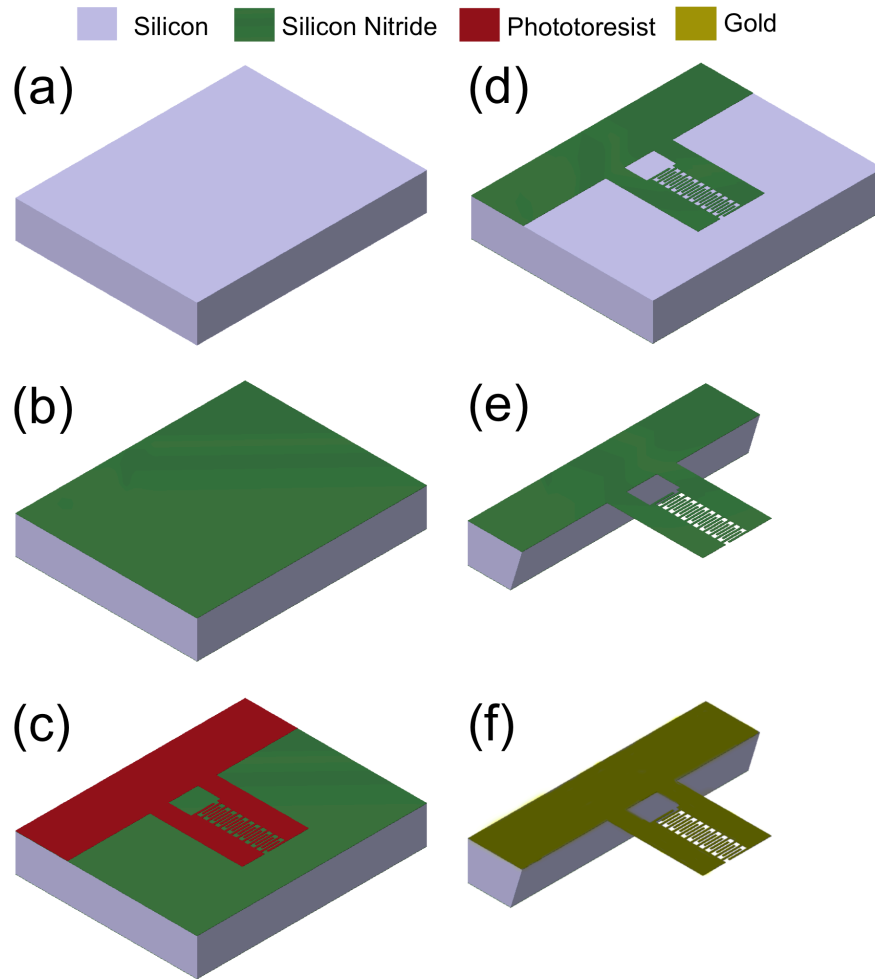


Figure 3-2: Fabrication process flow. Only major steps are presented. (a) $\langle 100 \rangle$ silicon wafer cleaned by piranha and acetone. (b) LPCVD silicon nitride deposition (on both sides). (c) Cantilever patterns defined by photore resist. (d) Silicon nitride removed by Plasma Tech, photore resist removed by piranha and acetone. The processes of photore resist patterning and silicon nitride removal were repeated again on the backside to define die patterns. (e) Device released by KOH solution. (f) Gold deposition.

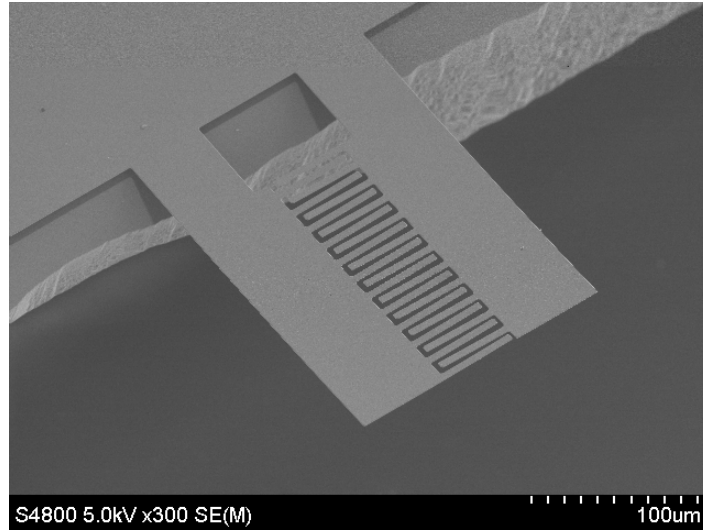


Figure 3-3: SEM image of a dual-beam cantilever.

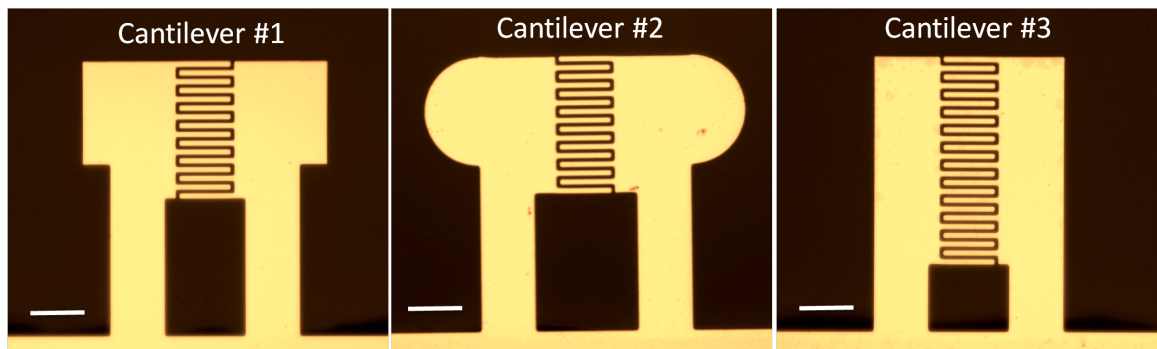


Figure 3-4: Micrograph of different cantilever designs. Scale bar: 50 μm .

3.3 Piezoelectronic Actuation

In this section, we discuss the experimental setup and the experiments of weighing microparticles using the cantilevers described before. It is possible to observe the natural frequencies of our cantilevers without any external actuation: the kT -based thermomechanical actuation is sufficient to excite the cantilever over a broad frequency range that includes resonance [83-86]. However, as also mentioned in Chapter 1, external

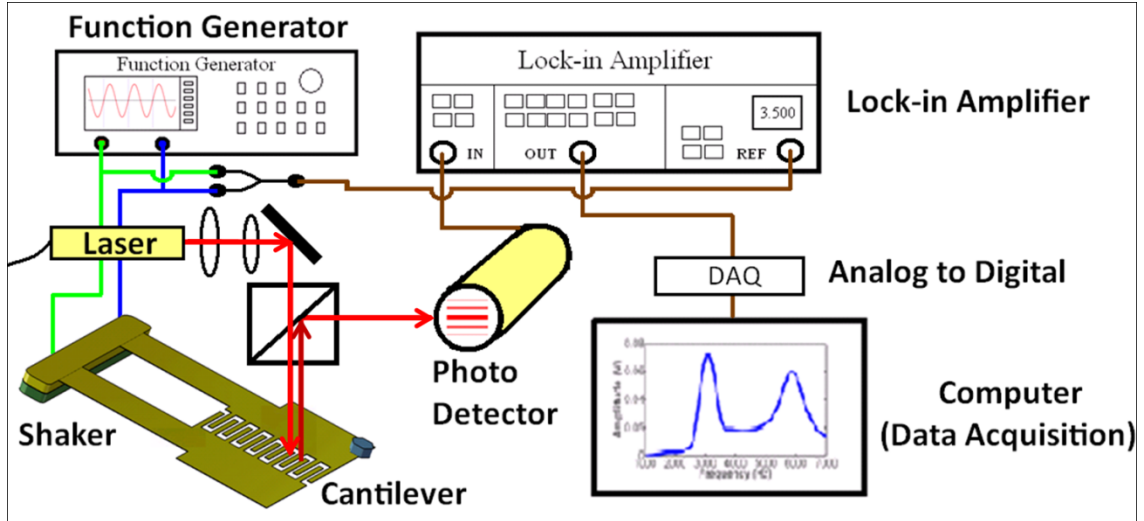
excitation does offer the advantage of improved signal-to-noise ratios and allow better observation of frequency changes [87]. We therefore use a piezoelectric actuator to drive our sensors during measurement.

3.3.1 Experimental Setup

Figure 3-5a demonstrates the experimental setup used to perform the weighing measurements. The coherent illumination is generated by a 632.8 nm Helium-Neon laser (Newport R-30991, 5 mW), and the resulting beam is focused by three lenses. The reflected laser is directed toward the photo detectors by a beam splitter (Thorlabs BS016). The photo detector is composed of a photodiode (12 V reverse-bias, Thorlabs DET110) and an adjustable aperture (Thorlabs SM1D12), which is used to measure the intensity of the 0th mode of the reflected diffraction pattern (Figure 3-5b). A function generator (Tektronix AFG 3102) is used to actuate the piezoelectric shaker. The sinusoidal signal provided by the function generator serves the purposes of both actuating the piezoelectric shaker (Thorlabs AE0203D04F) and providing reference signal to the lock-in amplifier (Stanford Research Systems SR830).

The reflected signal collected by the photodiode is sent to a lock-in amplifier for noise filtering. Output of the filter is connected to a computer for further analyses via a data acquisition interface (National Instrument DAQ). Lastly, a LabVIEW program made in-house is used to collect the data, and a Matlab algorithm is used to smooth the resulting frequency spectrum.

(a)



(b)

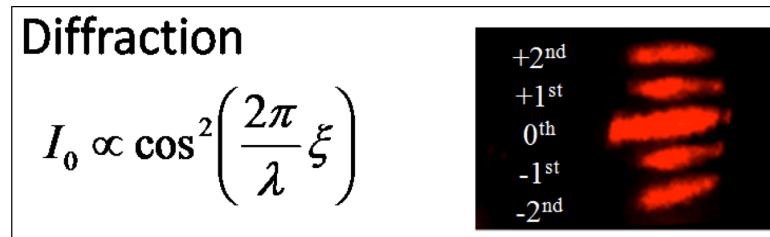


Figure 3-5: (a) Experimental setup of the weight measurement system. (b) First three reflected diffraction modes.

3.3.2 Frequency Response due to Added Mass

Figure 3-6 demonstrates the frequency response of the system (using Cantilever #1) when the sensor arm is loaded with three different masses. In each experiment, an individual polystyrene bead (Spherotech Inc.) with a different mass was placed on the free end of the sensor arm for weighing. A small amount of grease (70 - 200pg) was applied underneath the bead prior to the placement, for improving the attachment

between the bead and the cantilever surface as discussed in Chapter 2. We found that this much grease has negligible mass in comparison with the particles being weighed and can efficiently improve the adhesion between the particles and the cantilever surface. In some measurements where the mass of grease has significant impact on experimental results, such as measuring lighter objects (mass < 5 ng), the effect of grease on frequencies can be directly accounted for by measuring the mass of grease before the target object is placed. The mass derivation process will be described in Section 3.3.3.

In the frequency spectrum of Figure 3-6, the frequencies corresponding to the two peaks represent the resonance frequencies of the sensor (low frequency peak) and the unloaded reference (high frequency peak) arms. Initially, since both cantilevers are empty, no significant frequency separation occurs and two resonance peaks overlap with each other (red curve in Figure 3-6). As the load on the sensor arm increases, the resonance peak corresponding to the sensor arm shifts to the left and the two resonance peaks separate. The resonance frequency of the reference arm stays unchanged because there is no change of mass on the reference arm. The mass of the load on the sensor arm can be derived readily from the resonance frequency corresponding to the sensor cantilever. Since the resonance frequencies corresponding to both arms are shown in the same frequency spectrum, the cantilever-based resonator can also be applied to weigh two objects of different masses in one measurement.

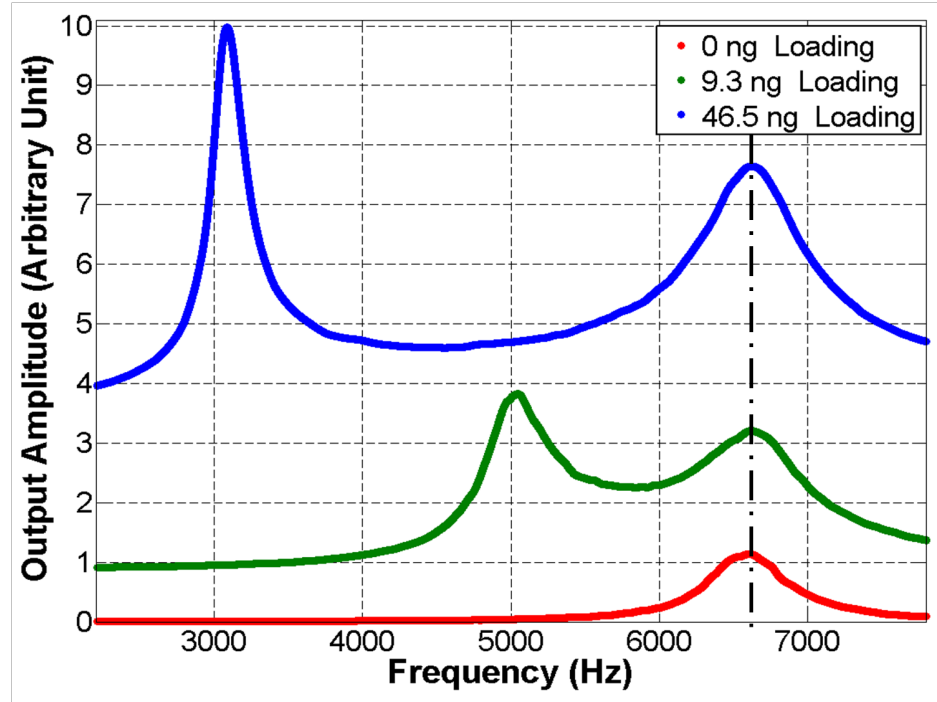


Figure 3-6: The frequency response of system with different mass loads. Resonance frequencies of both the sensor and the reference arms are obtained in a single measurement (The 46.5 ng and 9.3 ng beads were placed 12.2 μm and 11.6 μm away from the tip of the cantilever, respectively).

As discussed in Chapter 1, the resonance frequency of a cantilever depends not only on the mass of the load but also on the location of the load with respect to the tip of the cantilever [88, 89]. We used finite element analysis to demonstrate the dependence of the resonance frequency on the mass and the location of the loaded particle. Figure 3-7 shows the change of the resonance frequency of Cantilever #1 with different loading masses and locations on the sensor arm. It is obvious that both added mass and loading location have an impact on the resonance frequency. To mitigate the effect of loading location uncertainty, in each experiment, the exact location of a loaded particle needs to

be measured by optical microscopy. The effects of loading locations will be further discussed in Section 3.4.2.

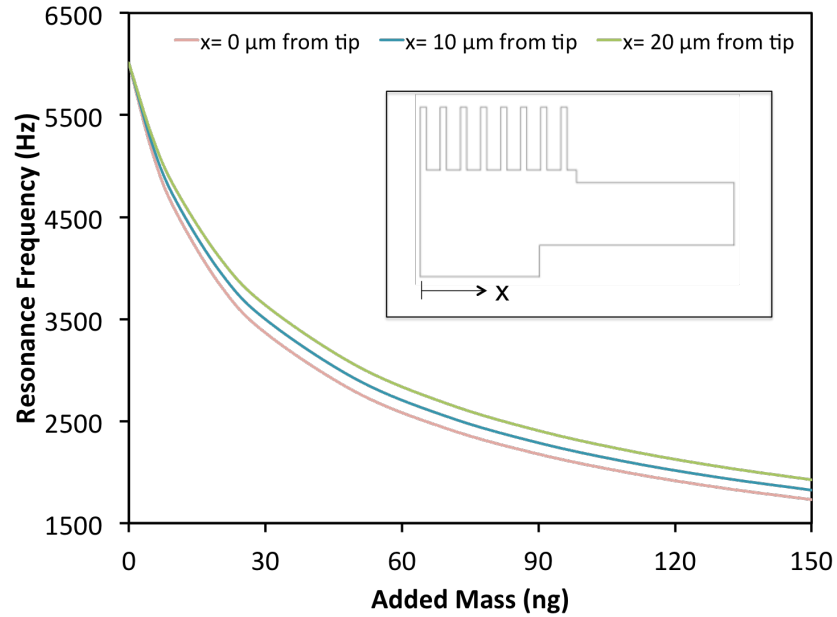


Figure 3-7: The resonance frequency of Cantilever #1 (as shown in inset) with location of the load with respect to the cantilever tip.

3.3.3 Mass Derivation

In this study, we utilize the ABAQUS finite element simulation to derive the mass from the frequencies observed in the experiment. To conduct the simulation, we first characterized the Young's modulus of the particular cantilever in question. The effective density of our cantilever is estimated as 3.65 g cm^{-3} by averaging a 20 nm thick gold layer with a density of 19.3 g cm^{-3} [90] and a 480 nm of silicon-rich silicon nitride layer with a density of 3 g cm^{-3} [91]. The Young's modulus is estimated to be 170 GPa, by matching

the resonance frequency of an empty cantilever predicted by the finite element simulation with that observed experimentally.

To obtain the mass of loaded objects, we match 1) the experimentally observed resonance frequency of the loaded cantilever and 2) microscopically determined location and approximate shape of the loaded objects with our finite element simulation. Figure 3-8a demonstrates the weighing of a *Lasthenia fremontii* pollen grain (left arm). As mentioned before, prior to the placement, a small amount of grease is smeared on the cantilevers to improve the adhesion between the pollen grain and the cantilever surface. On the right arm, a polystyrene bead with a previously measured mass of 39.9 ng is loaded to ensure that the system is functioning properly. Figure 3-8b is the experimental frequency spectrum corresponding to the weighing experiment in Figure 3-8a. The resonance frequency of the sensor cantilever shifted from 7319 Hz (the resonance frequency of an empty cantilever) to 6043 Hz due to the loading of the pollen grain. The resonance frequency of the reference cantilever was reduced to 3342 Hz due to the weight of the reference bead. By introducing these measured resonant frequencies and location of the loaded object into finite element simulation, the mass of the pollen grain was obtained as 4.54 ng.

We verified the accuracy of the weighing scheme by comparing the effective density of polystyrene beads determined by measuring their mass and microscopically observed volume, to their density reported by the manufacturer (Spherotech, Inc.). In this test, Cantilever #3 and an optical microscope were used to individually measure the mass and volume of ten small (measured average diameter 24.8 μm) and ten large (measured average diameter: 41.9 μm) polystyrene beads. The resulting average masses of small and

large beads were 8.37 ng and 40.62 ng respectively. The average densities of ten different beads were then calculated as 1.048 g cm^{-3} for small beads and 1.055 g cm^{-3} for large beads. These results were in good agreement with the density of polystyrene beads reported by the manufacturer ($\sim 1.05 \text{ g cm}^{-3}$).

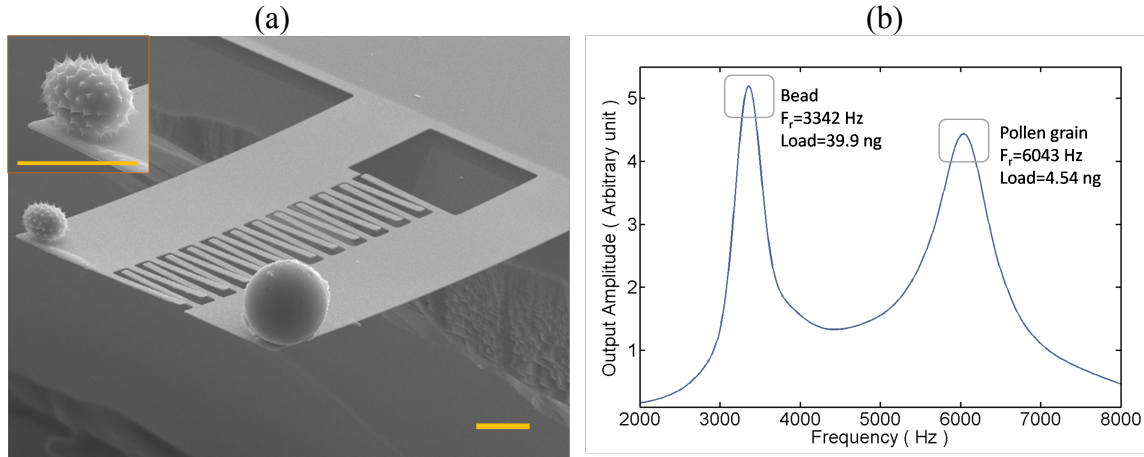


Figure 3-8: (a) SEM image of a pollen grain placed on a cantilever (left arm). The reference cantilever (right arm) was loaded with a polystyrene bead of known mass. Scale bars: $30 \mu\text{m}$. (b) Frequency response of the system that shows the resonance frequencies of both cantilevers.

3.4 Device Characterization

As discussed previously, the resonance frequency of a cantilever depends on both the added mass and loading location on the cantilever. In this section, we first discuss the effective mass and the stiffness of the cantilevers, which can later be used for uncertainty analysis. We next discuss the effect of the loading location on the resulting resonance frequency. Afterward, the repeatability of measurements is studied to achieve an

understanding of the realistic resolution of detectable frequency. Finally, we present an uncertainty analysis of the weighing system.

3.4.1 Determination of the Effective Mass and Effective Stiffness of Cantilevers

We first determined the effective mass (M) and effective stiffness (K_e) of cantilevers by combining the experimental results with finite element simulations. In Section 3.4.2 and Section 3.4.4, these two values will be used to characterize the effect of loading location as well as the systematic uncertainty of the weighing system.


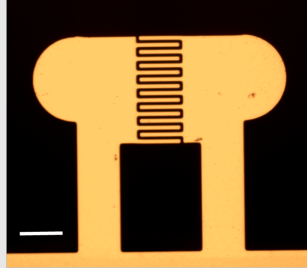
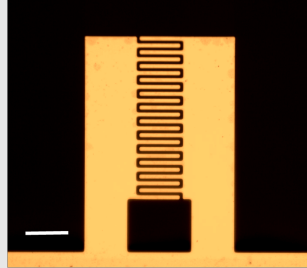
Several studies have presented analytical methods for determining the stiffness of cantilevers. For example, Sader *et al.* [92, 93] estimated the stiffness of rectangular cantilevers from the knowledge of its resonance frequency and quality factor, without requiring the knowledge of cantilever's thickness or density. However, cantilevers used in our study are not perfectly rectangular and Sader's simplistic formulations are not directly applicable. Therefore, in this study k_e and M in Equation (1.4) were determined by combining finite element simulations with experiments.

To obtain k_e and M , we first obtained the effective density and Young's modulus of the used cantilever by the procedure presented in Section 3.3.3. Afterward, the effective stiffness (k_e) was determined by simulating the tip deflection due to a point load using a finite element simulation. Finally, the effective mass (M) was determined by substituting the resonance frequency of the empty cantilever (f_0) and k_e into Equation (1.4). The k_e and M values of different cantilevers used in this study are summarized in

Table 3-1.

It should be noted that k_e and M of different cantilevers could vary even with identical geometry. Since a wafer is fabricated with many devices on it, a user may assume the same properties for all cantilevers on the same wafer. This can lead to errors since dimensions could differ slightly (possibly due to alignment errors during photolithography). For example, according to our measurement, the change in thickness due to non-uniformity of nitride deposition was measured as 8 nm over a 3 inches range on a wafer, which for a thin film with 500 nm-thickness, could alter the stiffness of a cantilever by 4.9% (cubic dependence on thickness) and its mass by 1.6% (linear dependence on thickness). According to Equation (1.4), the combined effect of this on a cantilever's natural frequency (with nominal M of 11.202 ng and k_e of 0.0195 N/m) would be about 106 Hz. We also found that the length of two cantilevers that are 2 inches apart on the wafer can differ by as much as 1 μm . For a 250 μm long cantilever, the effect of this uncertainty on stiffness can be about 1.2 %, and on mass 0.4 %, the combined effect of which can be a 53 Hz uncertainty on resonance frequency. Therefore, in order to account for the variation between different cantilevers, the above mentioned calibration process has to be carried out for each specific cantilever.

Table 3-1: Effective stiffness (k_e), effective mass (M) and resonance frequency (F_r) of different shapes of cantilevers. The cantilever types corresponding to different numbers are shown in Figure 3-3. Scale bars: 50 μm .

	Cantilever #1	Cantilever #2	Cantilever #3
k_e (N/m)	0.0195	0.0188	0.0182
M (ng)	11.202	13.171	8.634
f_0 (Hz)	6642	6010	7319
Type			

3.4.2 Effects of Loading Position on Resonance Frequency

As shown in Section 3.3.2, the location of the loaded particle can affect the resonance frequency of a cantilever. This effect can be predicted by [94, 95]:

$$f_r = \frac{1}{2\pi} \sqrt{\frac{k_e}{M + g_b(x)^2 m}}, \quad (3.1)$$

where f_r is the resonance frequency of cantilever, M and k_e are respectively the effective mass and effective stiffness of the cantilever, m is the added mass, and $g_b(x)$ is:

$$g_b(x) = 1 - \frac{3}{2} \left(\frac{x}{L} \right) + \frac{1}{2} \left(\frac{x}{L} \right)^3, \quad (3.2)$$

where L is the length of the cantilever and x is the distance of the load away from the tip of the cantilever. As a load is moved away from the free end of a cantilever, the denominator in Equation (3.1) decreases and thus the resonance frequency of the cantilever increases. Unlike Equation (1.4) that assumes the added mass being placed exactly at the tip of the cantilevers, Equation (3.1) factors in the effect of loading location (x) and hence provides a more accurate estimate.

Figure 3-9 presents the relationship between the loading location, added mass and the resonance frequency of the loaded cantilever. The modeled cantilever is Cantilever #3 as illustrated in Figure 3-4. Circles and curves in this figure represent the results obtained from the finite element simulation and Equation (3.1), respectively. The trend indicates that the sensor does not “feel” the added mass as much when it moves away from the tip. In this study, we address this issue by 1) using the micromanipulator to place a load as close to the tip as possible to ensure a better mass sensitivity, and 2) measuring the actual position of the load and accounting for the effect of location when determining the added mass.

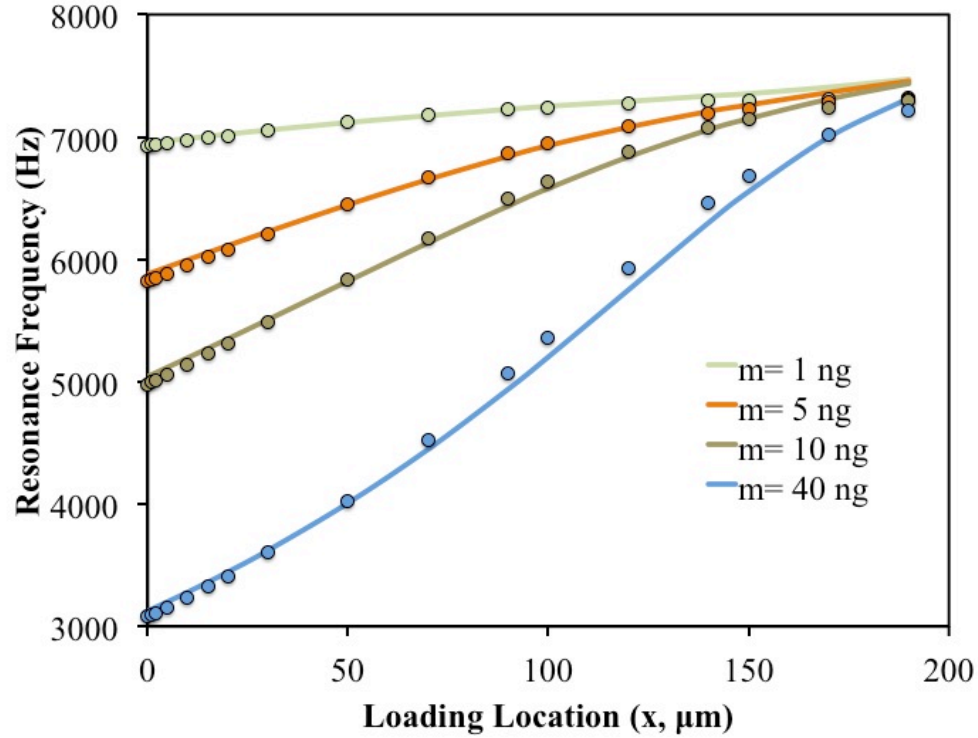


Figure 3-9: Dependence of resonance frequency, added mass (m) and loading position (x). Curves represent prediction of Equation (3.1) and circles represent finite element simulations.

3.4.3 Uncertainty in Mass Measurement

We examined the systematic uncertainty in our mass measurements by evaluating the uncertainties in determining the location of a loaded particle as well as that in the frequency measurements. The uncertainty in the loading location is introduced by the resolution limit of the optical microscope used. The uncertainty in the frequency measurement is due to the effects of both the quality factor of the cantilever and the signal-to-noise ratio, as well as other drifts in the system. To quantify the uncertainty in both the location and the frequency measurements, we conducted experiments in which

the resonance frequency of a cantilever (Cantilever #3) and the location of a polystyrene particle loaded on a cantilever were repeatedly measured. The location of a polystyrene bead (24.8 μm in diameter) was repeatedly measured twenty times by means of calibrated brightfield microscopy. The 99.7 % confidence interval for the resulting uncertainty in location was 0.16 μm for a bead that was on average located 8.3 μm away from the tip of the cantilever. The uncertainty in the resonance frequency was obtained by measuring the resonance frequency of the loaded cantilever ten times. In this experiment, the excitation voltage was 3.0 V and the resulting average resonance frequency was measured as 3345 Hz (which gave the mass of the bead as 39.7 ng) with an uncertainty of ± 0.89 Hz at the 99.7% confidence level.

The effect of the uncertainties in the measured location (δx) and frequency (δf), on the uncertainty in the mass measurement (δm) was then calculated using an error propagation approach:

$$\delta m = \sqrt{\left(\frac{\partial m}{\partial f} \delta f\right)^2 + \left(\frac{\partial m}{\partial x} \delta x\right)^2}, \quad (3.3)$$

where m is the mass of the load that can be derived from Equation (3.1):

$$m = \frac{k_e - M_c(2\pi f_r)^2}{g_b(x)^2(2\pi f_r)^2}. \quad (3.4)$$

As shown Figure 3-9, the general trend of resonance frequencies predicted by finite element simulation agrees with that described by Equation (3.1). However, a more careful investigation of the figure shows that the mismatches between the FEM simulation and the analytical model could be considerable for larger loads placed at larger distances from the tip. This mismatch is smaller for small values of x , (e.g. < 50

μm). In our experiments, with the use of the micromanipulator, the target objects are generally placed close to the tip of the cantilever ($x < 20 \mu\text{m}$). Therefore, Equation (3.4) serves an appropriate model that can be used in conjunction with Equation (3.3) for uncertainty analysis. The effective stiffness (k_e) and effective mass (M) of the tested cantilever (Cantilever #3) were previously determined as 0.0182 N/m and 8.634 ng as shown in Table 3 - 1.

Figure 3-10 shows the resulting dependence of the calculated mass uncertainty (δm) on the added mass (m) and the loading location (x). According to Figure 3-10, the uncertainty in mass is 3.2 pg for a 1 ng load (when $x = 0$). This uncertainty increases to about 82 pg when the added mass is 40 ng . The effect of location uncertainty is less severe as the uncertainty in the mass of a 1 ng load increases only from 3.2 pg to 3.8 pg when x increases from 0 to $20 \mu\text{m}$.

We next compared the calculated uncertainties with the experimentally observed variations in mass. We used two groups of 10 beads for this analysis, one group with an average diameter of $24.8 \mu\text{m}$ ("small beads"), and one with an average diameter of $41.9 \mu\text{m}$ ("large beads"). We first picked one bead from each group and weighed it 10 times. Each weighing was performed from scratch where the same bead was weighed, removed from the cantilever surface, placed back on the cantilever and weighed again by recording the new frequency and the bead location. The resulting variation in mass measurements as well as the systematic uncertainty predicted by Equation (3.3), at the 99.7% confidence level are shown in Figure 3-11. The similarity between the experimental and the calculated uncertainty values indicate that the uncertainties in the frequency and location measurements are an important part of the overall systematic uncertainty. Next, we

studied the variation of mass from one bead to another in each group, where we weighed each bead from each group once. In each experiment, the mass of the grease on the sensor surface was measured before beads were placed on the cantilever so that the measured frequencies only represent the mass of the beads. These results are also presented in Figure 3-11 as well as Table 3-2, and indicate that bead-to-bead variation in mass, even for beads from the same group, greatly outweigh the systematic uncertainty in the mass measurements.

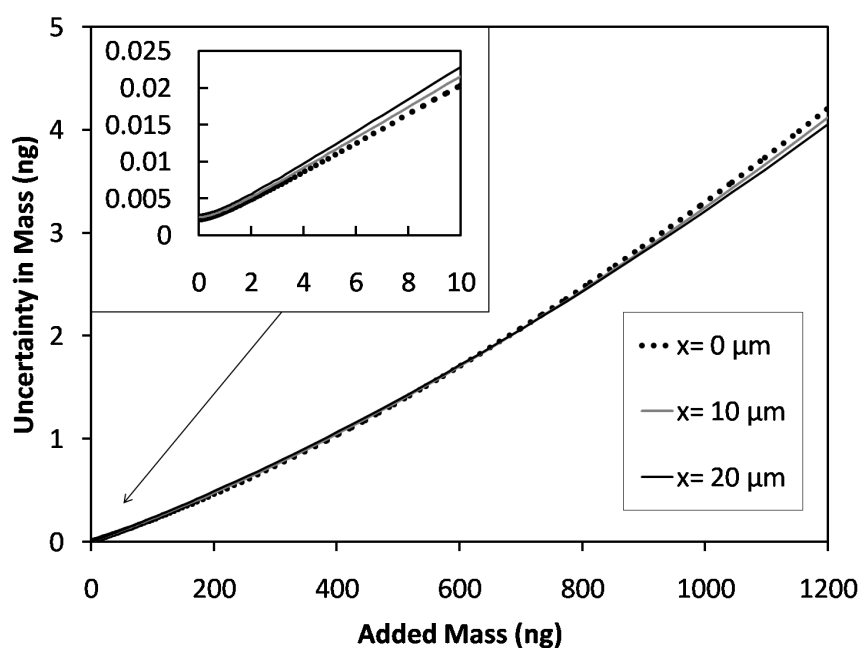


Figure 3-10: The theoretical uncertainty in mass with respect to the mass and location of the attached matter. 'x' denotes the distance of the load away from the tip of the cantilever.

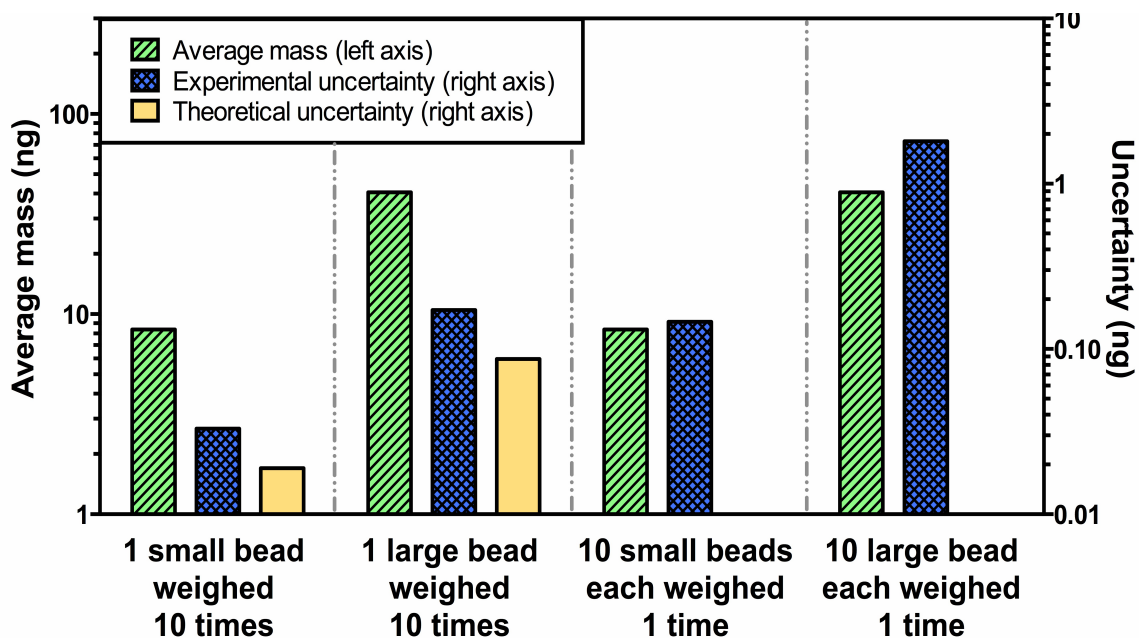


Figure 3-11: The bar chart illustrates experimental and theoretical uncertainties in mass for single beads ($n=10$). The average masses and experimental uncertainties in mass of ten different beads are also presented.

Table 3-2: Experimental and theoretical mass uncertainties at the 99.7% confidence level.

Sample	Mean mass (ng)	Experimental Error (\pm ng)	Theoretical Error (\pm ng)
1 small bead weighed 10 times	8.38	0.033	0.019
1 large bead weighed 10 times	40.56	0.172	0.087
10 small beads each weighed 1 time	8.37	0.146	NA
10 large bead each weighed 1 time	40.62	1.810	NA

3.4.4 Comparison of Experimental and the Ultimate Theoretical Mass Uncertainty

In this study, the added mass is determined by measuring the resonance frequency of the loaded cantilever. Therefore, the resolution of frequency measurement (δf_0 in Hz or $\delta \omega_0$ in rad/s) has a direct impact on the mass resolution. Although we determine our minimum detectable frequency experimentally, which automatically accounts for all possible uncertainties and noise sources, it is informative to compare this with the ultimate limits of a system in the absence of all uncertainties except for thermal noise. Such a model has been reported by Ekinici *et al.* [48]. Accordingly, the ultimate minimum detectable frequency of a thermomechanically driven cantilever can be expressed as:

$$\delta \omega_0 \approx \left[\frac{K_B T}{E_c} \frac{\omega_0 BW}{Q} \right]^{1/2} . \quad (3.5)$$

Where E_c represents the maximum drive energy:

$$E_c = M \omega_0^2 \langle x_c \rangle^2 \quad (3.6)$$

with M being the modal mass, ω_0 the resonance frequency, and $\langle x_c \rangle$ the RMS oscillation amplitude. In our study, for an unloaded Cantilever #3, quality factor (Q) is 16.4, angular resonance frequency (ω_0) is 45986.6 rad/s ($f_0 = 7319$ Hz), the approximate measurement bandwidth (BW) to define a resonance peak ($\sim f_0/Q$) is 446.3 Hz, and the effective mass of the cantilever (M) is 8.634 ng. The RMS amplitude of the resonator $\langle x_c \rangle$ can be estimated using the product of the amplitude of external excitation to the base of the cantilever (A) and the quality factor of the measurement ($\sim A*Q/\sqrt{2}$). For a 3.0 V peak-to-peak excitation voltage, A (provided by our piezo stage) is 45 nm and hence $\langle x_c \rangle$ is approximately 521.8 nm. With the above information, $\delta \omega_0$ is calculated as 1.02 rad/s or 0.16 Hz. This value is small in comparison with what we obtained experimentally in the

previous section for a loaded cantilever (~ 0.89 Hz). In fact, it will be even smaller if the effect of a 40 ng load is included in the calculation. The difference is not surprising as Ekinici's formulation is an ultimate theoretical limit (derived for $Q > 10,000$) and considers the thermomechanical noise as the only source of uncertainty. In comparison, our experiment provides a realistic estimation of frequency uncertainty, which accounts for every source of error that could have contributed to our frequency uncertainty, such as drifts in frequency measurements. However, Equation (3.5) does demonstrate that the frequency uncertainty of measurement can be improved by utilizing an external drive as well as increasing the modal mass of a cantilever. According to Equation (3.5), with an enhanced excitation (increasing x_c), E_c is increased and hence $\delta\omega$ is decreased. In addition, with an increased modal mass (M), quality factor of the system is also increased according to [96]:

$$Q = \frac{1}{2\xi} = \frac{\sqrt{k_e M}}{c}, \quad (3.7)$$

where ξ , k_e , M , c represent the damping ratio, spring constant, effective mass, and damper constant of the cantilever, respectively. From Equation (3.6) and Equation (3.7), an increase in the nominal load on the cantilever not only increases the external excitation energy (E_c) but also improves the quality factor, both resulting in an improved frequency uncertainty.

We verify the effects of both external excitation and nominal load to frequency resolution by observing the repeatability of our frequency measurements. We loaded the sensor cantilever with an individual polystyrene bead with a known mass and varied the peak-to-peak excitation voltage. Two different loads (0 ng and 46.5 ng) were tested and

each experiment was repeated five times at each excitation voltage. The standard deviation of the measured resonance frequency was then calculated. In the study, Cantilever #1 is used, and the average resonance frequencies corresponding to 0 ng and 46.5 ng added masses were measured as 6642.8 Hz and 3081.5 Hz. The experimental results are shown in Figure 3-12. Figure 3-12 agrees with Equation (3.5) which demonstrates that an improvement of frequency resolution can be achieved by increasing both external excitation and nominal load on the cantilever. This however, does not imply that an increased load will ultimately lead to an increased mass resolution. In fact, the fundamentally nonlinear nature of the system results in smaller changes in resonance frequency as the total mass of the system increases. This effect ultimately outweighs the improvement in the external energy as well as the quality factor of the system, which can be explained by Equation (1.8) that indicates the ultimate mass resolution of an externally driven and thermomechanically limited resonator [47]:

$$\delta M \approx 2M \left(\frac{E_{th}}{E_c} \right)^{1/2} \left(\frac{BW}{Q\omega_0} \right)^{1/2}. \quad (3.8)$$

Using the parameters in Equation (3.5) and Equation (3.6), Equation (3.8) predicts an ultimate mass resolution of 0.38 pg which is about an order of magnitude smaller when compared with the smallest uncertainty value in Figure 3-10. This is expected, since, as mentioned before, Equation (3.8) only assumes limitation by thermal noise, and does not take the effect of the loading location into account. Equation (3.8) does suggest that the mass resolution can be improved by increasing external excitation (E_c). Hence, in our measurements, we use excitation voltages larger than 2.5 V to maximize the external

energy input into the system. However, with an increased load on cantilever, the mass uncertainty is increases which is also shown in Figure 3-10.

Due to the relatively low quality factor of our cantilevers, the resonant peaks of the two cantilevers could sometimes be difficult to differentiate from one another when the added mass is small (i.e. when the two peaks overlap). When this happens, we have the option to load the reference cantilever with a bead and separate the resonance frequencies of the two cantilevers. This also increases the effective mass of the reference cantilever and hence improves our ability to resolve its resonance frequency.

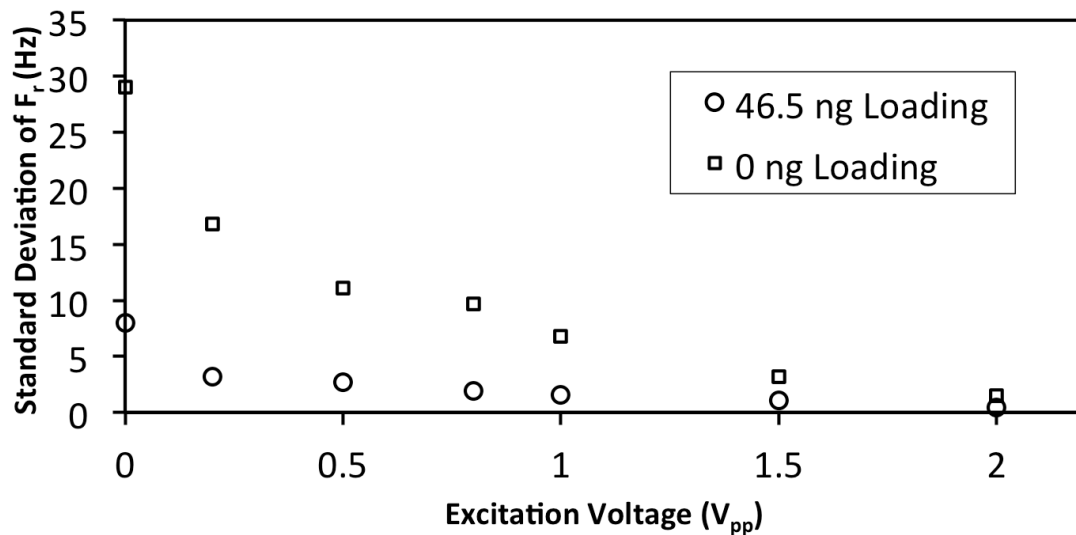


Figure 3-12: Dependence of the standard deviation in the measured frequency on the excitation voltage and loading.

3.5 Summary

In this chapter, we have presented a cantilever-based resonator that can be used to measure the mass of individually selected single microparticles. The resonator has two

adjacent cantilevers that constitute a sensor/reference pair. By matching the experimentally measured resonance frequency of the loaded cantilever and the location of the load with a finite simulation model, the mass of load can be determined. We validated the accuracy of the weighing method by measuring the density of polystyrene beads, and the result was in good agreement with that reported by the manufacturer. Finally, we performed a hybrid experimental/analytical study of the measurement uncertainty, that we believe is a more realistic representation of the mass resolution of the system than what is predicted by theoretical models provided in literature that predict ultimate resolutions.

CHAPTER 4. SELECTIVE WEIGHING OF INDIVIDUAL MICROPARTICLES

In this chapter, we demonstrate the weighing of individual dry biological microparticles by discretely picking and placing them on a resonator for mass measurement (similar to a typical weighing scenario in a supermarket). A single target entity that is selected under a microscope is first grabbed by a mechanically actuated micromanipulator whose fabrication and basic operation were described in Chapter 2. The entity is then moved and placed on the tip of the sensor arm of the cantilever for weighing. The concept is schematically shown in Figure 4-1. Due to the ease of use and the maneuverability of the micromanipulator, and the large surface of the cantilever-based resonator, this weighing approach is highly compatible with established laboratory practices to provide mass information for a wide variety of microparticles. We utilized the present weighing scheme to measure the dry mass of individual cancer cells, prostate stem cell spheres, and cancer cells that are bound to other particles and those that have been dissected by focused ion beam milling. We finally demonstrate the weighing of a wide variety of biological microparticles over a high dynamic range (from 10s of pictograms to micrograms).

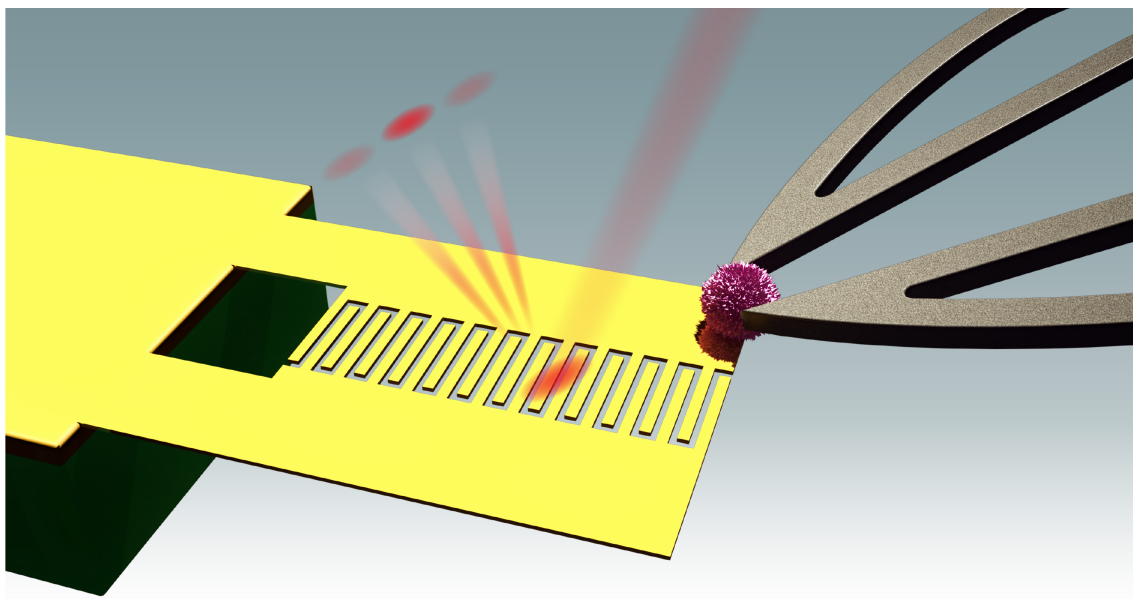


Figure 4-1: Schematic of the measurement strategy for selectively weighing individual micro-entities.

4.1 Dry Mass Measurement of Biological Microparticles

Measuring the dry mass of biological entities has sparked great interest because this simple physical property can provide unique insight into many fields including biology, pathology, and ecology. For example, studies showed that the dry mass of individual yeasts could be used as an effective way to study the synthesis of new cellular material during cell growth [97, 98]. Researchers also used the dry mass to monitor the growth of cells [99, 100], as well as demonstrating the change of cell mass in response to chemicals [60, 69]. In several studies of environmental biology and ecology, the mass of airborne pollens was correlated with the pollen transportation and gene flow [101-103]. The dry mass of microorganisms was also used to determine the metabolic rate that represented the energy needed to sustain life [104-106].

Several approaches regarding the measurement of the dry mass of biological microparticles have been reported. It has been shown that the dry mass of bacteria can be estimated by using their carbon content [107] or electron opacity values determined by electron microscopy [108]. Optical interferometry methods [71, 100, 109-112] were also used to observe temporal changes in the dry mass of live cells. However, to use methods that do not directly weigh particles, assumptions about their optical or material properties have to be made. In addition, the measurement accuracy can be affected by experimental conditions such as debris in fluid [71] or speckle generated by the illumination sources [100]. Researchers have used nanomechanical resonance to demonstrate characterization of cells in terms of their mass [65, 71, 113, 114]. As presented in Chapter 1, the Manalis Group at MIT used the suspended microchannel resonators (SMR) to estimate the dry mass of cells in suspensions that flow through the interior channels of a microfluidic structure [66, 68]. Here we use the combination of a micromanipulator and cantilever-based resonator to directly measure the dry mass of *individually selected* biological microparticles as opposed to weighing them in multiplicity.

Cells and microorganisms are often dried to obtain scanning electron microscopic (SEM) images. With proper fixation and drying procedures [115], the geometries and interior structures of dried samples can be preserved and be recognized under an electron microscope. Several studies report using the electron microscope to conduct pathological or morphological analyses of dried biological microparticles including cancer cells [116], *Drosophila* embryos [117, 118], erythrocytes [119, 120], and pancreatic islets [121-124]. In addition to SEM imaging, drying procedures are also used in conjunction with other procedures and tests such as focused ion beam milling [125], microorganism preservation

[126], and mass spectrometry [127]. With the method we present here, the mass of a wide variety of dried biological particles can be directly and individually measured, and be readily used to complement their morphological, structural or chemical properties.

4.2 Preparation of Cancer Cell and Blood Cell Samples

4.2.1 Cultivation of Cancer Cell Lines

Human cancer cell lines were obtained, cultured, fixed and dried for weighing experiments. The breast cancer cell line MCF-7, obtained from American Type Culture Collection (ATCC), was cultured in Eagle's Minimum Essential Medium (EMEM, ATCC) with 10% fetal bovine serum (FBS, Gemini Bio Products). The lung cancer cell line A549, obtained from Indiana University School of Medicine, was cultured in F-12K Medium (ATCC) with 10% FBS. KB cells, a HELA subclone obtained from Purdue University Department of Chemistry, was cultured in folic acid depleted RPMI 1640 medium (Gibco) with 10% FBS. All three cell lines were harvested using Trypsin-EDTA (Invitrogen) before going through a series of fixing, dehydration, and drying processes further described in Section 4.2.3 "*Fixation, dehydration and drying of cell samples*".

4.2.2 Preparation of Blood Cells

Red blood cells (RBCs) and leukocytes were isolated from blood samples of healthy donors under an approved IRB protocol and subjected to weight measurement. Blood samples were first collected in BD vacutainer tubes with additives of sodium polyanethol sulfonate (SPS) and were kept at 4 °C immediately after collection until blood cell isolation. Blood samples were used within two hours after collection. To

obtain RBCs, 4 mL of the collected blood was first transferred into a tube and centrifuged at 400 g for 20 minutes. RBCs were subsequently collected from the bottom of the tube using a pipet tip. Leukocytes (mainly lymphocytes) were isolated from another 4 mL of blood using Ficoll-Paque PLUS (GE Healthcare) by following the standard protocols provided by the vendor.

4.2.3 Fixation, Dehydration and Drying of Cell Samples

Cells and microorganisms were first fixed by 2 % glutaraldehyde in 0.1 M cacodylate for 30 minutes. After rinsing by cacodylate buffer (0.1M, pH 7.4), cells and microorganisms were post-fixed by 1% osmium tetroxide (OsO_4) in 0.1 M cacodylate for 30 minutes. These two fixation steps can effectively retain proteins and lipids in cells [128, 129]. The series of fixation procedure has been commonly used as a method to stabilize the interior structures of cells and tissues when preparing them for scanning electron microscopy (SEM) and dissection [130, 131]. The samples were then subjected to a series of dehydration processes in ethanol with varying concentrations (10, 30, 50, 70, 90, 100 for 10 minutes each). Afterward, cells were re-suspended in 50% and 100% *hexamethyldisilazane* (HMDS) solutions for 10 minutes each. HMDS has been shown to replace the critical point drying (CPD) method as an effective and economical way to dry biological samples [132-134]. It has been demonstrated that HMDS induces only a small amount of surface tension and hence prevents cell structures from collapse and distortion introduced during air-drying [135-137].

4.3 Weighing of Individual Stem Cell Spheres of Different Inflammation States

Our system is unique in the sense that it can easily manipulate and measure the mass of a specifically selected micro-entity. In this section, we use our system to differentiate between different types of prostate stem cell spheres based on their masses and densities.

Prostate stem cells (PSC) are able to self-renew and differentiate into mature cells in order to compensate tissue injury. It is currently believed that these cells play a role in prostate cancer initiation and progression [138, 139]. To study the biological properties of prostate stem cells and the associated therapeutic applications, the sphere-forming assay is extensively utilized where stem cells grow into 3 dimensional clusters or ‘spheres’ in soft agar. Here, we apply our weighing system to study the impact of inflammation on PSC by comparing the dimension, dry mass, and effective density between regular (naïve) and inflammation regulated (inflamed) PSC spheres.

In this study, the adolescent mouse prostate stem cell spheres were provided by Prof. Ratliff and Hsing-Hui Wang from the Purdue University Center for Cancer Research. After being isolated from Matrigel (BD Bioscience), prostate spheres were first fixed using paraformaldehyde and then air-dried on a glass slide. Next, individual spheres were picked up by the micromanipulator under a microscope and placed on the cantilever-based resonator for weighing. Figure 4-2a illustrates the SEM image of a prostate sphere located on a cantilever for mass measurement. The dry mass of the specific sphere in Figure 4-2a was measured as 279 ng according to the frequency spectrum in Figure 4-2b. The volume of the sphere was then determined based on the microscopically observed diameter and the assumption that the sphere was a perfect

spheroid. Finally, the effective density of the loaded prostate sphere was calculated as 1.13 g cm^{-3} by dividing the measured mass by its effective volume. In addition to measuring one object each time, the present method can also weigh two objects with two different masses simultaneously. Figure 4-3a illustrates a SEM image of two prostate spheres placed on different cantilevers for a simultaneous mass measurement. With the frequency spectrum shown in Figure 4-3b, the masses of both cell spheres were derived as 114 ng for large sphere and 25.8 ng for small sphere.

Figure 4-4 shows the average volumes, masses, and effective densities of 42 naïve and 37 inflamed PSC spheres. The measured average mass, volume, and effective density of naïve PSC spheres were $105.83 \pm 56.09 \text{ ng}$, $96182 \pm 49927 \text{ }\mu\text{m}^3$, $1.11 \pm 0.11 \text{ g cm}^{-3}$ (mean \pm 1 standard deviation); and the average mass, volume, and effective density of inflamed PSC spheres were $234.32 \pm 218.51 \text{ ng}$, $175241 \pm 147355 \text{ }\mu\text{m}^3$, $1.292 \pm 0.144 \text{ g cm}^{-3}$. As seen in Figure 4-4, inflammation regulated PSC generated significantly larger, heavier, and denser prostate spheres in comparison to what naïve PSC did (Student t-test, $p < 0.05$).

This is an ongoing project in collaboration with the Tim Ratliff Group of the Purdue University Center for Cancer Research. At the present, although we are not completely certain what causes the inflamed spheres to have higher mass and volume, it might be possible that the inflammation regulated PSCs are more proliferative and therefore generate heavier and larger spheres within the same cultivation time. The result of inflamed prostate spheres being denser can be explained by an observation of the inner structures of prostate spheres. According to Wang *et al.* [140], prostate spheres generated by inflamed PSC have significantly higher percentage of tubule-like (or double-layered)

spheres (41.4 %) than that generated by naïve PSC (21%). The interior of tubule-like spheres (or inner layer of spheres) is filled with proteins [140, 141] which have a higher density ($1.4\sim 1.5 \text{ g cm}^{-3}$ according to [142]) than the rest of the sphere (Figure 4-4c). Therefore, our result of higher average density for inflamed prostate spheres suggests that inflamed prostate spheres may indeed have higher percentage of tubule-like structure than naïve ones.

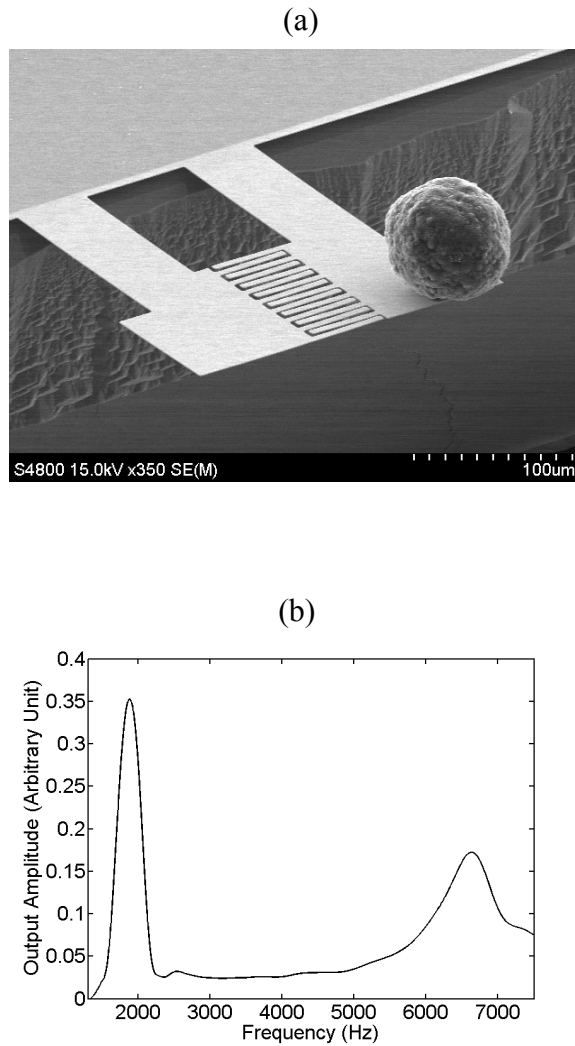


Figure 4-2: (a) SEM image and (b) corresponding frequency spectrum of weighing a PSC sphere. The system used is referred to as Cantilever #1 in Chapter 3 [140].

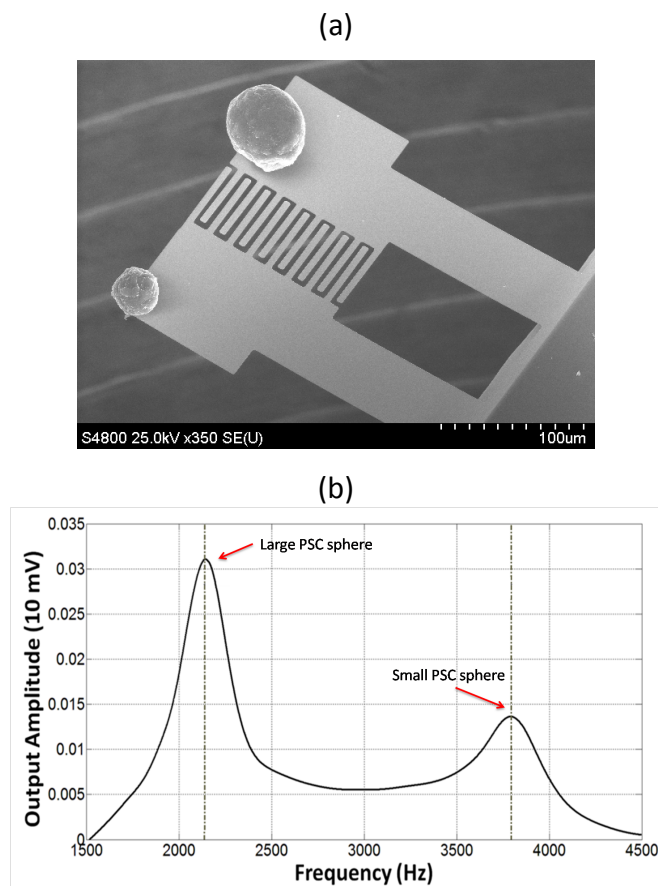


Figure 4-3: (a) SEM image and (b) the resulting frequency spectrum showing the simultaneously weighing of two different stem cell spheres.

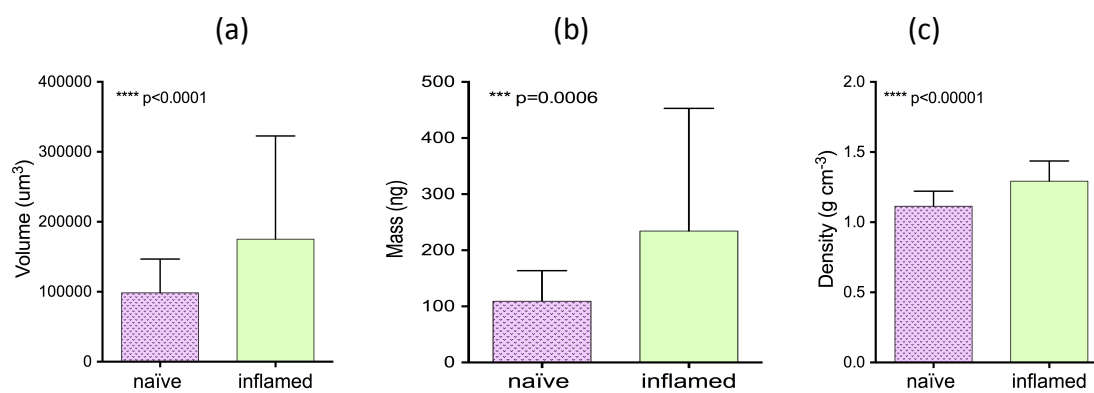


Figure 4-4: Measured average (a) volume, (b) mass, and (c) density of naïve and inflamed prostate spheres. Error bar: +1 SD.

4.4 Arrangement of Single Particles on Resonator Surface

In Chapter 2 we demonstrated the capability of the micromanipulator to perform particle-by-particle construction of micro structures on various substrates including surfaces of the cantilevers used in this study [143]. With this capability, we can build structures by combining individual particles on the tip of a resonator and readily weigh these structures. This becomes especially useful for weighing particles smaller than $\sim 15\ \mu\text{m}$. It is often easier to maneuver and place a small particle on top of a larger spherical particle already placed on the cantilever surface than it is to directly place it on a two-dimensional cantilever surface. Figure 4-5a is an example of a cell-bead stack built on a cantilever surface. To build this stack, a polystyrene bead (orange) was first placed on the cantilever. Next, the top of the bead was “painted” with a layer of grease (purple) to improve adhesion. Afterward, an individually targeted KB cell (green) was placed on the bead using the micromanipulator.

To obtain the mass of the specific KB cell in Figure 4-5a, the resonance frequency of the cantilever with the bead/grease combination was first determined. After the cell was placed on top of the bead, the resonance frequency of the cantilever corresponding with the bead/grease/cell combination was measured again. Subsequently, the measured resonance frequencies as well as the locations of the bead and cell were used in a finite element simulation to determine the mass of the cell. The mass of the dry KB cell in Figure 4-5a was determined as $0.52 \pm 0.019\ \text{ng}$ (measured mass \pm theoretical systematic uncertainty). We also applied the method to weigh smaller biological particles such as red blood cells (Figure 4-5b). The resulting mass of the specific dry red blood cell in Figure 4-5b was $57 \pm 18\ \text{pg}$. Note that in this case, using a heavier base particle under the

relatively small red blood cell increases the systematic uncertainty. Therefore, the measurement resolution can be improved by choosing a lighter base particle such as a smaller bead.

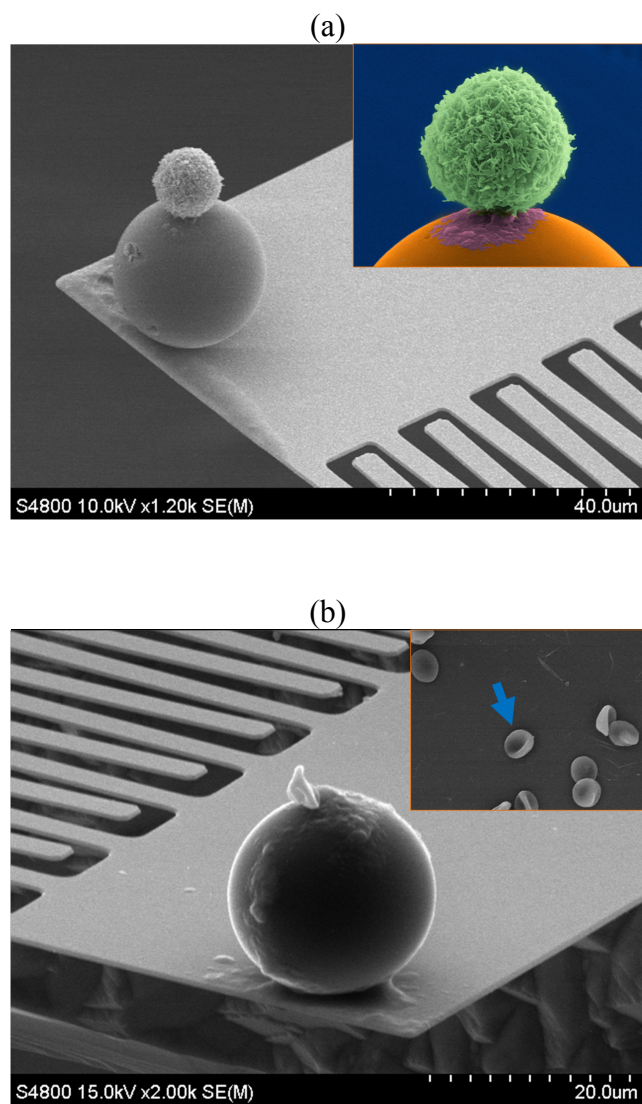


Figure 4-5: SEM images of microparticles measured by the cantilever-based resonator. (a) KB cell was placed on top of a polystyrene bead for weighing. The inset shows the side view of the cell-bead stack. The green part indicates the KB cell, purple is the adhesive grease layer, and orange is the polystyrene bead. (b) Weighing of a red blood cell. A red blood cell was selectively picked up from a scatter of cells (inset) by the micromanipulator.

4.5 Weighing of Individually Selected Cancer Cells

Knowing the mass of a cell can be extremely valuable. For example, researchers have shown that they can investigate the effects of chemical or clinical treatments on tumor cells by observing their masses [60, 61]. Others have shown that the dry mass of cells can be associated with cellular senescence and cell growth [58, 71, 144]. With our approach, a particular cell can be individually isolated and weighed. Figure 4-6a shows individual cancer cells that were selectively weighed by our system. In this experiment five A549 cancer cells were selected from the surface of a glass slide that contained numerous dried A549 cells, and weighed. After the weighing, the A549 cells were removed from the cantilever and arranged on a conductive substrate for SEM imaging. With this particular protocol that combines SEM imaging and on demand weighing, detailed spatial information as well as the mass of individual cells can be obtained as shown in Figure 4-6a.

The developed method can also be used to characterize individual cells that are attached to other particles. For example, magnetic particles are frequently used in immunomagnetic separation to isolate specific cells from heterogeneous cell suspensions [145, 146]. This analysis often relies on a balance between magnetic, fluidic and gravitational forces applied on cells in question and hence the mass of the individual cell-bead assembly. Using our method, the mass of an individual cell that is attached to magnetic particles can be determined and compared to that without particles. This information can be useful for accurate simulations of magnetic flow-based separation systems and the overall optimization of the system [147, 148]. Here, we incubated KB cells with magnetic beads (Sigma-Aldrich) conjugated with antibodies against folate

receptor (anti-FR, R&D systems) for 90 minutes. Afterward, bead-bound cells were collected by a magnet [149], followed by a re-suspension in a fixing agent (Glutaraldehyde). After a series of fixation, dehydration and HMDS-drying steps described before, individual bead-attached and bare KB cells were analyzed using our weighing system.

Figure 4-6b shows a comparison of KB (with and without beads), A549, as well as MCF-7 cancer cells. The average dry masses of bead-bound KB, bare KB, MCF-7, and A549 cells were measured as 1.05 ± 0.40 , 0.76 ± 0.15 ng, 0.43 ± 0.13 ng, 0.61 ± 0.13 ng, respectively (mean \pm 99.7% confidence interval, Figure 4-6b). Notice that the error bars in Figure 4-6b indicate cell-to-cell variation in mass, not the systematic measurement uncertainty that is less than 20 pg (as discussed in Chapter 3). It was observed that dried KB cells were on average heaviest of all three cell lines, whereas MCF-7 cells were the lightest. For KB cells, it was observed that bead-bound KB cells were on average 0.2 ng heavier than bare KB cells. The greater variation observed in the mass of bead-bound KB cells is expected and most likely due to variation in the number of beads bound to each cell during incubation.

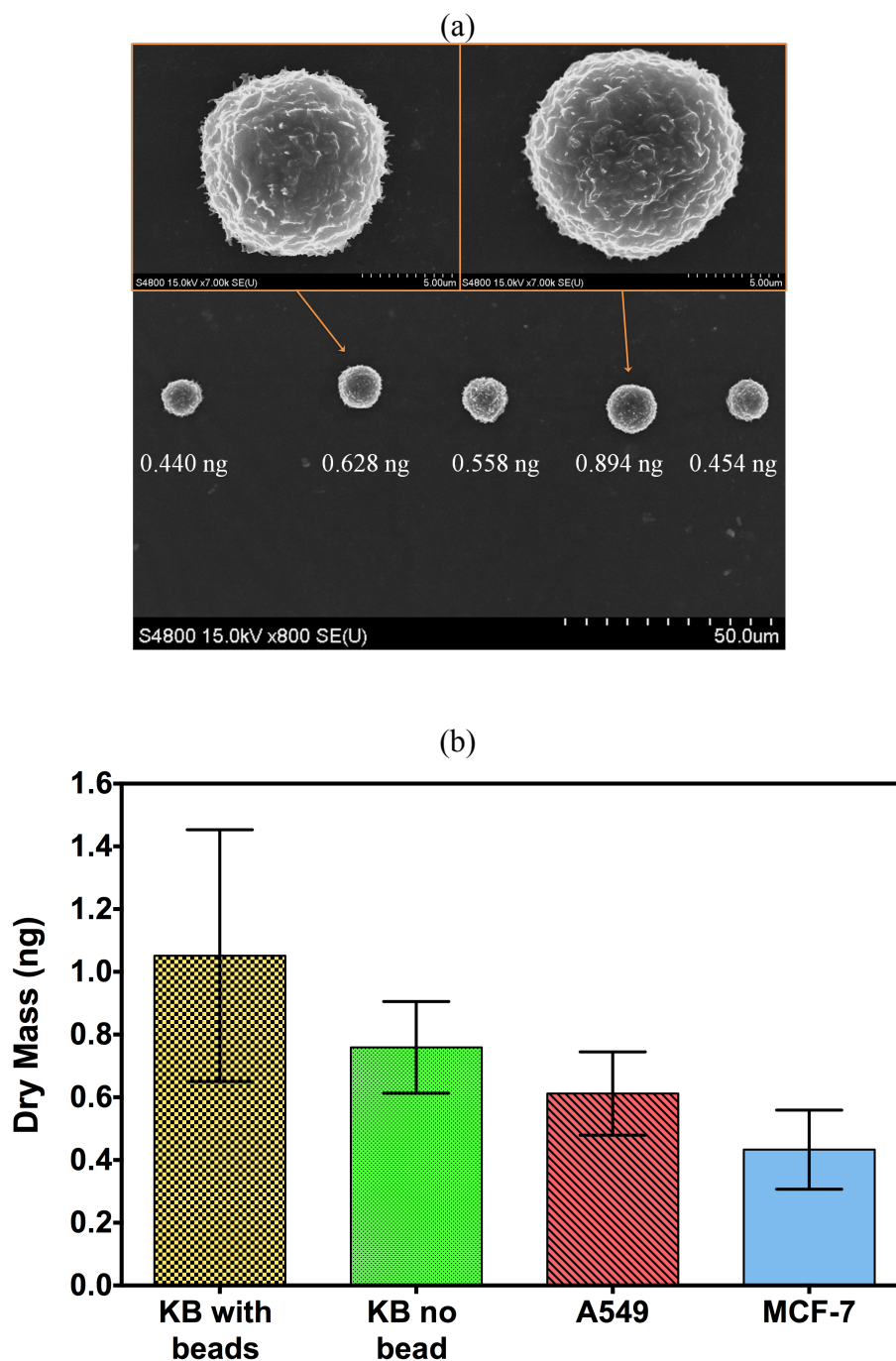


Figure 4-6: (a) SEM image of measured A549 cells with their corresponding dry masses. The theoretical uncertainty of the measured mass was around 20 pg. (b) The dry mass of bead-bound KB cells and bare KB cells are compared. The dry mass of A549 and MCF-7 cancer cells were also presented. Error bars represent +/- 99.7% confidence interval of cell-to-cell variation (not the systematic uncertainty in measurements which is far smaller).

4.6 Weighing in Conjunction with the Focused Ion Beam Cell Milling Process

The developed method can also be utilized to individually characterize fragments or parts of whole cells. To demonstrate this capability, an individual KB cell was chosen from an array of KB cells that have been weighed individually (Figure 4-7a) and arranged on a conductive tape substrate. Subsequently, the targeted cell was sectioned by means of focused ion beam (FIB) milling technique as illustrated in Figure 4-7b~7d. The FIB cell milling procedure is detailed in Appendix B. After the milling process, the remainder of the target KB cell was picked up by the micromanipulator and weighed again. It was measured that the dry mass of the specific cell in Figure 4-7 was reduced from 790 ± 19 pg (mean \pm theoretical systemic uncertainty) to 220 ± 19 pg after the milling process. Figure 4-8 illustrates weighing of a sectioned K9-TCC cell. The cell mass was reduced from 862 ± 3 pg to 483 ± 2 pg after the milling process. Since the dimensions of K9-TCC cells were generally larger than $15 \mu\text{m}$, we did not load the cell above a base particle (as seen in Figure 4-8c and d). As a result, the theoretical systematic uncertainty of weighing K9-TCC cells is smaller than that of weighing KB cells. FIB milling is normally used to prepare sections of samples for electron microscopy, while avoiding the distortion in cellular structures that can result from conventional mechanical sectioning processes [150]. Our system can readily be combined with FIB milling to interrogate parts of individual cells or various biological particles in terms of their mass.

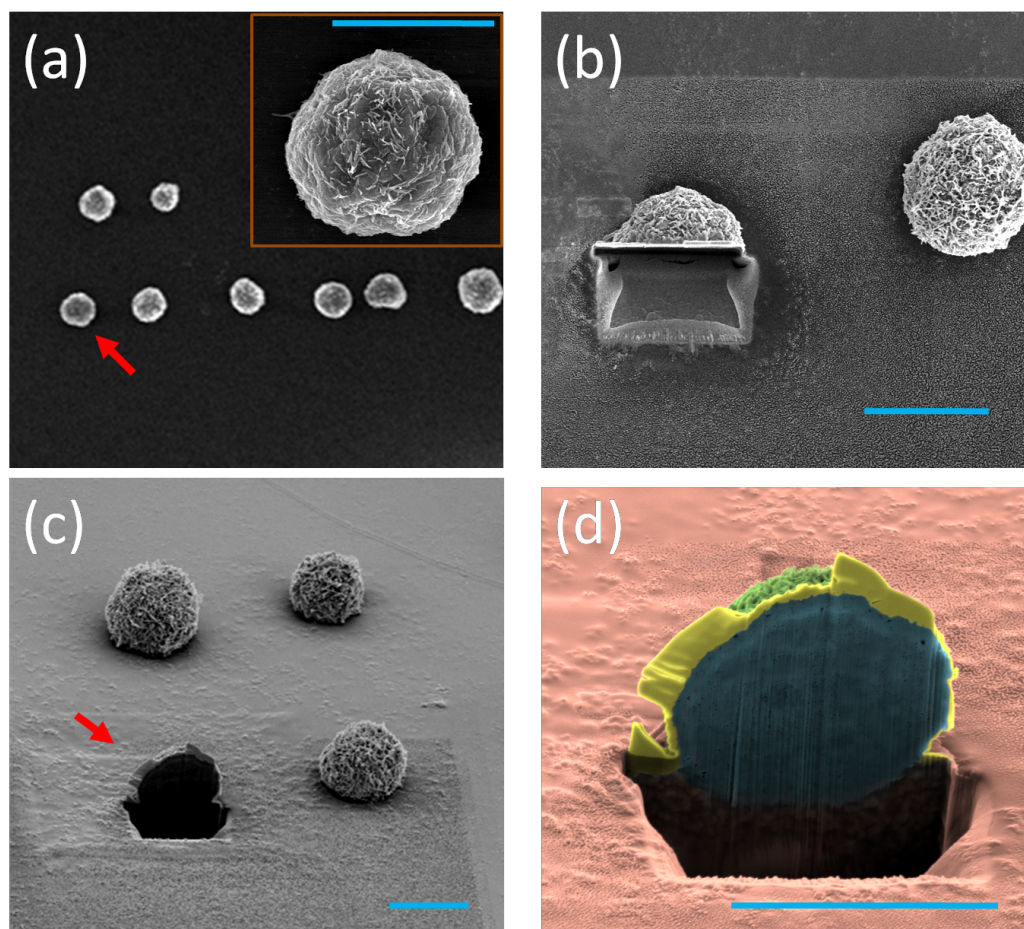


Figure 4-7: (a) SEM image of an array of KB cells arranged individually after being weighed. Red arrow indicates the specific cell to be milled by FIB. (b) Top view and (c) tilted view of the milled cell. (d) The artificially colored SEM image illustrates the cross-section of the milled KB cell. The green and blue parts represent the surface and interior structure of cell, the yellow part is the thin platinum layer that is deposited to protect and define the milling edge, and the pink part depicts the conductive substrate. Scale bars denote 10 μm .

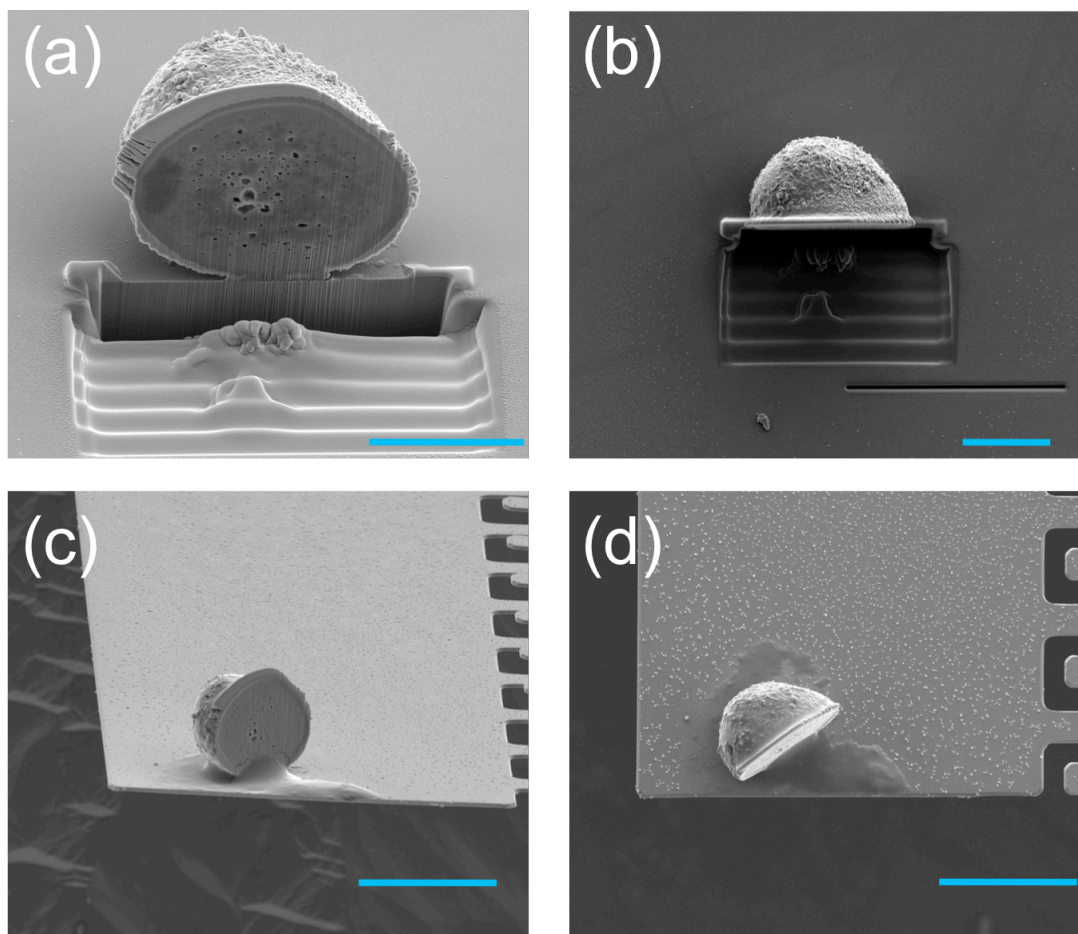


Figure 4-8: SEM images of the (a) top view and (b) tilted view of the milled K9-TCC cell. The substrate was glass. (c) Tilted view and (d) top view of a milled K9-TCC located on a cantilever. Scale bars: (a) and (b) are 10 μ m, (c) and (d) are 20 μ m.

4.7 Characterization of Microparticles over a High Dynamic Range

The weighing scheme is advantageous in its robustness and versatility in selectively weighing individual microparticles over a high dynamic range of mass. The specific prong design allows the manipulation of particles with dimensions between 5 μm and 300 μm [143]. Also the large surface area (50 μm by 250 μm) of the cantilever facilitates the placement of microparticles with various sizes. We characterized the dry mass of wide variety of microparticles including (in the order of increasing size) red blood cells, white blood cells, cancer cells, canine bladder cells, pollen grains, micro beads, stem cell spheroids, pancreatic islet spheroids as well as the eye-brain complexes of insects.

In the weighing experiment, pollen grains from *Lasthenia fremontii* and *Lasthenia glabrata* species were obtained from Purdue University Departments of Biological Sciences and Botany & Plant Pathology (courtesy of Prof. Nancy Emery). Pollen grains were collected on glass slides by tapping the flowers that contained the grains. Diatoms were collected from outdoor pond water. Each diatom was air dried without any fixation or dehydration processes. Mouse pancreatic islet spheroids were provided by Prof. Jenna Rickus of the Department of Agricultural and Biological Engineering, Purdue University. As mentioned before, mouse prostate stem cell spheres were provided by Purdue University Center for Cancer Research. Stem cell spheres were fixed with paraformaldehyde after isolation from Matrigel (BD Bioscience). The eye-brain complexes of *drosophilae* were provided by the Department Biochemistry, Purdue University.

Figure 4-9 demonstrates that our weighing system can readily load and measure the mass of microparticles with complex geometries, including single pennate-type diatom [151-155] and pollen grain from *Lasthenia fremontii* [156-158] (shown in Figure 3-8a). The mass of the diatom is measured as 4.40 ng. Figure 4-10 and Table 4-1 summarize the results of a tandem weighing/SEM analysis performed on 12 different kinds of entities. The dimensions of the measured particles ranged from 5 μm (red blood cells) to 190 μm (eye-brain complex of drosophila). Here, the error bars represent the sample-to-sample variation for all data points except the pancreatic islet and the eye-brain complex where only one sample was available for analysis. For these two data points, the systematic measurement uncertainties are 1.66 ng and 10.25 ng, which are too small to visualize in Figure 4-10.

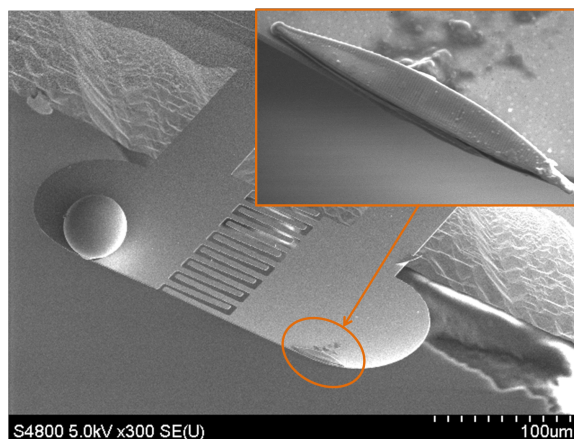


Figure 4-9: SEM image of the weighing of a diatom (right arm). The inset depicts a magnified view of the diatom on the cantilever tip. The cantilever used is Cantilever #2 shown in Chapter 3.

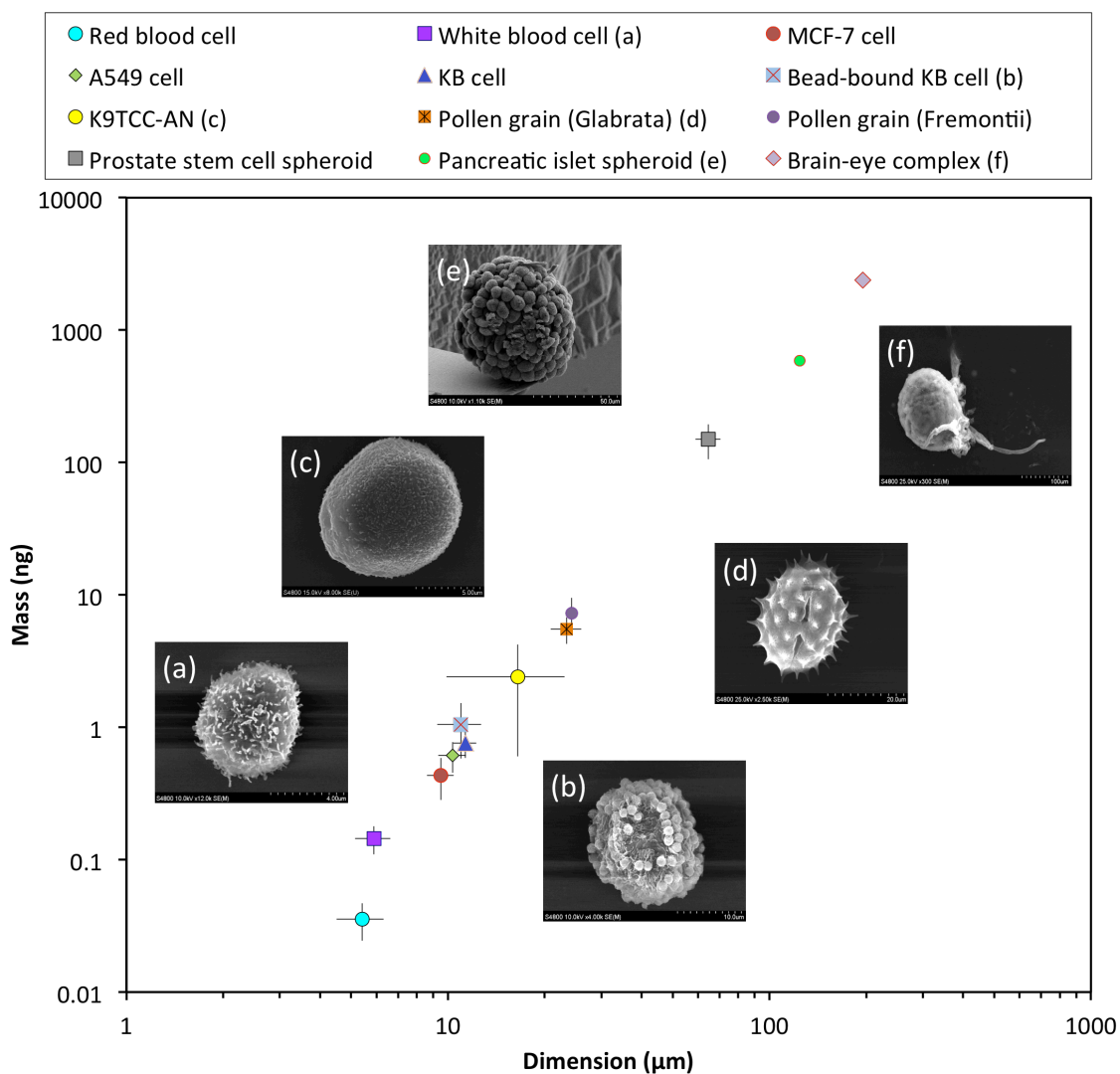


Figure 4-10: Summary chart of all measured biological microparticles. Insets show the SEM images of measured targets including (a) a white blood cell, (b) a bead-bound KB cell, (c) a K9TCC-AN cell, (d) a *Lasthenia Glabrata* pollen grain, (e) a pancreatic islet spheroid from mouse, and (f) an eye-brain complex collected from *drosophila* larvae. Error bars represent $\pm 99.7\%$ confidence interval. Pancreatic islet spheroid and brain-eye complex have sample size = 1 therefore no error bars are shown.

Table 4-1: Mass and dimension of measured biological micro-entities. Dimension indicates the diameter of a spherical particle or the long axis of an oval particle such as a pollen grain. Mass and dimension variation denote the value of 99.7% confidence interval.

Sample	Sample size	Average mass (ng)	Mass variation (ng)	Dimension (μm)	Dimension variation (μm)
Red blood cells	8	0.04	0.01	5.76	0.48
White blood cells	9	0.14	0.03	5.8	0.75
MCF-7 cells	20	0.43	0.15	9.51	0.91
A549 cells	20	0.61	0.16	10.36	1.01
KB cells	20	0.76	0.17	11.33	0.94
KB cells with beads	20	1.05	0.47	10.97	1.72
K9TCC-AN	9	2.41	1.8	16.48	6.6
Pollen grains (<i>Glabrata</i>)	14	5.51	1.24	23.42	2.56
Pollen grains (<i>Fremontii</i>)	14	7.28	2.25	24.25	1.01
Stem cell spheres	10	149.56	44.24	64.63	5.79
Islet Spheroids	1	586	NA	124	NA
Eye-brain complex	1	2395	NA	195	NA

4.8 Summary

In summary, we have demonstrated the application of the micromanipulator-resonator system for selectively and individually measuring the mass of various microparticles. To prepare dried biological samples, we have introduced a two-step fixing process followed by a chemical drying technique that can preserve the morphology of cells during the dehydration and drying processes. By applying the weighing method on PSC spheres, we found that inflamed prostate spheres are on average larger, heavier, and denser than naïve ones. These results suggest that inflamed PSC may be more proliferative and generate larger percentage of tubule-like spheres. We also introduced the method of cell-bead stacks to facilitate the procedures of placing and removing smaller biological entities including cancer cells and blood cells to and from the sensor surface. With the method of cell-bead stacks, we were able to compare the mass of individual cancer cells. Moreover, we also combined our weighing scheme with other standard experimental methods to provide complimentary mass information of bead-bound cancer cells as well as fractions of cancer cells. Finally, we demonstrated the weighing of various biological microorganisms over a wide dynamic range from 10s of pictograms to micrograms.

CHAPTER 5. SUMMARY AND FUTURE WORK

5.1 Summary

The main goal of this thesis study was to develop a facile and versatile method for selecting and weighing individual microparticles. The weighing scheme, which was designed to mimic the simple and intuitive nature of a typical select-and-weigh experience in a supermarket, comprises a mechanically driven micromanipulator and a cantilever-based resonator. The use of the micromanipulator can effectively improve the specificity in picking and analyzing a desired micro-entity and allow placing it at the tip of the cantilever for an accurate mass measurement. With this system we were able to measure the masses of biological particles that weigh some 10s of picograms. It is possible to find mass measurement techniques in the literature that can resolve far smaller masses. However, these systems are significantly more complicated both in terms of fabrication and the associated experimental setups. Furthermore, they mostly rely on probabilistic attachment of the target particles on sensor surfaces, which not only results in errors in determining the associated mass but also makes it challenging to weigh an individual particle chosen by the user. The system we have developed is capable of detecting a wide range of particles that are biologically significant in a simple and accurate manner.

In this study, we performed the weighing of a variety of individual biological microparticles whose masses ranged from 10s of picograms to micrograms. We further used the system to weigh cells bound to other particles, as well as in conjunction with focused ion beam milling to measure fractions of cells. In addition, we also demonstrated the potential of our system to help solve biological problems by studying the weights of naïve vs. inflamed prostate stem cell (PSC) spheres. Our results demonstrated that the inflammation-regulated PSC generated larger, heavier, and denser prostate spheres, which may indicate a higher proliferation potential for inflamed PSCs and a relatively greater ratio of tubule-like prostate spheres generated by inflamed PSCs. Finally, we also conducted the weighing of a wide variety of microparticles that vary from a red blood cell ($\sim 10^{-11}$ g) to the eye-brain complex of an insect ($\sim 10^{-6}$ g), covering a 5-order-of-magnitude mass range.

We expect this versatile system to have a wide range of applications including analysis of individual cell's response to drugs or chemical treatments and comparative analysis of individual pollen grains as well as offering interesting possibilities such as autopsy of insects.

5.2 Future Work

This study shows an easy, direct, and inexpensive way to measure the mass of various microparticles. However, there are still many studies that can be performed to further improve the performance as well as extend the applicability of the system.

First, in order to measure smaller microparticles such as bacteria, both the maneuverability of the microtweezer and the sensitivity of the cantilever-based weighing

device can be improved. To reduce the smallest size the microtweezer can control, the sharpness of the microtweezer tip needs to be improved by refining the manufacturing process. To improve the sensitivity of the cantilever-based resonator, it may be more desirable to operate the cantilever at higher resonant modes, or increase the resonance frequency of the first mode by modifying the geometry of the cantilever.

Second, the micromanipulator can be applied to analyze rare circulating tumor cells (CTC) isolated from blood samples by other appropriate microfluidic platforms. [148]. These systems often capture other unintended cells alongside the CTCs that are aimed. Hence, the micromanipulator can be employed to directly retrieve a single cell from the chip surface of the microfluidic device that has captured it and place it in another container for the subsequent DNA analysis without suffering from the impurities that may be introduced by other cells that were unintentionally captured. This application can greatly improve the specificity of the follow-up analyses after the CTC detection processes. Furthermore, the system can be used to weigh these single cells, which can provide an additional phenotype to characterize and differentiate them from normal cells.

Third, several studies have suggested that the density of cellular microparticles can reveal important information such as different cell growth stages of cells as well as the impact of chemical treatments on cells. In Chapter 4, we also demonstrated that the density information is directly related to the inflammation status of PSC spheres. Therefore, in order to obtain the density of microparticles of various geometries, an effective and accurate volume measurement tool is needed to work in conjunction with our weighing system. Currently, there are plenty of methods that can measure the volume of microparticles such as white light interferometry [159] and confocal microscopy [160].

By combining both mass and volume measurement tools, we can investigate the density response of biological microparticles to treatments of other factors.

Fourth, we are currently utilizing our system to measure the mass of pollen grains from *Lasthenia fremontii*. *L. fremontii* is an annual plant that is endemic to vernal pools wetlands in California. With the characteristics of sharp and stable distribution boundaries across years of varying precipitation patterns and pool hydrology [158], *L. fremontii* has been widely utilized to study the relationship between environmental heterogeneity and plants [156, 157]. With our weighing method, we can investigate the impact of environmental factors (i.e. temperature and precipitation) on the mass of pollen grains of *L. fremontii*. In addition, since pollen grains of *Lasthenia* are normally transported by bees, we can also compare the masses of pollen grains from different species (with the same genus *Lasthenia*), and associate the mass of pollen grains to the distribution patterns between different species.

Fifth, since our cantilever has two cantilevers in close proximity, it is possible that there exists some coupling between the two cantilevers. In our experiments, especially in the context of the weights we have measured, we have not noticed a significant change in the response of one cantilever when we have loaded the other. However, if such a coupling does exist, it could affect the resolution of the system. Such a coupling could result from unintended undercutting of the base of the cantilevers or the viscosity of the medium (in this case air) between the interdigitated fingers of the system. In a future study, the coupling between the adjacent arms could be studied so that its effect on the measurement resolution can be understood.

Finally, for those applications that require the specific drying process we have discussed in the study, it will be desirable to know how much this process affects the weight of the particle being analyzed. This can be accomplished by performing controlled experiments whereby the amount of a specific chemical used in the process is varied while keeping others constant. Such a study can be extremely useful to a wide range of scientists who use similar methods for drying and fixation.

LIST OF REFERENCES

LIST OF REFERENCES

- [1] G. G. Yaralioglu, A. Atalar, S. R. Manalis, and C. F. Quate, "Analysis and design of an interdigital cantilever as a displacement sensor," *Journal of Applied Physics*, vol. 83, pp. 7405-7415, 1998.
- [2] N. V. Lavrik, M. J. Sepaniak, and P. G. Datskos, "Cantilever transducers as a platform for chemical and biological sensors," *Review of Scientific Instruments*, vol. 75, pp. 2229-2253, 2004.
- [3] Q. Chen, W. Tang, D. Z. Wang, X. J. Wu, N. Li, and F. Liu, "Amplified QCM-D biosensor for protein based on aptamer-functionalized gold nanoparticles," *Biosensors & Bioelectronics*, vol. 26, pp. 575-579, 2010.
- [4] K. Autumn, Y. A. Liang, S. T. Hsieh, W. Zesch, W. P. Chan, T. W. Kenny, R. Fearing, and R. J. Full., "Adhesive force of a single gecko foot-hair," *Nature*, vol. 405, pp. 681-685, 2000.
- [5] F. Beyeler, S. Muntwyler, and B. J. Nelson, "A Six-Axis MEMS Force-Torque Sensor With Micro-Newton and Nano-Newtonmeter Resolution," *Journal of Microelectromechanical Systems*, vol. 18, pp. 433-441, 2009.
- [6] G. Binnig, C. F. Quate, and C. Gerber, "Atomic Force Microscope," *Physical Review Letters*, vol. 56, pp. 930-933, 1986.
- [7] S. Lucyszyn, "Review of radio frequency microelectromechanical systems technology," *IEEE Proceedings-Science Measurement and Technology*, vol. 151, pp. 93-103, 2004.
- [8] J. Tamayo, "Nanomechanical systems - Inside track weighs in with solution," *Nature Nanotechnology*, vol. 2, pp. 342-343, 2007.
- [9] R. Raiteri, M. Grattarola, H. J. Butt, and P. Skladal, "Micromechanical cantilever-based biosensors," *Sensors and Actuators B-Chemical*, vol. 79, pp. 115-126, 2001.
- [10] R. Bashir, "BioMEMS: state-of-the-art in detection, opportunities and prospects," *Advanced Drug Delivery Reviews*, vol. 56, pp. 1565-1586, 2004.
- [11] M. Li, H. X. Tang, and M. L. Roukes, "Ultra-sensitive NEMS-based cantilevers for sensing, scanned probe and very high-frequency applications," *Nature Nanotechnology*, vol. 2, pp. 114-120, 2007.

- [12] Y. T. Yang, C. Callegari, X. L. Feng, K. L. Ekinci, and M. L. Roukes, "Zeptogram-scale nanomechanical mass sensing," *Nano Letters*, vol. 6, pp. 583-586, 2006.
- [13] K. Park, J. Jang, D. Irimia, J. Sturgis, J. Lee, J. P. Robinson, M. Toner, and R. Bashir, "Living cantilever arrays' for characterization of mass of single live cells in fluids," *Lab on a Chip*, vol. 8, pp. 1034-1041, 2008.
- [14] S. Xu and R. Mutharasan, "Rapid and Sensitive Detection of Giardia lamblia Using a Piezoelectric Cantilever Biosensor in Finished and Source Waters," *Environmental Science & Technology*, vol. 44, pp. 1736-1741, 2010.
- [15] K. Kim, X. Y. Liu, Y. Zhang, J. Cheng, X. Yu Wu, and Y. Sun, "Elastic and viscoelastic characterization of microcapsules for drug delivery using a force-feedback MEMS microgripper," *Biomedical Microdevices*, vol. 11, pp. 421-427, 2009.
- [16] N. Chronis and L. P. Lee, "Electrothermally activated SU-8 microgripper for single cell manipulation in solution," *Journal of Microelectromechanical Systems*, vol. 14, pp. 857-863, 2005.
- [17] J. K. Luo, A. J. Flewitt, S. M. Spearing, N. A. Fleck, and W. I. Milne, "Comparison of microtweezers based on three lateral thermal actuator configurations," *Journal of Micromechanics and Microengineering*, vol. 15, pp. 1294-1302, 2005.
- [18] P. Lerch, C. K. Slimane, B. Romanowicz, and P. Renaud, "Modelization and characterization of asymmetrical thermal micro-actuators," *Journal of Micromechanics and Microengineering*, vol. 6, pp. 134-137, 1996.
- [19] M. Kohl, E. Just, W. Pfleging, and S. Miyazaki, "SMA microgripper with integrated antagonism," *Sensors and Actuators A-Physical*, vol. 83, pp. 208-213, 2000.
- [20] P. B. O. Millet, S. Regnier, P. Bidaud, D. Collard, L. Buchaillot, "Micro gripper driven by SDAs coupled to an amplification mechanism," *The 1'2th International Conference on Solid State Sensen, Actuators and Microsystems, Boston, MA*, 2003.
- [21] D. Z. J. Schlick, "Design and application of a gripper for microparts using flexure hinges and pneumatic actuation," *Proeding of SPIE, Microrobotics Microassembly III, Boston, MA*, 2001.
- [22] S. K. Jericho, M. H. Jericho, T. Hubbard, and M. Kujath, "Micro-electro-mechanical systems microtweezers for the manipulation of bacteria and small particles," *Review of Scientific Instruments*, vol. 75, pp. 1280-1282, 2004.
- [23] S. K. Nah and Z. W. Zhong, "A microgripper using piezoelectric actuation for micro-object manipulation," *Sensors and Actuators A-Physical*, vol. 133, pp. 218-224, 2007.
- [24] S. Maruo, K. Ikuta, and H. Korogi, "Submicron manipulation tools driven by light in a liquid," *Applied Physics Letters*, vol. 82, pp. 133-135, 2003.

- [25] S. Maruo, K. Ikuta, and H. Korogi, "Force-controllable, optically driven micromachines fabricated by single-step two-photon micro stereolithography," *Journal of Microelectromechanical Systems*, vol. 12, pp. 533-539, 2003.
- [26] Y. Choi, J. Ross, B. Wester, and M. G. Allen, "Mechanically driven microtweezers with integrated microelectrodes," *Journal of Micromechanics and Microengineering*, vol. 18, 2008.
- [27] B. A. Wester, S. Rajaraman, J. D. Ross, M. C. LaPlaca, and M. G. Allen, "Development and characterization of a packaged mechanically actuated microtweezer system," *Sensors and Actuators A-Physical*, vol. 167, pp. 502-511, 2011.
- [28] E. Gil-Santos, D. Ramos, A. Jana, M. Calleja, A. Raman, and J. Tamayo, "Mass Sensing based on deterministic and stochastic responses of elastically coupled nanocantilevers," *Nano Letters*, vol. 9, pp. 4122-4127, 2009.
- [29] S. Dohn, R. Sandberg, W. Svendsen, and A. Boisen, "Enhanced functionality of cantilever based mass sensors using higher modes," *Applied Physics Letters*, vol. 86, 2005.
- [30] E. Forsen, G. Abadal, S. Ghatnekar-Nilsson, J. Teva, J. Verd, R. Sandberg, W. Svendsen, F. Perez-Murano, J. Esteve, E. Figueras, F. Campabadal, L. Montelius, N. Barniol, and A. Boisen, "Ultrasensitive mass sensor fully integrated with complementary metal-oxide-semiconductor circuitry," *Applied Physics Letters*, vol. 87, 2005.
- [31] D. Z. Jin, X. X. Li, J. Liu, G. M. Zuo, Y. L. Wang, M. Liu, and H. Yu, "High-mode resonant piezoresistive cantilever sensors for tens-femtogram resolvable mass sensing in air," *Journal of Micromechanics and Microengineering*, vol. 16, pp. 1017-1023, 2006.
- [32] L. B. Sharos, A. Raman, S. Crittenden, and R. Reifenger, "Enhanced mass sensing using torsional and lateral resonances in microcantilevers," *Applied Physics Letters*, vol. 84, pp. 4638-4640, 2004.
- [33] A. Boisen, J. Thaysen, H. Jensenius, and O. Hansen, "Environmental sensors based on micromachined cantilevers with integrated read-out," *Ultramicroscopy*, vol. 82, pp. 11-16, 2000.
- [34] S. Chatzandroulis, A. Tserepi, D. Goustouridis, P. Normand, and D. Tsoukalas, "Fabrication of single crystal Si cantilevers using a dry release process and application in a capacitive-type humidity sensor," *Microelectronic Engineering*, vol. 61-62, pp. 955-961, 2002.
- [35] L. T. Chen, C. Y. Lee, and W. H. Cheng, "MEMS-based humidity sensor with integrated temperature compensation mechanism," *Sensors and Actuators A-Physical*, vol. 147, pp. 522-528, 2008.
- [36] H. F. Ji, K. M. Hansen, Z. Hu, and T. Thundat, "Detection of pH variation using modified microcantilever sensors," *Sensors and Actuators B-Chemical*, vol. 72, pp. 233-238, 2001.

- [37] R. Bashir, J. Z. Hilt, O. Elibol, A. Gupta, and N. A. Peppas, "Micromechanical cantilever as an ultrasensitive pH microsensor," *Applied Physics Letters*, vol. 81, pp. 3091-3093, 2002.
- [38] P. I. Oden, G. Y. Chen, R. A. Steele, R. J. Warmack, and T. Thundat, "Viscous drag measurements utilizing microfabricated cantilevers," *Applied Physics Letters*, vol. 68, pp. 3814-3816, 1996.
- [39] E. Gil-Santos, D. Ramos, J. Martinez, M. Fernandez-Regulez, R. Garcia, A. San Paulo, M. Calleja, and J. Tamayo, "Nanomechanical mass sensing and stiffness spectrometry based on two-dimensional vibrations of resonant nanowires," *Nature Nanotechnology*, vol. 5, pp. 641-645, 2010.
- [40] X. Y. Dong, Y. Q. Liu, Z. G. Liu, and X. Y. Dong, "Simultaneous displacement and temperature measurement with cantilever-based fiber Bragg grating sensor," *Optics Communications*, vol. 192, pp. 213-217, 2001.
- [41] C. Y. Lee and G. B. Lee, "Micromachine-based humidity sensors with integrated temperature sensors for signal drift compensation," *Journal of Micromechanics and Microengineering*, vol. 13, pp. 620-627, 2003.
- [42] C. A. Savran, T. P. Burg, J. Fritz, and S. R. Manalis, "Microfabricated mechanical biosensor with inherently differential readout," *Applied Physics Letters*, vol. 83, pp. 1659-1661, 2003.
- [43] S. S. Rao, *Mechanical Vibrations*, 5th ed. NJ: Prentice Hall, 2011.
- [44] H. J. Butt and M. Jaschke, "Calculation of thermal noise in atomic-force microscopy," *Nanotechnology*, vol. 6, pp. 1-7, 1995.
- [45] D. S. Golovko, T. Haschke, W. Wiechert, and E. Bonaccorso, "Nondestructive and noncontact method for determining the spring constant of rectangular cantilevers," *Review of Scientific Instruments*, vol. 78, 2007.
- [46] L. Johnson, A. T. K. Gupta, A. Ghafoor, D. Akin, and R. Bashir, "Characterization of vaccinia virus particles using microscale silicon cantilever resonators and atomic force microscopy," *Sensors and Actuators B-Chemical*, vol. 115, pp. 189-197, 2006.
- [47] K. L. Ekinci, Y. T. Yang, and M. L. Roukes, "Ultimate limits to inertial mass sensing based upon nanoelectromechanical systems," *Journal of Applied Physics*, vol. 95, pp. 2682-2689, 2004.
- [48] J. L. Hutter and J. Bechhoefer, "Calibration of atomic-force microscope tips," *Review of Scientific Instruments*, vol. 64, pp. 1868-1873, 1993.
- [49] M. Tortorese, R. C. Barrett, and C. F. Quate, "Atomic resolution with an atomic force microscope using piezoresistive detection," *Applied Physics Letters*, vol. 62, pp. 834-836, 1993.

- [50] J. Thaysen, A. Boisen, O. Hansen, and S. Bouwstra, "Atomic force microscopy probe with piezoresistive read-out and a highly symmetrical Wheatstone bridge arrangement," *Sensors and Actuators a-Physical*, vol. 83, pp. 47-53, 2000.
- [51] R. Berger, H. P. Lang, C. Gerber, J. K. Gimzewski, J. H. Fabian, L. Scandella, E. Meyer, and H. J. Güntherodt, "Micromechanical thermogravimetry," *Chemical Physics Letters*, vol. 294, pp. 363-369, 1998.
- [52] S. Alexander, L. Hellemans, O. Marti, J. Schneir, V. Elings, P. K. Hansma, M. Longmire, and J. Gurley, "An atomic-resolution atomic-force microscope implemented using an optical-lever," *Journal of Applied Physics*, vol. 65, pp. 164-167, 1989.
- [53] N. P. Dcosta and J. H. Hoh, "Calibration of optical-lever sensitivity for atomic-force microscopy," *Review of Scientific Instruments*, vol. 66, pp. 5096-5097, 1995.
- [54] S. R. Manalis, S. C. Minne, A. Atalar, and C. F. Quate, "Interdigital cantilevers for atomic force microscopy," *Applied Physics Letters*, vol. 69, pp. 3944-3946, 1996.
- [55] E. B. Cooper, E. R. Post, S. Griffith, J. Levitan, S. R. Manalis, M. A. Schmidt, C. F. Quate, "High-resolution micromachined interferometric accelerometer," *Applied Physics Letters*, vol. 76, pp. 3316-3318, 2000.
- [56] D. R. Evans and V. S. J. Craig, "Sensing cantilever beam bending by the optical lever technique and its application to surface stress," *Journal of Physical Chemistry B*, vol. 110, pp. 5450-5461, 2006.
- [57] C. A. Savran, A. W. Sparks, J. Sihler, J. Li, W. C. Wu, D. E. Berlin, T. P. Burg, J. Fritz, M. A. Schmidt, and S. R. Manalis "Fabrication and characterization of a micromechanical sensor for differential detection of nanoscale motions," *Journal of Microelectromechanical Systems*, vol. 11, pp. 703-708, 2002.
- [58] Z. N. Demidenko and M. V. Blagosklonny, "Quantifying pharmacologic suppression of cellular senescence: prevention of cellular hypertrophy versus preservation of proliferative potential," *Aging (Albany NY)*, vol. 1, pp. 1008-1016, 2009.
- [59] K. Park, L. J. Millet, N. Kim, H. A. Li, X. Z. Jin, G. Popescu, N. R. Aluru, K. J. Hsia, and R. Bashir "Measurement of adherent cell mass and growth," *Proceedings of the National Academy of Sciences of the United States of America*, vol. 107, pp. 20691-20696, 2010.
- [60] L. Weiss, "The effects of trypsin on the size, viability and dry mass of Sarcoma 37 Cells," *Experimental Cell Research*, vol. 14, pp. 80-83, 1958.
- [61] B. G. Durie and S. E. Salmon, "A clinical staging system for multiple myeloma. Correlation of measured myeloma cell mass with presenting clinical features, response to treatment, and survival," *Cancer*, vol. 36, pp. 842-54, 1975.
- [62] T. P. Burg and S. R. Manalis, "Suspended microchannel resonators for biomolecular detection," *Applied Physics Letters*, vol. 83, pp. 2698-2700, 2003.

- [63] T. P. Burg, M. Godin, S. M. Knudsen, W. Shen, G. Carlson, J. S. Foster, Ken Babcock, and S. R. Manalis, "Weighing of biomolecules, single cells and single nanoparticles in fluid," *Nature*, vol. 446, pp. 1066-1069, 2007.
- [64] T. P. Burg, A. R. Mirza, N. Milovic, C. H. Tsau, G. A. Popescu, J. S. Foster, J. S. Foster, and S. R. Manalis, "Vacuum-packaged suspended microchannel resonant mass sensor for biomolecular detection," *Journal of Microelectromechanical Systems*, vol. 15, pp. 1466-1476, 2006.
- [65] A. K. Bryan, V. C. Hecht, W. Shen, K. Payer, W. H. Grover, and S. R. Manalis, "Measuring single cell mass, volume, and density with dual suspended microchannel resonators," *Lab on a Chip*, vol. 14, pp. 569-76, 2014.
- [66] M. Godin, F. F. Delgado, S. M. Son, W. H. Grover, A. K. Bryan, A. Tzur, P. Jorgensen, K. Payer, A. D Grossman, M. W. Kirschner, and S. R. Manalis, "Using buoyant mass to measure the growth of single cells," *Nature Methods*, vol. 7, pp. 387-390, 2010.
- [67] A. K. Bryan, A. Goranov, A. Amon, and S. R. Manalis, "Measurement of mass, density, and volume during the cell cycle of yeast," *Proceedings of the National Academy of Sciences of the United States of America*, vol. 107, pp. 999-1004, 2010.
- [68] F. Feijo Delgado, N. Cermak, V. C. Hecht, S. Son, Y. Li, S. M. Knudsen, S. Olcum, J. M. Higgins, J. Chen, W. H. Grover, S. R. Manalis, "Intracellular water exchange for measuring the dry mass, water mass and changes in chemical composition of living cells," *PLoS One*, vol. 8, pp. e67590, 2013.
- [69] W. H. Grover, A. K. Bryan, M. Diez-Silva, S. Suresh, J. M. Higgins, and S. R. Manalis, "Measuring single-cell density," *Proceedings of the National Academy of Sciences of the United States of America*, vol. 108, pp. 10992-6, 2011.
- [70] E. A. Corbin, L. J. Millet, K. R. Keller, W. P. King, and R. Bashir, "Measuring physical properties of neuronal and glial cells with resonant microsensors," *Analytical chemistry*, vol. 86, pp. 4864-4872, 2014.
- [71] G. Popescu, K. Park, M. Mir, and R. Bashir, "New technologies for measuring single cell mass," *Lab on a Chip*, vol. 14, pp. 646-652, 2014.
- [72] A. Boisen, S. Dohn, S. S. Keller, S. Schmid, and M. Tenje, "Cantilever-like micromechanical sensors," *Reports on Progress in Physics*, vol. 74, 2011.
- [73] B. Ilic, D. Czaplewski, M. Zalalutdinov, H. G. Craighead, P. Neuzil, C. Campagnolo, and C. Batt, "Single cell detection with micromechanical oscillators," *Journal of Vacuum Science & Technology B*, vol. 19, pp. 2825-2828, 2001.
- [74] A. Gupta, D. Akin, and R. Bashir, "Single virus particle mass detection using microresonators with nanoscale thickness," *Applied Physics Letters*, vol. 84, pp. 1976-1978, 2004.

- [75] J. A. Walker, K. J. Gabriel, and M. Mehregany, "Mechanical integrity of polysilicon films exposed to hydrofluoric-acid solutions," *Journal of Electronic Materials*, vol. 20, pp. 665-670, 1991.
- [76] Objet Ltd. [Online]. Available: <http://www.objet.com/3D-Printing-Materials/>
- [77] F. Mateen, "Mechanical gripper for manipulation of single micro-particles," Master of Science, Purdue University, 2008.
- [78] R. U. Lukacs, A. S. Goldstein, D. A. Lawson, D. H. Cheng, and O. N. Witte, "Isolation, cultivation and characterization of adult murine prostate stem cells," *Nature Protocols*, vol. 5, pp. 702-713, 2010.
- [79] J. Z. Hilt, A. K. Gupta, R. Bashir, and N. A. Peppas, "Ultrasensitive BioMEMS sensors based on microcantilevers patterned with environmentally responsive hydrogels," *Biomedical Microdevices*, vol. 5, pp. 177-184, 2003.
- [80] K. M. Hansen, H. F. Ji, G. H. Wu, R. Datar, R. Cote, A. Majumdar, and T. Thundat, "Cantilever-based optical deflection assay for discrimination of DNA single-nucleotide mismatches," *Analytical Chemistry*, vol. 73, pp. 1567-1571, 2001.
- [81] R. Flores-Perez, A. K. Gupta, R. Bashir, and A. Ivanisevic, "Cantilever-based sensor for the detection of different chromophore isomers," *Analytical Chemistry*, vol. 79, pp. 4702-4708, 2007.
- [82] F. M. Battiston, J. P. Ramseyer, H. P. Lang, M. K. Baller, C. Gerber, J. K. Gimzewski, E. Meyer, and H. J. Guentherodt, "A chemical sensor based on a microfabricated cantilever array with simultaneous resonance-frequency and bending readout," *Sensors and Actuators B-Chemical*, vol. 77, pp. 122-131, 2001.
- [83] B. Ilic, D. Czaplewski, H. G. Craighead, P. Neuzil, C. Campagnolo, and C. Batt, "Mechanical resonant immunospecific biological detector," *Applied Physics Letters*, vol. 77, pp. 450-452, 2000.
- [84] A. N. Cleland and M. L. Roukes, "Noise processes in nanomechanical resonators," *Journal of Applied Physics*, vol. 92, pp. 2758-2769, 2002.
- [85] K. M. Vanvliet, "Derivation of the fluctuation-dissipation theorem," *Physical Review*, vol. 109, pp. 1021-1022, 1958.
- [86] J. Weber, "Remarks on the fluctuation dissipation theorem," *Physical Review*, vol. 98, pp. 1165-1165, 1955.
- [87] K. Icoz, "Immunomagnetic bead-assisted nanomechanical biosensor," Doctor of Philosophy, Purdue University, 2010.
- [88] B. D. Chan, K. Icoz, R. L. Gieseck, and C. A. Savran, "Selective Weighing of individual microparticles using a hybrid micromanipulator-nanomechanical resonator system," *IEEE Sensors Journal*, vol. 13, pp. 2857-2862, 2013.
- [89] K. Park, N. Kim, D. T. Morissette, N. R. Aluru, and R. Bashir, "Resonant MEMS mass sensors for measurement of microdroplet evaporation," *Journal of Microelectromechanical Systems*, vol. 21, pp. 702-711, 2012.

- [90] J. F. Shackelford and W. Alexander, *CRC materials science and engineering handbook*, 3rd ed. Boca Raton, FL: CRC Press, 2001.
- [91] S. D. Senturia, *Microsystem design*. Boston: Kluwer Academic Publishers, 2001.
- [92] J. E. Sader, J. W. M. Chon, and P. Mulvaney, "Calibration of rectangular atomic force microscope cantilevers," *Review of Scientific Instruments*, vol. 70, pp. 3967-3969, 1999.
- [93] J. E. Sader, I. Larson, P. Mulvaney, and L. R. White, "Method for the calibration of atomic-force microscope cantilevers," *Review of Scientific Instruments*, vol. 66, pp. 3789-3798, 1995.
- [94] N. Lobontiu, I. Lupea, R. Ilic, and H. G. Craighead, "Modeling, design, and characterization of multisegment cantilevers for resonant mass detection," *Journal of Applied Physics*, vol. 103, p. 064306, 2008.
- [95] N. Lobontiu, *Dynamics of microelectromechanical systems*. New York: Springer, 2007.
- [96] Y. Liu, G. Zhao, L. Wen, X. Z. Xu, and J. R. Chu, "Mass-loading effect on quality factor of floppy silicon microcantilever in free air space," *Micro & Nano Letters*, vol. 6, pp. 62-65, 2011.
- [97] J. M. Mitchison, "Single cell studies of the cell cycle and some models," *Theoretical Biology and Medical Modelling*, vol. 2, pp. 4, 2005.
- [98] J. M. Mitchison, "The growth of single cells: I. *Schizosaccharomyces Pombe*," *Experimental Cell Research*, vol. 13, pp. 244-262, 1957.
- [99] G. Popescu, Y. Park, N. Lue, C. Best-Popescu, L. Deflores, R. R. Dasari, M. S. Feld, K. Badizadegan, "Optical imaging of cell mass and growth dynamics," *American Journal of Physiology-Cell Physiology*, vol. 295, pp. C538-C544, 2008.
- [100] M. Mir, Z. Wang, Z. Shen, M. Bednarz, R. Bashir, I. Golding, S. G. Prasanth, and G. Popescu, "Optical measurement of cycle-dependent cell growth," *Proceedings of the National Academy of Sciences of the United States of America*, vol. 108, pp. 13124-13129, 2011.
- [101] L. M. Sosnoskie, T. M. Webster, D. Dales, G. C. Rains, T. L. Grey, and A. S. Culpepper, "Pollen grain size, density, and settling velocity for palmer Amaranth (*Amaranthus palmeri*)," *Weed Science*, vol. 57, pp. 404-409, 2009.
- [102] D. E. Aylor, "Settling speed of corn (*Zea mays*) pollen," *Journal of Aerosol Science*, vol. 33, pp. 1601-1607, 2002.
- [103] R. van Hout and J. Katz, "A method for measuring the density of irregularly shaped biological aerosols such as pollen," *Journal of Aerosol Science*, vol. 35, pp. 1369-1384, 2004.
- [104] E. A. Dawes and D. W. Ribbons, "The endogenous metabolism of microorganisms," *Annu Rev Microbiol*, vol. 16, pp. 241-64, 1962.

- [105] A. M. Makarieva, V. G. Gorshkov, B. L. Li, S. L. Chown, P. B. Reich, and V. M. Gavrilov, "Mean mass-specific metabolic rates are strikingly similar across life's major domains: Evidence for life's metabolic optimum," *Proceedings of the National Academy of Sciences of the United States of America*, vol. 105, pp. 16994-9, 2008.
- [106] A. Jakubowska and R. Korona, "Epistasis for growth rate and total metabolic flux in yeast," *PLoS One*, vol. 7, pp. e33132, 2012.
- [107] G. Bratbak, "Bacterial Biovolume and Biomass Estimations," *Applied and Environmental Microbiology*, vol. 49, pp. 1488-1493, 1985.
- [108] M. Loferer-Krossbacher, J. Klima, and R. Psenner, "Determination of bacterial cell dry mass by transmission electron microscopy and densitometric image analysis," *Applied and Environmental Microbiology*, vol. 64, pp. 688-694, 1998.
- [109] R. Barer, "Interference microscopy and mass determination," *Nature*, vol. 169, pp. 366-7, 1952.
- [110] H. G. Davies and M. H. Wilkins, "Interference microscopy and mass determination," *Nature*, vol. 169, p. 541, 1952.
- [111] R. Barer, "Determination of dry mass, thickness, solid and water concentration in living cells," *Nature*, vol. 172, pp. 1097-8, 1953.
- [112] K. Lee, K. Kim, J. Jung, J. Heo, S. Cho, S. Lee, G. Chang, Y. Jo, H. Park, and Y. Park, "Quantitative phase imaging techniques for the study of cell pathophysiology: from principles to applications," *Sensors*, vol. 13, pp. 4170-4191, 2013.
- [113] E. A. Corbin, B. R. Dorvel, L. J. Millet, W. P. King, and R. Bashir, "Micro-patterning of mammalian cells on suspended MEMS resonant sensors for long-term growth measurements," *Lab on a Chip*, pp. 1401-1404, 2014.
- [114] Y. Weng, F. F. Delgado, S. Son, T. P. Burg, S. C. Wasserman, and S. R. Manalis, "Mass sensors with mechanical traps for weighing single cells in different fluids," *Lab on a Chip*, vol. 11, pp. 4174-80, 2011.
- [115] B. G. Nordestgaard and J. Rostgaard, "Critical-Point Drying Versus Freeze-Drying for Scanning Electron-Microscopy - a quantitative and qualitative study on isolated hepatocytes," *Journal of Microscopy-Oxford*, vol. 137, pp. 189-207, 1985.
- [116] K. Hotary, X. Y. Li, E. Allen, S. L. Stevens, and S. J. Weiss, "A cancer cell metalloprotease triad regulates the basement membrane transmigration program," *Genes & Development*, vol. 21, pp. 1139-1139, 2007.
- [117] F. R. Turner and A. P. Mahowald, "Scanning electron-microscopy of drosophila-melanogaster embryogenesis .3. formation of the head and caudal segments," *Developmental Biology*, vol. 68, pp. 96-109, 1979.

- [118] F. R. Turner and A. P. Mahowald, "Scanning electron-microscopy of drosophila embryogenesis .1. structure of egg envelopes and formation of cellular blastoderm," *Developmental Biology*, vol. 50, pp. 95-108, 1976.
- [119] R. S. Richards, L. X. Wang, and H. Jelinek, "Erythrocyte oxidative damage in chronic fatigue syndrome," *Archives of Medical Research*, vol. 38, pp. 94-98, 2007.
- [120] L. C. S. Medeiros, W. De Souza, C. G. Jiao, H. Barrabin, and K. Miranda, "Visualizing the 3D architecture of multiple erythrocytes infected with plasmodium at nanoscale by focused ion beam-scanning electron microscopy," *PLoS One*, vol. 7, pp. e33445, 2012.
- [121] O. Ohtani, "3-dimensional organization of the connective-tissue fibers of the human-pancreas - a scanning electron-microscopic study of naoh treated-tissues," *Archivum Histologicum Japonicum*, vol. 50, pp. 557-566, 1987.
- [122] M. Y. Fan, Z. P. Lum, X. W. Fu, L. Levesque, I. T. Tai, and A. M. Sun, "Reversal of diabetes in BB rats by transplantation of encapsulated pancreatic-islets," *Diabetes*, vol. 39, pp. 519-522, 1990.
- [123] E. Sunami, H. Kanazawa, H. Hashizume, M. Takeda, K. Hatakeyama, and T. Ushiki, "Morphological characteristics of Schwann cells in the islets of Langerhans of the murine pancreas," *Archives of Histology and Cytology*, vol. 64, pp. 191-201, 2001.
- [124] V. Chandra, G. Swetha, S. Muthyala, A. K. Jaiswal, J. R. Bellare, P. D. Nair, R. R. Bhonde, "Islet-like cell aggregates generated from human adipose tissue derived stem cells ameliorate experimental diabetes in mice," *PLoS One*, vol. 6, pp. e20615, 2011.
- [125] D. Terada, S. Hattori, T. Honda, M. Iitake, and H. Kobayashi, "Embossed-carving processing of cytoskeletons of cultured cells by using focused ion beam technology," *Microscopy Research Technique*, vol. 76, pp. 290-295, 2013.
- [126] C. A. Morgan, N. Herman, P. A. White, and G. Vesey, "Preservation of micro-organisms by drying; a review," *Journal of Microbiological Methods*, vol. 66, pp. 183-93, 2006.
- [127] J. Malm, D. Giannaras, M. O. Riehle, N. Gadegaard, and P. Sjoval, "Fixation and drying protocols for the preparation of cell samples for time-of-flight secondary ion mass spectrometry analysis," *Analytical Chemistry*, vol. 81, pp. 7197-7205, 2009.
- [128] D. Hopwood, "Theoretical and practical aspects of glutaraldehyde fixation," *Histochemical Journal*, vol. 4, pp. 267-303, 1972.
- [129] J. D. Bancroft and M. Gamble, *Theory and practice of histological techniques*, 6th ed. Edinburgh: Churchill Livingstone, 2008.

- [130] K. U. Laiho, Shelburne, Jd, and B. F. Trump, "Observations on cell volume, ultrastructure, mitochondrial conformation and vital-dye uptake in Ehrlich ascites tumor cells - Effects of Inhibiting Energy Production and Function of Plasma Membrane," *American Journal of Pathology*, vol. 65, pp. 203-214, 1971.
- [131] D. F. Bray, J. Bagu, and P. Koegler, "Comparison of hexamethyldisilazane (HMDS), Peldri II, and critical-point drying methods for scanning electron microscopy of biological specimens," *Microscopy Research and Technology*, vol. 26, pp. 489-95, 1993.
- [132] J. C. Araujo, F. C. Teran, R. A. Oliveira, E. A. Nour, M. A. Montenegro, J. R. Campos, R. F. Vazoller, "Comparison of hexamethyldisilazane and critical point drying treatments for SEM analysis of anaerobic biofilms and granular sludge," *Journal of Electron Microscopy*, vol. 52, pp. 429-433, 2003.
- [133] J. T. Lee and K. L. Chow, "SEM sample preparation for cells on 3D scaffolds by freeze-drying and HMDS," *Scanning*, vol. 34, pp. 12-25, 2012.
- [134] F. Braet, R. De Zanger, and E. Wisse, "Drying cells for SEM, AFM and TEM by hexamethyldisilazane: a study on hepatic endothelial cells," *Journal of Microscopy*, vol. 186, pp. 84-87, 1997.
- [135] J. L. Nation, "A new method using hexamethyldisilazane for preparation of soft insect tissues for scanning electron-microscopy," *Stain Technology*, vol. 58, pp. 347-351, 1983.
- [136] N. H. Hazrin-Chong and M. Manefield, "An alternative SEM drying method using hexamethyldisilazane (HMDS) for microbial cell attachment studies on sub-bituminous coal," *Journal of Microbiological Methods*, vol. 90, pp. 96-99, 2012.
- [137] S. W. Jung, H. M. Joo, J. S. Park, and J. H. Lee, "Development of a rapid and effective method for preparing delicate dinoflagellates for scanning electron microscopy," *Journal of Applied Phycology*, vol. 22, pp. 313-317, 2010.
- [138] M. F. Clarke, J. E. Dick, P. B. Dirks, C. J. Eaves, C. H. Jamieson, D. L. Jones, J. Visvader, I. L. Weissman, and G. M. Wahl, "Cancer stem cells--perspectives on current status and future directions: AACR Workshop on cancer stem cells," *Cancer Research*, vol. 66, pp. 9339-9344, 2006.
- [139] N. Barker, R. A. Ridgway, J. H. van Es, M. van de Wetering, H. Begthel, M. van den Born, E. Danenberg, A. R. Clarke, O. J. Sansom, and H. Clevers, "Crypt stem cells as the cells-of-origin of intestinal cancer," *Nature*, vol. 457, pp. 608-611, 2009.
- [140] H. H. Wang, Wang, L., Chan, B. D., Savran, C. A., Jerde, T. J., Ratliff, T. L., "Androgen receptor-dependent prostate stem cells drives prostate epithelial expansion in the absence of androgen in response to autoimmune prostatitis," *in submission*.
- [141] B. J. Boehm, S. A. Colopy, T. J. Jerde, C. J. Loftus, and W. Bushman, "Acute bacterial inflammation of the mouse prostate," *The Prostate*, vol. 72, pp. 307-317, 2012.

- [142] H. Fischer, I. Polikarpov, and A. F. Craievich, "Average protein density is a molecular - weight - dependent function," *Protein Science*, vol. 13, pp. 2825-2828, 2004.
- [143] B. D. Chan, F. Mateen, C. L. Chang, K. Icoz, and C. A. Savran, "A compact manually actuated micromanipulator," *Journal of Microelectromechanical Systems*, vol. 21, pp. 7-9, 2012.
- [144] R. Kafri, J. Levy, M. B. Ginzberg, S. Oh, G. Lahav, and M. W. Kirschner, "Dynamics extracted from fixed cells reveal feedback linking cell growth to cell cycle," *Nature*, vol. 494, pp. 480-3, 2013.
- [145] T. T. Hansel, J. D. Pound, D. Pilling, G. D. Kitas, M. Salmon, T. A. Gentle, S. S. Lee, and R. A. Thompson, "Purification of human-blood eosinophils by negative selection using immunomagnetic beads," *Journal of Immunological Methods*, vol. 122, pp. 97-103, 1989.
- [146] H. Bordelon, P. K. Russ, D. W. Wright, and F. R. Haselton, "A magnetic bead-based method for concentrating DNA from human urine for downstream detection," *PLoS One*, vol. 8, pp. e68369, 2013.
- [147] K. Hoshino, Y. Y. Huang, N. Lane, M. Huebschman, J. W. Uhr, E. P. Frenkel, X. Zhang, "Microchip-based immunomagnetic detection of circulating tumor cells," *Lab on a Chip*, vol. 11, pp. 3449-3457, 2011.
- [148] C. L. Chang, C. A. Savran, S. Jalal, and D. E. Matei, "Micro-aperture Chip system for high-throughput immunomagnetic cell detection," *2012 IEEE Sensors Proceedings*, pp. 1672-1675, 2012.
- [149] K. Icoz and C. Savran, "Nanomechanical biosensing with immunomagnetic separation," *Applied Physics Letters*, vol. 97, pp. 123701, 2010.
- [150] M. Marko, C. Hsieh, W. Moberlychan, C. A. Mannella, and J. Frank, "Focused ion beam milling of vitreous water: prospects for an alternative to cryo-ultramicrotomy of frozen-hydrated biological samples," *Journal of Microscopy-Oxford*, vol. 222, pp. 42-47, 2006.
- [151] R. Gordon, D. Losic, M. A. Tiffany, S. S. Nagy, and F. A. S. Sterrenburg, "The Glass Menagerie: diatoms for novel applications in nanotechnology," *Trends in Biotechnology*, vol. 27, pp. 116-127, 2009.
- [152] K. M. Wee, T. N. Rogers, B. S. Altan, S. A. Hackney, and C. Hamm, "Engineering and medical applications of diatoms," *Journal of Nanoscience and Nanotechnology*, vol. 5, pp. 88-91, 2005.
- [153] K. H. Sandhage, M. B. Dickerson, P. M. Huseman, M. A. Caranna, J. D. Clifton, T. A. Bull, T. J. Heibel, W.R. Overton, and M. E. A. Schoenwaelder, "Novel, bioclastic route to self-assembled, 3D, chemically tailored meso/nanostructures: Shape-preserving reactive conversion of biosilica (diatom) microshells," *Advanced Materials*, vol. 14, pp. 429-433, 2002.
- [154] J. Parkinson and R. Gordon, "Beyond micromachining: the potential of diatoms," *Trends in Biotechnology*, vol. 17, pp. 190-196, 1999.

- [155] A. R. Parker and H. E. Townley, "Biomimetics of photonic nanostructures," *Nature Nanotechnology*, vol. 2, pp. 347-353, 2007.
- [156] N. C. Emery, "Ecological limits and fitness consequences of cross-gradient pollen movement in *Lasthenia fremontii*," *American Naturalist*, vol. 174, pp. 221-235, 2009.
- [157] N. C. Emery, K. J. Rice, and M. L. Stanton, "Fitness variation and local distribution limits in an annual plant population," *Evolution*, vol. 65, pp. 1011-1020, 2011.
- [158] N. C. Emery, M. L. Stanton, and K. J. Rice, "Factors driving distribution limits in an annual plant community," *New Phytologist*, vol. 181, pp. 734-747, 2009.
- [159] S. W. Kim and G. H. Kim, "Thickness-profile measurement of transparent thin-film layers by white-light scanning interferometry," *Applied Optics*, vol. 38, pp. 5968-5973, 1999.
- [160] Y. E. Korchev, J. Gorelik, M. J. Lab, E. V. Sviderskaya, C. L. Johnston, C. R. Coombes, I. Vodyanoy, and C. R. Edwards, "Cell volume measurement using scanning ion conductance microscopy," *Biophysical Journal*, vol. 78, pp. 451-457, 2000.

APPENDICES

Appendix A Assembly of the Micromanipulator

The assembly process of the micromanipulator is schematically presented in Figure A-1. The micromanipulator is comprised of a micrometer head, a tweezers holder, a clamping cap, a cone tip, and a microtweezer. The assembly process starts with inserting the micrometer head into the tweezers holder as shown in Figure A-1b. Afterward, the tip of the micrometer head is capped by the cone tip as shown in Figure A-1c. The microtweezer is then carefully placed on the tweezers holder by using another translation stage (Figure A-1d). The two outside prongs are sled into the two slots on the tweezers holder to prevent the microtweezer from moving during operation. Finally, the clamping cap is utilized to secure the microtweezer from moving in the vertical direction. With appropriate dimensional design of every junction part, we are able to perform a boltless mounting between different parts.

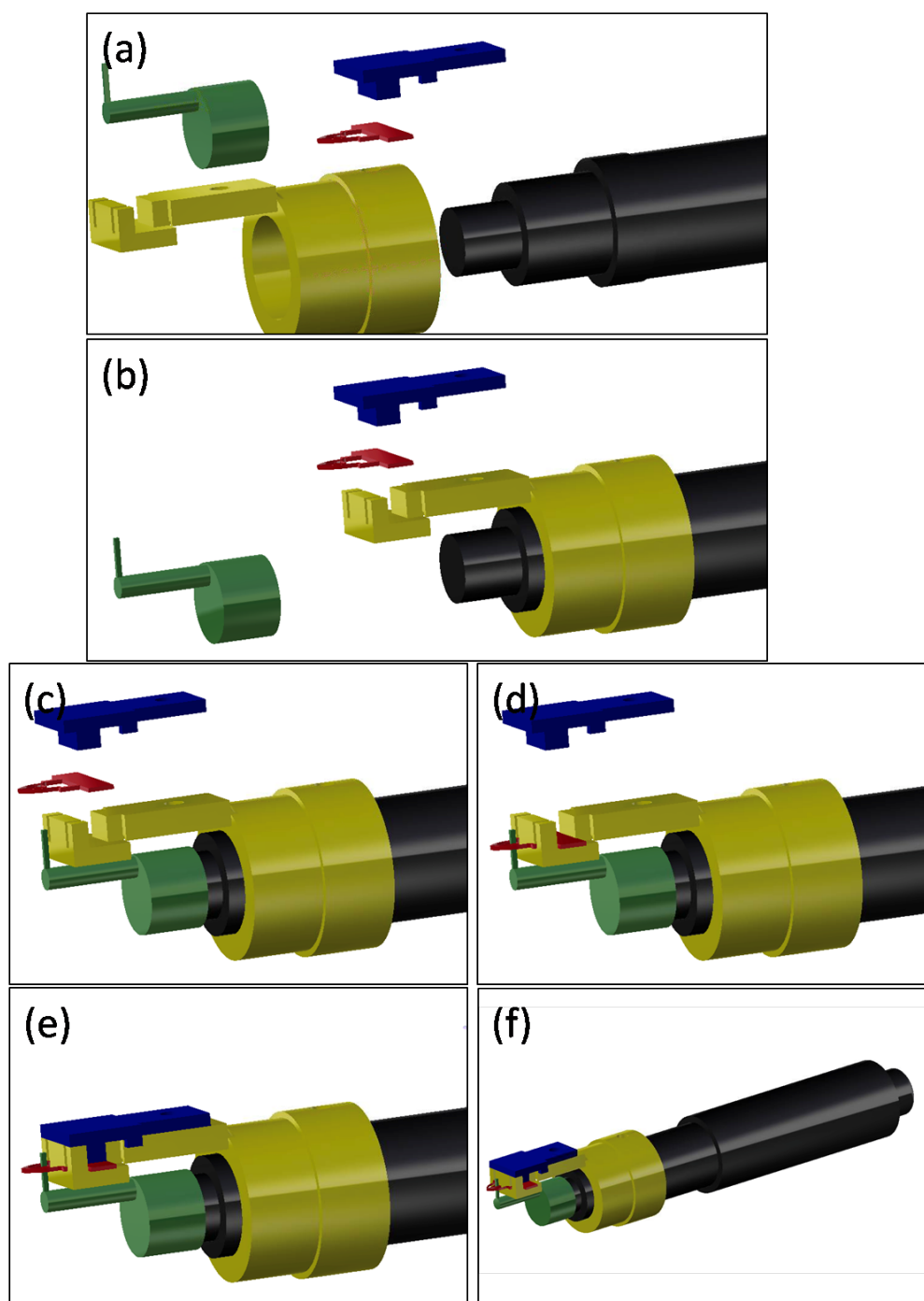


Figure A-1: Schematics of the assembly process. (a) An explosion view of the micromanipulator, (b) assembling micrometer head with the tweezers holder, (c) assembling the cone tip, (d) installing the microtweezer, (e) assembling the clamping cap, (f) a zoom-out view of the micromanipulator.

Appendix B Focused Ion Beam (FIB) Milling of Cells

The experiment of FIB cell milling was carried out by FEI Quanta 3D FEG (FEI Company) that has a dual-beam source, one is the gallium ion beam column and the other is the electron beam column. The milling procedure is presented in Figure B-1. First, a post-weighed target cell was selected under a SEM as seen in Figure B-1a. Afterward, the gallium ion beam was utilized incorporated with the trimethylcyclopentadienyl platinum $((\text{CH}_3)_3\text{Pt}(\text{CpCH}_3))$ gas injector to selectively deposit a thin layer of platinum on the sample cell as shown in Figure B-1b and Figure B-1f. The platinum layer serves two purposes: 1) to define the milling edge, and to prevent the cell surface around the milling edge from being damaged by ion beam, and 2) to improve the uniformity of the milling speed throughout the milling path and therefore eliminate most artifacts on the milled surface (strips in Figure B-1c). After the Pt deposition process, the gas injector was turned off and the cell starts to be milled by the gallium FIB as seen in Figure B-1g and Table B-1. The milled cell is presented in Figure B-1c and B1d. With this FIB milling process, the targeted cell can be sectioned easily and precisely with minimized structural distortion that would most likely happen in traditional cell sectioning techniques.

Table B-1: FIB cell milling process

Step	Description	Acc. Current
#1	“Regular cross-section” until half of the cell has been removed	4.6 nA
#2	“Cleaning cross-section” to slowly approach the cutting edge	1.9 nA
#3	“Cleaning cross-section” to clean the cutting edge	0.64 nA
Milling with the ion beam was done at accelerating voltage of 20 kV		

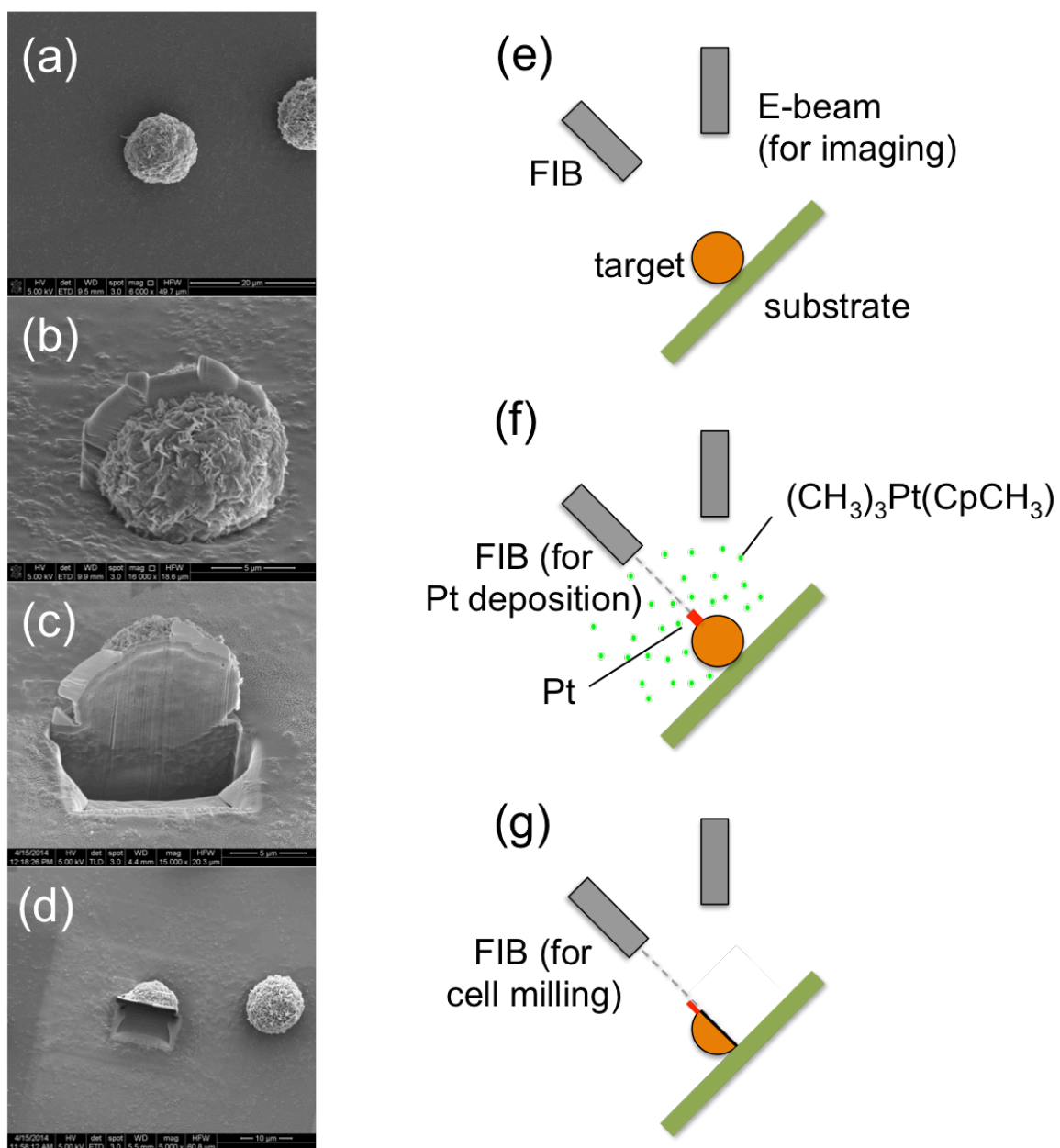


Figure B-1: SEM images of (a) the selected KB cell, (b) KB cell coated with a thin Pt layer, (c) and (d) milled KB cell. (e-g) Flow chart of the FIB cell milling process.

VITA

VITA

Bin-Da Chan
School of Mechanical Engineering, Purdue University
Birck Nanotechnology Center, Purdue University

Bin-Da Chan received the B.S. degree in Mechanical Engineering from National Chiao Tung University, Hsinchu City, Taiwan in 2006, and the M.S. degree in Mechanical Engineering, Fabrication Division from National Taiwan University, Taipei City, Taiwan in 2008. He is currently working toward the Ph.D. degree in the School of Mechanical Engineering at Purdue University, where his research involves, MEMS, microfabrication, biosensors, and nanomechanical sensors.